RSC Advances

RSC Publishing

REVIEW

View Article Online
View Journal | View Issue

Cite this: *RSC Adv.*, 2013, **3**, 22790

An overview of the engineered graphene nanostructures and nanocomposites

Jiahua Zhu,[ab] Minjiao Chen,[a] Qingliang He,[a] Lu Shao,[c] Suying Wei*[b] and Zhanhu Guo*[a]

This critical review focuses on the property analysis of graphene and graphene nanocomposites (GNCs) and their demonstrated superior performances in energy storage and conversion, electrochemical- and biosensing, environmental remediation and flame retardant application and atomic thickness membrane separation. The performances of graphene and GNCs are strongly dependent on their chemical component, synthetic method, nanoscale morphology, and assembling structure of the hybrids. The current progress in supercapacitor energy storage density, solar cell power conversion efficiency, thermoelectric energy conversion efficiency, electrochemical sensing capability, biosensor sensitivity, heavy metal adsorption capacity and efficiency, photocatalytic degradation rate of organic dye, flame retardant polymer nanocomposites, graphene and porous graphene membranes is discussed with detailed examples through extensive analysis of the literature.

Received 4th July 2013
Accepted 2nd September 2013

DOI: 10.1039/c3ra44621b

www.rsc.org/advances

1. Introduction

The two dimensional (2D) single carbon atomic thick graphene arranged as a honeycomb lattice has unique electron and phonon transport behavior, high thermal conductivity (5000 W m^{-1} K^{-1}), electrical conductivity (6000 S cm^{-1}) and mechanical stiffness (130 GPa), optical transmittance of ~98% and large specific surface area (2675 m^2 g^{-1}).[1–7] During the last few decades, significant efforts have been made toward the use

[a]*Integrated Composites Laboratory (ICL), Dan F Smith Department of Chemical Engineering, Lamar University, Beaumont, TX 77710, USA. E-mail: zhanhu.guo@lamar.edu; Tel: +1 409 880 7654*

[b]*Department of Chemistry and Biochemistry, Lamar University, Beaumont, TX 77710, USA*

[c]*School of Chemical Engineering and Technology, State Key Laboratory of Urban Water Resource and Environment (SKLUWRE), Harbin Institute of Technology, Harbin 150001, P.R. China*

Dr Jiahua Zhu received his MS in Chemical Engineering from Nanjing University of Technology in 2009, where he researched self-lubricating sealing composite materials with Prof. Xiaohua Lu and Prof. Xin Feng. He received a PhD degree of Chemical Engineering at Lamar University. Dr Zhu has been doing research in Integrated Composites Laboratory (ICL) supervised by Prof. Zhanhu Guo. His research interests involve new synthetic routes to multifunctional nanocomposites with advanced applications in environmental remediation, energy harvesting, and electronic device fabrication. He was awarded the Chinese Government Award for Outstanding Self-Financed Students Abroad and SPE Thermoplastic Elastomers Special Interest Group Scholarship in 2012.

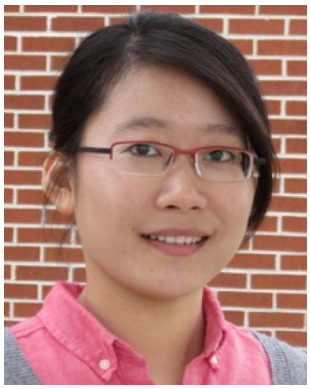

Dr Minjiao Chen is currently a research associate in Integrated Composites Laboratory (ICL) at Lamar University. She received PhD degree in Chemistry from the Hong Kong University of Science and Technology (2012) and BS degree in Applied Chemistry from Yangzhou University (2006). Her research interests are in biochemistry including bioorganic chemistry, protein chemistry, enzymology and advanced bio-applications of multifunctional nanocomposites.

of carbon nanotubes as electronic devices, sensors, and reinforcements of polymer matrices, there are still remaining challenges such as the nanotube agglomeration, limited availability of high-quality nanotubes, and high production cost. Therefore, graphene provides an alternative option to produce advanced materials due to their excellent physicochemical properties and the natural abundance of their precursor, graphite.

Different methods have been developed to obtain high quality graphene, including physical methods such as mechanical exfoliation,[8] and chemical methods including chemical reduction of graphite oxide,[9,10] total organic synthesis[11] and chemical vapor deposition (CVD).[12] Among these methods, chemical reduction from graphite oxide (GO) is the most promising and economical method for scale-up production of graphene. The intermediate, GO, obtains an expanded *d*-spacing between individual sheets and can be easily exfoliated into single sheets with sonication. In addition, the large number of oxygen-containing groups at the edge and basal planes of graphene provide sufficient functional sites, which could serve as templates for the growth of different nanostructures.

Most of the current research in this area is focused on the synthesis, characterization, device manufacturing and

Mr Qingliang He, currently a PhD candidate in the Integrated Composites Laboratory, Dan F. Smith Department of Chemical Engineering at Lamar University. Mr He obtained a BS degree in Chemistry from Anhui University in 2005, and a MS degree in Safety Technology and Engineering from State Key Laboratory of Fire Science, University of Science and Technology of China in 2009. Mr He also had a three-year working experience as a Visiting Scholar at University of Georgia (2008 to 2010). Mr He is currently the student member of American Institute of Chemical Engineers (AIChE) and Materials Research Society (MRS). His current research focuses on fundamental science behind multifunctional light-weight polyolefin-based magnetic nanocomposites for microwave absorption and environmental remediation applications.

Dr Suying Wei, currently an Assistant Professor in the Department of Chemistry and Biochemistry at Lamar University, obtained a chemistry PhD degree from Louisiana State University (2006), a MS in applied chemistry from Beijing University of Chemical Technology (2000) and BS in chemical engineering from Shandong University of Science and Technology (1996). Her research interests are in multifunctional composites especially those towards biomedical applications. Her expertise is in analytical, materials and surface chemistry. She was awarded NSF summer institute fellowship, Pfizer graduate fellowship and Robinson award for excellent research in analytical science during previous professional development.

Dr Lu Shao, is currently a full professor in School of Chemical Engineering and Technology at Harbin Institute of Technology (HIT) in China. He received his BSc (1999) and MSc (2001) from HIT, and his PhD (2005) from National University of Singapore (mentored by Prof. Tai-Shung Chung, Prof. Suat-Hong Goh and Dr Phallathadka Pramoda Kumari). Before joining HIT in 2006, he had worked as the assistant project manager in C-PAK Company, Singapore for more than one year. His research interests are advanced membrane materials and functional composite materials, with a particular focus on energy and environmental issues. He was awarded the Chinese Government Award for Outstanding Self-Financed Students Abroad in 2008 and New Century Excellent Talents in University in 2011.

Dr Zhanhu Guo, currently an Assistant Professor in Dan F. Smith Department of Chemical Engineering at Lamar University, obtained a Chemical Engineering PhD degree from Louisiana State University (2005) and received three-year (2005–2008) postdoctoral training in Mechanical and Aerospace Engineering Department in University of California Los Angeles. Dr Guo directs the Integrated Composites Laboratory and Chairs the Composite Division of American Institute of Chemical Engineers (AIChE, 2010–2011). His current research focuses on fundamental science behind multifunctional light-weight nanocomposites for energy harvesting, environmental remediation and electromagnetic radiation shielding applications.

applications of graphene, GO as well as their corresponding nanocomposites. To achieve different functionalities, various nanomaterials have been incorporated to graphene or GO including nanostructural carbons, noble metals, metal oxides, conductive polymers and *etc.* Besides, graphene has been used as fillers in polymer matrix to enhance the mechanical strength, conductivity and gas barrier performance.[13–16] Targeting to different applications, either surface modification of graphene by grafting functional groups or composite design by decorating functional nanostructures could be a feasible approach. For examples, (a) graphene-based materials in environmental remediation: Fe@Fe_2O_3/Si–O–S nanoparticles (NPs) coated on graphene exhibited much faster and complete adsorption removal of Cr(VI) within a wide range of pH conditions.[17] The Fe_3O_4/graphene nanocomposites were used to remove arsenic(III) and arsenic(V) ions from waste water with an extremely high removal efficiency of 99.9%, which can be easily separated by an external magnetic field after adsorption.[18,19] Highly selective adsorption of Hg^{2+} (adsorption capacity: 980 mg g^{-1}) was observed by a polypyrrole-reduced graphene oxide (PPy/RGO) composite.[20] The TiO_2 NPs have been grown on graphene to enhance the photocatalytic activity in the degradation of rhodamine B;[21] (b) graphene-based materials in supercapacitors: to improve the energy density of supercapacitor electrodes, pseudoactive materials majorly including metal oxides (RuO_2, MnO_2, Co_3O_4, NiO, V_2O_5, $NiCo_2O_4$, and *etc.*)[22–32] and conductive polymers (polyaniline (PANI), PPy, poly(3,4-ethylenedioxythiophene) (PEDOT) and *etc.*)[33–39] have been incorporated in graphene and their electrochemical properties have been widely investigated; (c) graphene-based materials in sensors: giant magnetoresistive (GMR) sensors, electrochemical sensors, and biosensors have been developed using graphene, modified graphene and graphene nanocomposites.

This critical review is focusing on the engineered graphene and its nanocomposites with the applications including supercapacitors, solar cells, thermoelectric power cells, electrochemical sensors, biosensors, environmental remediation, flame retardant polymer nanocomposites and graphene membrane separation. The synthesis methods and characterizations of graphene have been reviewed in several recent review literatures[40–42] and will not be detailed here. Instead, the physicochemical properties of the graphene and its nanocomposites are reviewed in detail. Then, from an engineering perspective, the practical applications of graphene and its nanocomposites in supercapacitor and solar cell electrodes, thermoelectric cells, electrochemical- and bio-sensors, heavy metal adsorbents, organic dye photocatalysts, polymer nanocomposite fillers and gas separation membranes are reviewed.

2. Physicochemical properties of graphene and graphene nanocomposites (GNCs)

Among the various unique physicochemical properties of graphene, the surface chemistry, electrochemistry, electron transport, mechanical property and optical transmittance are the major properties that most of the current applications are built on.

2.1 Surface chemistry

The abundant reactive oxygen-containing groups (carboxylic acid groups at the edges, epoxy and hydroxyl groups on the basal planes) in GO render it a good candidate for use in a wide range of applications. The chemical structure of GO is shown in Fig. 1. In most cases, GO served as a precursor for graphene fabrication, which was obtained from graphite oxidation and subsequent reduction to graphene through different methods including chemical reduction,[7] thermally mediated reduction[43,44] and electrochemical reduction.[45,46] Meanwhile, the hydrophilic functional groups on GO surface play a significant role in nanocomposites fabrication. On one hand, nanostructure growth could be initiated *via* covalent bondings between nanostructure precursor and GO surface groups and then grow following a specific pattern. On the other hand, basal and edge defects may leave behind after reduction, where precursors are preferred to nucleate and grow into nanostructures.

Graphene and carbon nanotubes share a similar surface feature and have many properties in common. It is difficult to differentiate each other from conventional spectral techniques. Raman spectroscopy is able to provide a powerful tool to differentiate between two different sp^2 carbon nanostructures, carbon nanotubes and graphene.[48] Fig. 2 shows the various Raman features including the G-band at ~1582 cm^{-1}, which is common to all sp^2 carbon forms, the radial breathing mode (RBM) that makes the diameter and optical transition energy analysis of nanotubes possible, edge-induced disordered D band[49] related to the presence of sp^3 defects, and G′ band arising from the two phonons with opposite momentum in the highest optical branch near the *K* point of the Brillouin zone.[50,51]

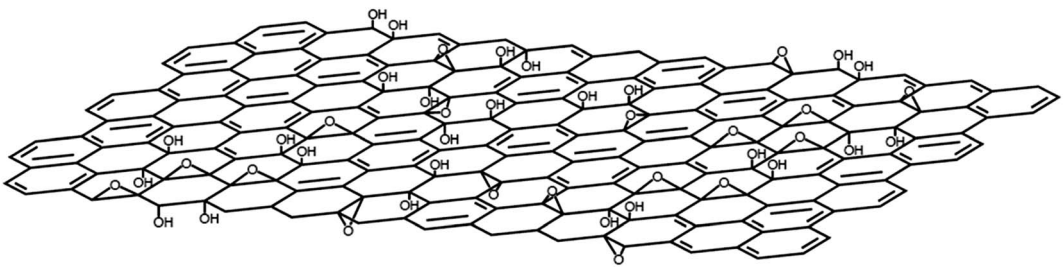

Fig. 1 Chemical structure of graphite oxide.[47] Reproduced from ref. 47 with permission.

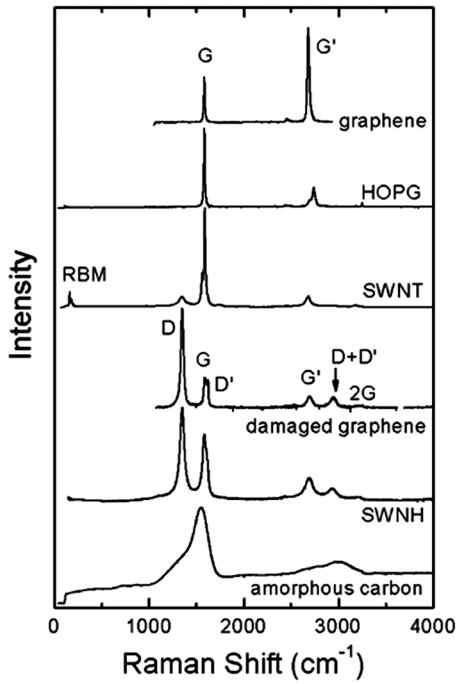

Fig. 2 Raman spectra from different types of sp^2 carbon nanostructures. The graphene-related structures are labeled next to their respective spectra. The main features (RBM and disorder-induced D, D′ and D + D′ bands; first-order Raman-allowed G band; and second-order Raman overtones G′ (2iTO) and 2G) are labeled in some spectra, but the assignment applies to all of them. The detailed analysis of the frequency, line shape, and intensity for these features gives the information about each respective sp^2 carbon structure.[48] Reproduced from ref. 48 with permission.

The presence of a sharp and symmetric G′ band is used as a fingerprint to identify single or bilayer graphene from multilayer graphene.[52] Both D and G′ bands are significant in providing information about the electronic and geometrical structure through the double resonance process.[48]

2.2 Electrochemical property

To reveal the advantages of graphene in potential applications in supercapacitor electrodes, electrochemical and biological sensors, the basic electrochemical behaviors should be first investigated to identify several important parameters such as electrochemical potential window, electron transfer rate, redox potential, *etc.*

Graphene exhibits a wide potential window of 2.5 V in 0.1 M phosphate buffer neutral solution.[53] This potential window is comparable to graphite and glassy carbon electrode (GCE). However, the charge-transfer resistance of graphene is significantly lower than that of graphite and GCE. Numerous studies have demonstrated that graphene exhibits very fast electron transfer rate, where a low peak-to-peak potential separation value (very close to the ideal value of 59 mV) is obtained in a single-electron electrochemical reaction.[54,55] The apparent electron transfer rate constant, K^0, is often used to determine the electron transfer rate quantitatively. Studies of graphene and GCE using $[Fe(CN)_6]^{3-/4-}$ reveal their K^0 of 0.49 and

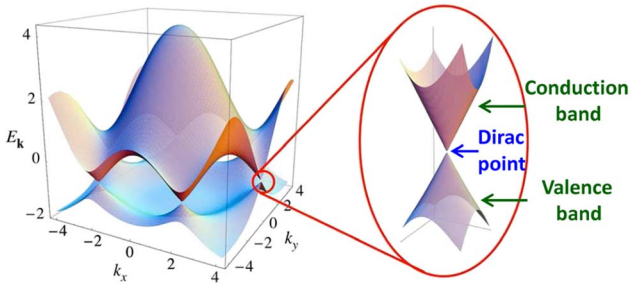

Fig. 3 Electronic dispersion of graphene.[57] Reproduced from ref. 57 with permission.

0.029 cm s^{-1}, respectively.[56] This significantly higher electron transfer rate of graphene indicates its favorable electron transfer than GCE.

2.3 Electron transfer property

Massive studies on graphene have made a significant progress on the understanding of its electronic structure and properties. Fig. 3 shows the well accepted electronic structure of graphene.[57] The conduction band and the valence band touch each other at six discrete points. These points are called *K* (Dirac) points and can be divided into two in-equivalent sets of three points each. The points within each set are all equivalent because they can reach each other by reciprocal lattice vectors. The two in-equivalent points are called *K* and *K*′ and form the valley isospin degree of freedom in graphene. The name valley isospin stems from the similarity of the vicinity of these points within a valley. The zoom shows that the dispersion relation close to the *K* points looks like the energy spectrum of massless Dirac particles. Both theoretical and experimental research efforts have indicated that the electronic energy dispersion in graphene is different from conventional 2D materials. Specifically, the electron and hole bands are linear near *K* and *K*′ points of the Brillouin zone in 2D graphene. However, the electron energy depends quadratically on the electron momentum in a conventional 2D system.[58] Various unusual transport phenomena are related to the fact that graphene behaves as a 2D electronic system, and the conduction and valence bands meet at the Dirac point, where the Fermi energy position is located.[59] As a Dirac fermion (fermions can be modelled with the well known Dirac equation) system with linear energy dispersion, electron–hole symmetry and pseudo spin (electrons have intrinsic degree of freedom), graphene promises intriguing electronic properties such as a high integer quantum Hall effect (a quantum-mechanical version of the Hall effect, observed in the 2D electron systems subjected to low temperatures and strong magnetic fields), the Klein paradox (unimpeded penetration of the relativistic particles that move with a near light speed through high and wide potential barriers),[60] an ambipolar electric field effect, along with ballistic conduction (transport of electrons in a medium with negligible electrical resistivity due to scattering) of charge carriers, *etc.* Owing to its approximately linear energy spectrum, carriers of low effective mass, and a zero band gap, the unique band structure of

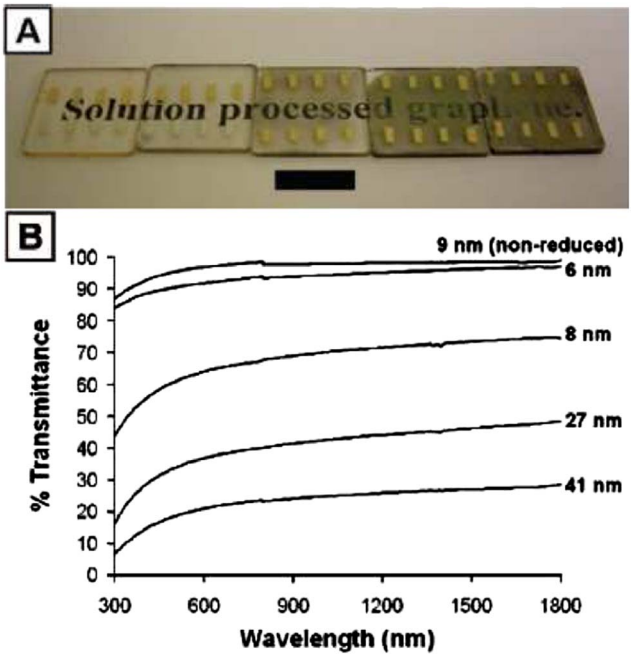

Fig. 4 (A) Photograph of an unreduced (leftmost) and a series of RGO films of increasing thickness. Black scale bar is 1 cm. (B) Optical transmittance spectra of the films in (A) with the film thickness indicated.[67] Reproduced from ref. 67 with permission.

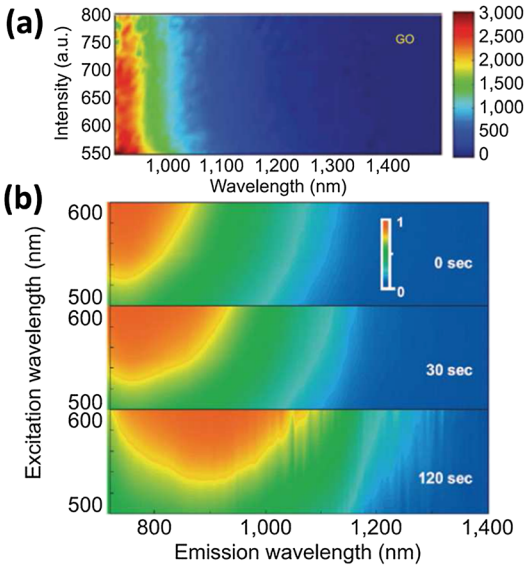

Fig. 5 (a) Fluorescence excitation-emission map of nanosized GO suspension with lateral flake size of 10–300 nm.[69] (b) Evolution of fluorescence excitation-emission map of GO thin-film samples (average flake size of ~100 μm^2) during hydrazine vapor exposure for 0 to 120 seconds.[70] Reproduced from ref. 70 with permission.

graphene makes it one of the best candidates for studying magntoresistance (MR). The MR is calculated using eqn (1):[61]

$$\mathrm{MR}(\%) = \frac{R(H) - R(0)}{R(0)} \times 100 \quad (1)$$

where $R(0)$ and $R(H)$ are the resistance at zero field and any applied field H, respectively.

2.4 Optical property

Graphene has great potential in electro-optical device applications due to the fascinating property, *i.e.*, coexistence of high mobility carrier and near-prefect optical transparency. In conventional transistors, electronic devices are operated at the so-called velocity saturation regime, at which carriers acquire the limiting velocity when they have enough kinetic energy to excite the optical phonons of the material. The optical phonon of graphene has much higher frequency (~1600 cm^{-1}) than those of inorganic semiconductors such as GaAs (~300 cm^{-1}) or Si (~500 cm^{-1}). Similarly, the intrinsic saturation velocity of graphene is higher, ~4 × 10^7 cm S^{-1}, than those in GaAs (~2 × 10^7 cm S^{-1}), Si (~1 × 10^7 cm S^{-1}), or InP (~0.5 × 10^7 cm S^{-1}). The unique electronic structure of graphene promises its distinct optical properties. Theoretical prediction reveals an excitonic absorption peak in the UV-region.[62] In the visible range, absorption spectrum is frequency independent.[63] Graphene has been manufactured into conductive transparent films with >70% transmittance.[64–67] Fig. 4(A) is a photograph of a series of GO films deposited on quartz slides, where the leftmost sample is an unreduced GO control and the rest are RGO films with thickness increasing from left to right. There is a marked transmission difference between the nonreduced and the reduced material that is due to the partial restoration of the π-electron system in the GO.[67] Fig. 4(B) displays the transmittance spectra, which show optical transmittance profile across the visible and near-infrared region of the spectrum.

Besides, unique fluorescent properties over a broad range of wavelengths have been discovered in GO and graphene owing to its heterogeneous electronic structure.[68] The fluorescence excitation-emission map of GO and GO after reduction by hydrazine vapor is displayed in Fig. 5. These unique properties make graphene an excellent candidate in applications such as transparent conductors, flexible displays, solar cell materials, and so on.

3. Design principles in diverse applications

3.1 Supercapacitor

Ragone plot, describing the relationship between energy density (E, W h kg^{-1}) and power density (P, W h kg^{-1}), has been widely used to evaluate the performance of different energy storage units. E and P can be calculated from eqn (2) and (3), respectively.[71]

$$E = \frac{1}{2} C_s (\Delta V)^2 \quad (2)$$

$$P = \frac{E}{t} \quad (3)$$

where C_s is the specific capacitance calculated from charge–discharge curve in F g^{-1}, ΔV is the potential drop during discharge in V, and t is the discharge time in h. To achieve high energy density, electrode materials are expected to have a large

C_s within a wide potential range. The C_s can be calculated from two electrochemical measurements, one is from cyclic voltammetry (CV) that can be calculated using eqn (4):

$$C_s = \frac{\int i\mathrm{d}V}{2 \times m \times \Delta V \times S} \quad (4)$$

where $\int i\mathrm{d}V$ is the integrated area of the CV curve, m is the mass of electrode material in g, ΔV is the scanned potential window in V, and S is the scan rate in V s^{-1}. The larger circled CV area at a specific scan rate, the better energy storage performance will be. The other is from galvanostatic charge–discharge that can be calculated by eqn (5)[72] from the discharge curves,

$$C_s = \frac{i \times \Delta t}{m \times \Delta V_1} \quad (5)$$

where i is the discharge current in A, Δt is the discharge time in s, and ΔV_1 is potential drop during discharge in V. The longer duration of discharge time at a specific current density, the better energy storage performance. All the current efforts are to enlarge the CV curve area and discharge time duration by advanced electrode material design.

3.2 Solar cell

Solar cell efficiency is the ratio of the electrical output of a solar cell to the incident energy in the form of sunlight. The energy conversion efficiency of a solar cell is the percentage of the solar energy to which the cell is exposed that is converted into electrical energy. Several factors affect a cell's conversion efficiency value, including its reflectance efficiency, thermodynamic efficiency, charge carrier separation efficiency and conduction efficiency values. The efficiency of any optoelectronic converter is given by eqn (6). The equation is more useful if it is expressed[73,74] as the product of a number of dimensionless groups, each of which refers to an energy dissipation process in the cell, *i.e.* eqn (7).

$$\eta_s = \left(JV / \int_0^{E_{max}} EN(E)\mathrm{d}E \right) \times 100\% \quad (6)$$

$$\eta_s = (1-R)\frac{E_g \int_{E_g}^{E_{max}} N(E)\mathrm{d}E}{\int_0^{E_{max}} EN(E)\mathrm{d}E} \frac{eV_{oc}}{E_g} \frac{J_{sc}/e}{(1-R)\int_{E_g}^{E_{max}} N(E)\mathrm{d}E} \frac{JV}{J_{sc}V_{oc}} \quad (7)$$

Each term indicates the reflection losses, light absorption efficiency, voltage factor, average quantum yield, and fill factor, respectively. And R is the ratio of the reflected to the incident energies, E_g is the threshold energy of absorption and $N(E)$ is the flux density of incident photons per unit energy interval. V_{oc} is the open circuit voltage, J_{sc} is short circuit current density, J is current density and V is the voltage.

3.3 Thermoelectric devices

Thermoelectric effect is the direct conversion of temperature differences to electric voltage and *vice versa*. Thermoelectric materials have wide potential applications in electricity generation, temperature measurement and temperature change of objects. The efficiency of a solid state thermoelectric device is determined by the magnitude of the figure of merit, ZT, which is given by eqn (8):[75]

$$ZT = S^2\sigma T/\kappa \quad (8)$$

S is the Seebeck coefficient or named thermopower, which measures the voltage induced in response to a temperature difference (V K^{-1} or μV K^{-1}), σ is the electrical conductivity in ohm^{-1} cm^{-1}, T is the absolute temperature of a given thermoelectric material, and κ is the thermal conductivity in W cm^{-1} K^{-1}. These parameters are strongly dependent on each other. To achieve a high ZT, a low thermal conductance κ together with a high Seebeck coefficient S and high charge conductance σ are required.

3.4 Sensors

Many electrochemical techniques have been developed and applied in sensors. Among them, two electrochemical techniques, amperometry titration and differential pulse voltammetry (DPV), are mostly used to determine the analyst concentration. The amperometry titration that monitors the current response with successive addition of reactants in a electrochemical system. In this case, the signal/noise ratio of at least 3 is required to define the lowest detecting limit. The other DPV method monitors the current that is measured immediately before each potential change and the current difference is plotted as a function of potential. By sampling the current just before the potential is changed, the effect of the charging current can be decreased and thus the sensitivity can be improved.

The idealized structure of graphene is completely two-dimensional, comprising a single layer of carbon atoms joined by sp^2 covalent bonds to form a flat hexagonal lattice. This extremely large specific surface area and excellent conductivity provide a great platform to construct advanced electrochemical and biological sensing devices. Especially, integrating functional nanostructures on graphene to make a hybrid structure has been a promising direction in the future. The design principles for future sensing devices are to reach high sensitivity (low detection limit), high reproducibility, large signal/noise ratio and fast response time.

3.5 Photocatalytic organic pollutants degradation

Graphene has low catalytic activity towards organic pollutants degradation, while it can be served as a platform to decorate catalytic structures that behaves better performance as a hybrid than any individual components. To realize an improved performance, several criteria in hybrid material design need to be considered especially the interfacial interaction between two materials. Taking graphene/TiO_2 for example, the hybrid structures have several advantages:[76] (i) increase catalyst adsorptivity. Organic dye molecules could transfer from the solution to the catalysts' surface and be adsorbed with offset face-to-face orientation *via* conjugation between dye and

aromatic regions of the graphene. (ii) Extend light absorption. The chemical bonds of Ti–O–C and good transparency of graphene render a red shift in the photoresponding range and facilitate a more efficient utilization of light for the catalyst. (iii) Suppress charge recombination. Graphene could act as an acceptor of the photogenerated electrons by TiO_2 and ensure fast charge transportation in view of its high conductivity, and therefore, an effective charge separation can be achieved.

3.6 Flame retardant composites

Since conventional polymeric materials are inflammable in most cases, they can not be directly used for structural materials and automobile parts unless being flame retardant (FR) treated properly. Usually, halogenated compounds,[77] metal hydroxides,[78,79] phosphorus-containing compounds,[80] silicon-containing compounds,[81] nitrogen-containing compounds,[82,83] carbon-nanofillers,[84–88] organoclay,[89–91] double-layer hydroxides,[92–94] and intumescent flame retardants[95,96] are commonly used to effectively reduce the flammability of polymeric materials. Due to the healthy issue and environmental protection requirements, the halogen-containing FR materials are prohibited and no longer favorable.[97] Meanwhile, the synergistic effect between at least two effective FR components such as nitrogen–phosphorus,[95,98,99] phosphorus–silicon,[81,100] became more effective in preparing FR polymer nanocomposites, and have been extensive studied and reported. Recently, graphene has shown great potential for fire safety applications, especially in terms of polymer nanocomposites.[101,102] Usually, a small additive amount of graphene, for example, <2 wt%, could significantly improve the thermal stability and reduce the heat release rate and toxic gases formation during the combustion of the polymer nanocomposites. The strong interfacial interaction between polymer and graphene forms a physical barrier which is the main reason for the reduced gas diffusion rate and polymer degradation.

Determining and assessing the flame retardant performance are of great significance for developing FR products. Usually, two major standard methods have been used: One is ASTM D2863-Limiting Oxygen Index (LOI)[103] for determining the minimum oxygen concentration to support candle-like combustion of plastics materials; and the other is ASTM D3801-UL-94 vertical burning test[104] for determining the comparative burning characteristics of plastic materials in a vertical position. It is necessary to satisfy certain requirements by using these two standard methods before one FR material, such as FR polymer nanocomposites, can be claimed as safe to be used for specific fire resistant purposes.

In addition to these two qualitative evaluations of FR property, another powerful quantitative assessment methods-oxygen combustion calorimetry is also commonly used to determine the detailed heat release related parameters such as rate of heat release (RHR), the single most important parameter in evaluating the fire hazard of material.[105,106] Specifically, Cone Calorimetry (ASTM E1354),[107] and Microscale Combustion Calorimetry (ASTM D7309)[108] are the most commonly used two techniques based on the oxygen consumption principle.

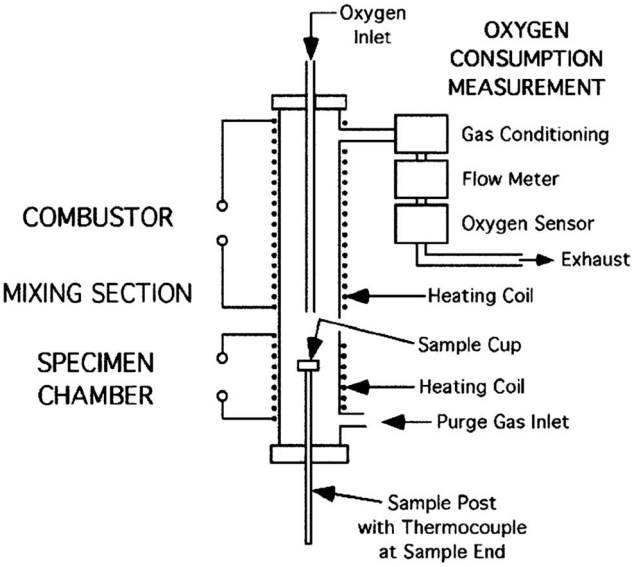

Fig. 6 The schematic diagram of Microscale Combustion Calorimetry.[108] Reproduced from ref. 108 with permission.

The Microscale Combustion Calorimetry is specifically designed for bench-scale small samples when only small amount sample is available or the large scale sample is costly. Eqn (9) shows the calculation of the specific RHR of one material:

$$\mathrm{RHR}\left(\mathrm{w\ g^{-1}}\right) = \frac{E\rho F}{m_0}\Delta[\mathrm{O_2}] \tag{9}$$

where E (approximately equals to 13.1 kJ per g O_2) is the average heat released by complete combustion of organic compounds per unit mass of oxygen consumed, ρ is density of oxygen at ambient conditions (g cm^{-3}), F is the volumetric flow rate of the combustion stream at ambient temperature and pressure measured at the terminal flow meter ($cm^3\ s^{-1}$), m_0 is the initial specimen mass (g), $\Delta[O_2]$ is the change in the concentration (volume fraction) of O_2 in the gas stream due to combustion measured at the oxygen sensor at time t ($cm^3\ cm^{-3}$). The $\Delta[O_2]$ is directly measured by the Microscale Calorimetry, and the RHR can be thus calculated based on the oxygen consumption.

The Cone Calorimetry is designed for testing macro-samples when large sample quantity is available. The advantage of Cone is that the smoke related parameters including smoke density, smoke release rate can be monitored simultaneously with measuring the RHR, for which the Microscale Calorimetry is unable to provide. On the other hand, the Microscale Calorimetry is very powerful and can be used for fast screening of the flammability for polymeric materials since only milligram level sample is required to run the test and only ~10 minutes to performe one test (concise structure is shown in Fig. 6). Meanwhile, the Microscale Calorimetry can also be applied to measure the RHR for flexible samples such as thin films and textiles or fibers, of which the Cone is unsuitable to test due to the high radiation flux used.

4. Applications

The unique chemical, electrochemical, electrical, and optical properties of graphene endow its wide applications in rapidly increasing academic communities and industry. The major focus of this review is to summarize the recent progress on graphene and its nanocomposites in five major application areas: (1) energy: supercapacitor and solar cell electrodes and thermoelectric power devices; (2) sensors: electrochemical sensors and biosensors; (3) environmental remediation: heavy metal adsorbents and photocatalysts for organic dye degradation, (4) flame retardant polymer nanocomposites, and (5) atomic thick graphene membrane separation.

4.1 Supercapacitors

Supercapacitor electrode is one of the major applications of graphene due to its extremely high electrical conductivity and large specific surface area. Graphene of different morphology and surface functionalities has been widely studied as high energy density electrodes for electrostatic double layer capacitors (EDLC). To further enhance the energy density, pseudoactive metal oxide and conductive polymer nanostructures are often introduced on graphene surface to form a composite electrode. In this session, pure graphene and hybrids (CNTs/graphene, metal oxides/graphene and conductive polymers/graphene) serving as supercapacitor and solar cell electrodes are discussed.

4.1.1 Graphene based supercapacitors. Graphene is often obtained from the reduction of GO by various reduction approaches[109] and has been demonstrated as a promising candidate for supercapacitors.[110–112] Recently, the capacitance of graphene was found to be 21 μF cm^{-2},[113] which sets the upper limit of EDLC for all carbon-based materials. Graphene is an ideal carbon electrode material for EDLC because it is capable of storing an EDLC capacitance value of upto 550 F g^{-1}, provided that the entire 2675 m^2 g^{-1} surface area is fully utilized.

The electrochemical performance of the graphene electrodes depends on several factors, such as electrolyte, operating potential window, surface functionalization, charging rate and *etc.* Generally, organic electrolyte allows energy storage unit to be operated in a wider potential window (>2.0 V), which is favorable for high energy density. Relatively smaller potential window is used in water based electrolyte (~1.0 V) and thus produced a lower energy density. Recently, Liu *et al.* reported an ultrahigh energy density and outstanding power performance of supercapacitors based on pristine graphene electrodes using ionic liquid as electrolyte.[114] The specific energy density reaches 85.6 W h kg^{-1} at room temperature and 136 W h kg^{-1} at 80 °C, measured at a current density of 1 A g^{-1}. The excellent performance of this material was attributed to the ability to make full utilization of the highest intrinsic surface capacitance and specific surface area of single-layer graphene by preparing curved graphene sheets that will not restack face-to-face. The curved morphology enables the formation of mesopores accessible to and wettable by ionic liquids electrolyte, which is capable of operating at a voltage >4.0 V that is much larger than 1.0 V in an aqueous electrolyte. In another work using 30% KOH electrolyte, lower energy density of 28.5 W h kg^{-1} was obtained within a smaller potential window of 1.0 V.[115]

The electrochemical behavior of graphene also largely depends on the surface properties. Brownson *et al.* studied the effect of surfactants and moieties on graphene and found that surfactant may contribute to a significantly enhanced capacitance of graphene electrode, while oxygen containing groups may be either detrimental or beneficial.[116] Even doubled capacitance in all-solid-state supercapacitors could be obtained from Nafion functionalized RGO (f-RGO) (118.5 F g^{-1} at 1 A g^{-1}) as compared to RGO electrode (62.3 F g^{-1} at 1 A g^{-1}). The enhanced performance was attributed to the facilitated ionic transport at the EDLC by means of the interfacial engineering of RGO by Nafion.[117]

During electrode preparation, binder is often used to process the individual graphene sheet into a compact electrode. However, binder is not desired due to its insulating feature. Monolithic graphene fiber has been fabricated from a directly drawing of CVD-grown graphene films *via* self-assembling, Fig. 7(a).[118] The graphene fiber exhibited high conductivity and uniform pore distribution, which showed a specific capacitance of 1.4 mF cm^{-2} in 1 M Na_2SO_4 electrolyte (10 mV s^{-1}).[118] Zhang *et al.* reported a hydrothermal method to reduce GO to

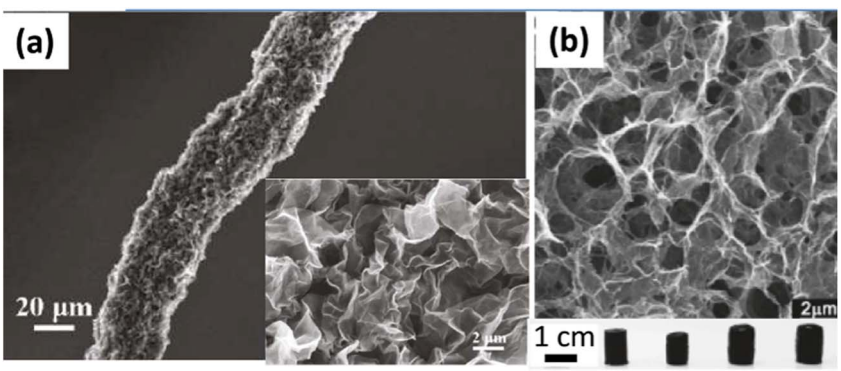

Fig. 7 (a) Graphene fiber drawn out of ethanol. The inset shows the wrinkled and porous structure,[118] (b) SEM image of porous graphene hydrogel and its photographs.[119] Reproduced from ref. 118 and ref. 119 with permission.

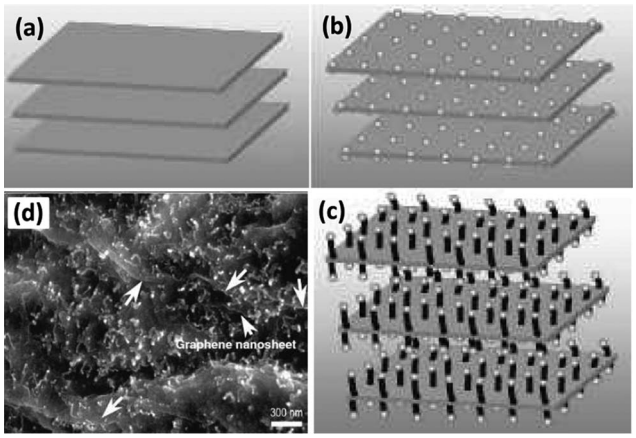

Fig. 8 Illustration of the formation of hybrid materials with CNTs grown in between graphene nanosheets, showing stacked layers of GO (a), catalyst particles adhered onto layer surface after deposition (b), CNTs in between graphene layers after growth (c) and SEM images of CNT/graphene sandwich structure (d) (Co catalyst: 16 wt%; carbon source: CO).[123] Reproduced from ref. 123 with permission.

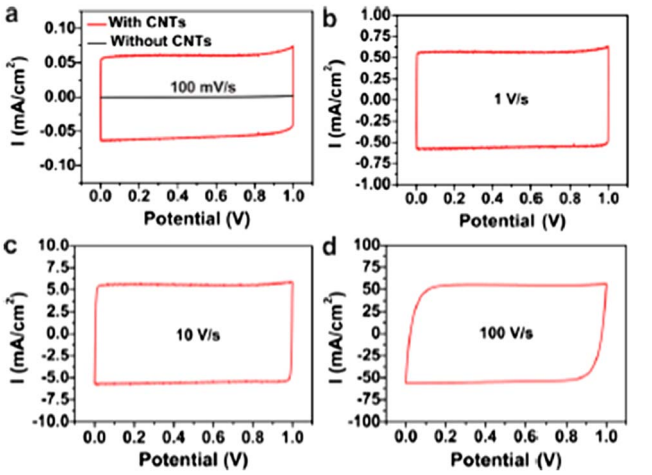

Fig. 10 CV characterizations of CNTCs/G-MCs using 1.0 M Na_2SO_4 as the electrolyte. (a) CVs of microsupercapacitors with and without CNTCs obtained at a scan rate of 100 mV s^{-1}; (b–d) CVs obtained at various scan rates of 1, 10, and 100 V s^{-1}.[124] Reproduced from ref. 124 with permission.

graphene hydrogels, Fig. 7(b).[119] The graphene hydrogels were further reduced with hydrazine (Hz) or hydroiodic acid (HI) to improve their conductivities. The supercapacitor based on the Hz-reduced graphene hydrogel exhibited a high specific capacitance of 220 F g^{-1} at 1 A g^{-1}, and this capacitance can be maintained for 74% as the discharging current density was increased up to 100 A g^{-1}.[119]

4.1.2 CNTs/Graphene based supercapacitors. Graphene can be easily agglomerated after drying due to the in-plane π–π interaction between graphene sheets, which is detrimental to the maintenance of high electrochemical activity. To fully utilize the surface area of graphene, CNTs are often introduced as a spacer between graphene nanosheets to avoid agglomeration. For example, Yu *et al.* prepared CNTs/graphene hybrid films by a self-assembling process using water soluble poly(ethyleneimine)-modified graphene sheets and acid-oxidized multiwalled carbon nanotubes (MWCNTs).[120] These hybrid films were demonstrated to possess an interconnected network of carbon structures with well-defined nanopores to be promising for supercapacitor electrodes, exhibiting a nearly rectangular cyclic voltammogram even at an exceedingly high scan rate of 1.0 V s^{-1} with an average specific capacitance of 120 F g^{-1}.[120] Lu *et al.* fabricated a similar flexible MWCNTs/graphene hybrid film by flow directed assembly from a complex dispersion of GO and pristine MWCNTs followed by the use of gas-based hydrazine to reduce the GO into graphene sheets.[121] Electrochemical measurements demonstrated that the MWCNTs/graphene film possessed a specific capacitance of 265 F g^{-1} at 0.1 A g^{-1} and a good rate capability (49% capacity retention at 50 A g^{-1}), and displayed an excellent specific capacitance retention of 97% after 2000 continuous charge–discharge cycles.[121] Even higher capacitance of 326.5 F g^{-1} at 20 mV s^{-1} was reported in a hierarchical CNTs/graphene architecture.[122]

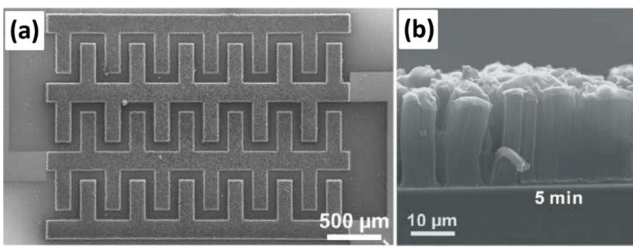

Fig. 9 (a) SEM image of a fabricated CNTCs/G microsupercapacitor, (b) cross-sectioned SEM images of CNTCs grown for 5 min.[124] Reproduced from ref. 124 with permission.

Besides the physical mixing of graphene and CNTs, *in situ* growth of CNTs on graphene to be a 3-D hybrid structure has been demonstrated a significantly enhanced capacitance. Fan *et al.* prepared a 3D CNT/graphene sandwich structure with CNT pillars grown in between the graphene layers by CVD, Fig. 8.[123] The unique structure endows the high-rate transportation of electrolyte ions and electrons throughout the electrode matrix and comprehensive utilization of pseudo and double-layer capacitance, resulting in an excellent specific capacitance of 385 F g^{-1} at 10 mV s^{-1} in 6 M KOH solution. After 2000 cycles, a capacitance increase of 20% of the initial capacitance was observed due to the increased effective interfacial area between electrode material and electrolyte with the increase of reaction time, indicating an excellent electrochemical stability of the electrode.[123]

Another interesting work on CNT carpets/graphene (CNTCs/G) based microsupercapaciotors has been reported recently by Lin *et al.*, the microstructure of device is shown in Fig. 9.[124] In this research, the CNTCs/G delivered a high volumetric energy density of 2.42 mW h cm^{-3} in ionic liquid, more than 2 orders of magnitude higher than that of aluminum electrolytic capacitors. The ultrahigh rate capability of 400 V s^{-1} enabled the microdevices to demonstrate a maximum power density of 115 W cm^{-3} in aqueous electrolyte. The CV curves maintained near-ideal rectangular shapes with symmetric charge and

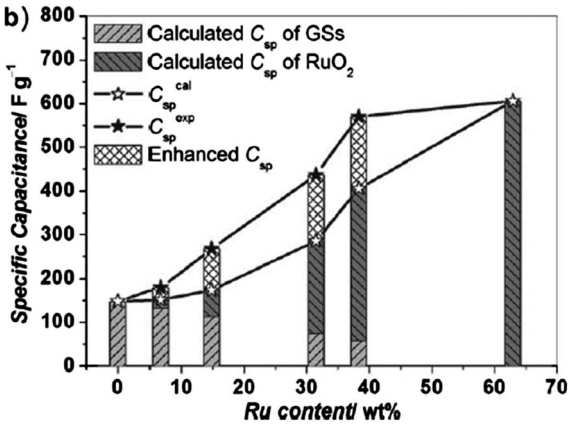

Fig. 11 Experimental and calculated specific capacitance of RuO_2/graphene (C_{sp}^{exp} and C_{sp}^{cal}), the calculated C_{sp}^{cal} of RuO_2/graphene is the sum of the calculated capacitances from graphene and RuO_2 components in composites. The inter-crossed, slashed-line squares indicate the enhanced capacitances ($C_{sp}^{exp} - C_{sp}^{cal}$) due to the synergistic effects.[22] Reproduced from ref. 22 with permission.

discharge current densities at a scan rate of up to 100 V s^{-1}, Fig. 10(a–d), suggesting a near perfect formation of EDLC.[124] These elevated electrical features were likely enabled by the seamless nanotube/graphene junctions at the interface of different carbon allotropic forms with a maximized electrical conductivity.

4.1.3 Metal oxides/graphene based supercapacitors. To enhance the capacitance, many approaches have been developed especially coating metal oxides and electroactive organic nanostructures on the graphene sheets with the aim to enhance the effective surface area and introduce additional pseudocapacitance. MnO_2 (600–700 F g^{-1})[125] and RuO_2 (720–900 F g^{-1})[126] are intensively investigated because of their higher theoretical capacitance values among the metal oxides. With the emphasis on metal oxide/graphene composites, different metal oxides RuO_2, MnO_2, Co_3O_4, NiO, V_2O_5, Fe_2O_3, Fe_3O_4, and *etc.*[22–32,127,128] have been incorporated in graphene and their electrochemical properties have been studied intensively.

Wu *et al.* incorporated hydrous RuO_2 NPs on graphene sheets to prepare a nanocomposite electrode.[22] The fine RuO_2 particles (5–20 nm) were anchored between graphene sheets to increase specific surface area. Benefiting from the combined advantages of graphene and RuO_2 in such a unique structure, RuO_2/graphene exhibited high specific capacitance (~570 F g^{-1}), enhanced rate capability, and excellent electrochemical stability (97.9% retention after 1000 cycles). The total specific capacitance of the composites was higher than the sum of specific capacitances of pure graphene and pure RuO_2 in their relative ratios (Fig. 11), which is indicative of a positive synergistic effect of graphene and RuO_2 on the improvement of electrochemical performance.[22]

MnO_2 nanostructure with different morphologies (nanoparticle, nano-needle, nanowire and nanosheet) has been integrated into graphene to study their morphology dependent performances. For examples, Huang *et al.* reported a specific capacitance of 308.5 F g^{-1} (at 5 mV s^{-1}) on the MnO_2 NPs/graphene composite electrode.[24] Using a layer-by-layer self-assembling technique, multilayer films of graphene and MnO_2 sheets have been successfully fabricated and exhibited a capacitance of 263 F g^{-1} at a discharge current density of 0.283 A g^{-1}.[130] The MnO_2 nanowire/graphene composite has been synthesized by Wu *et al.*, Fig. 12(a).[129] This composite was assembled into an asymmetric electrochemical capacitor with graphene, which can be cycled reversibly in the high-voltage region of 0–2.0 V and exhibit a superior energy density of 30.4 W h kg^{-1}. The symmetric capacitors based on graphene/graphene and composite/composite show much lower energy density of (2.8 W h kg^{-1}) and (5.2 W h kg^{-1}), respectively.[129] Fig. 12(b) shows the nano-needle like MnO_2 crystals *in situ* grown on the GO surface through a simple soft chemical route in a water-isopropyl alcohol system, this unique structure exhibits a capacitance of 216 F g^{-1} at 0.15 A g^{-1} discharge current density.[131] The relatively lower capacitance compared to previously mentioned MnO_2/graphene was due to the larger intrinsic resistance of GO. 3D conductive wrapping of MnO_2/graphene nanostructures with CNTs or conducting polymers on textile as flexible electrodes have been studied recently by Yu *et al.*[132] The specific capacitance of ~380 F g^{-1} was exhibited and excellent cycling stability was achieved with 95% retention over 3000 cycles.[132]

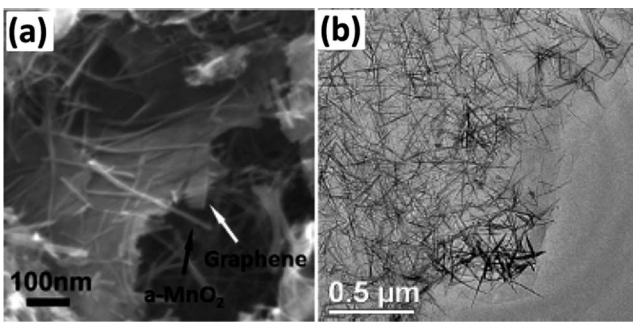

Fig. 12 (a) SEM of MnO_2 nanowire/graphene nanocomposite, and (b) TEM of MnO_2 nano-needle/graphene nanocomposite.[129] Reproduced from ref. 129 with permission.

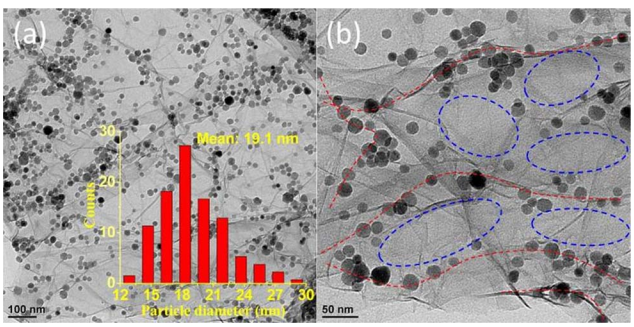

Fig. 13 TEM microstructures of the MGNCs. (a) The NPs are uniformly distributed on the graphene sheet (inset column figure shows the particle size distribution with an average size of 19.1 nm), (b) enlarged magnification of image (a) shows the favorable growth of NPs along the graphene edge indicated by the red dash line rather than the central area of graphene indicated by the blue dash circle.[133] Reproduced from ref. 133 with permission.

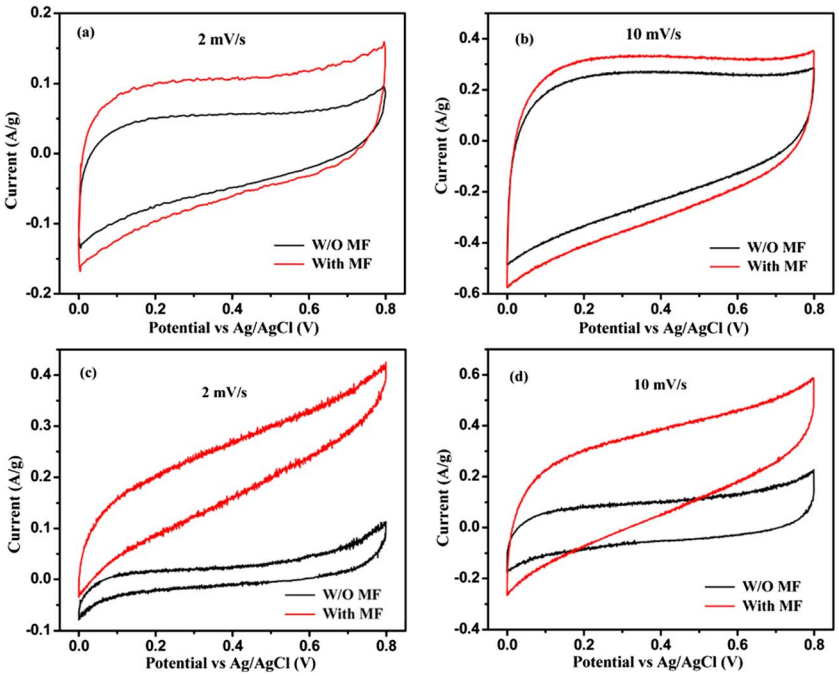

Fig. 14 Comparison of CV loops of graphene tested at a voltage sweeping rate of (a) 2, (b) 10 mV s^{-1}; and MGNCs tested at (c) 2 and (d) 10 mV s^{-1} in 1.0 M Na_2SO_4 electrolyte. "W/O MF" means the electrodes were tested without magnetic field, "With MF" indicates the measurement was tested in a magnetic field.[133] Reproduced from ref. 133 with permission.

The $Co(OH)_2$/graphene nanocomposite has been synthesized by a facile soft chemical approach. The electrochemical specific capacitance of the nanocomposite reached a value as high as 972.5 F g^{-1}, leading to a significant improvement in relation to each individual counterpart (137.6 and 726.1 F g^{-1} for graphene and $Co(OH)_2$, respectively).[134] Co_3O_4/graphene has been rapidly synthesized by microwave-assisted method. A maximum specific capacitance of 243.2 F g^{-1} has been obtained at a scan rate of 10 mV s^{-1}.[135] Monolayer NiO nanosheet/graphene composite synthesized *via* a self-assembling process exhibited a high specific capacitance of 525 F g^{-1} at a current density of 0.2 A g^{-1}.[136] Recently, Fe_3O_4 has been introduced into graphene with the aim to enhance the electrode capacitance and a much higher capacitance of Fe_3O_4/graphene nanocomposites (326 F g^{-1} (ref. 127) and 480 F g^{-1} (ref. 137)) is observed than that of either graphene or pure Fe_3O_4 NPs. Besides, V_2O_5 nanowires,[138] SnO_2 NPs,[25,139,140] TiO_2 NPs[72] have been used to as effective fillers in graphene to enhance the energy density and power density.

Most recently, Zhu *et al.* developed a one step thermal decomposition method to synthesize Fe_2O_3/graphene nanocomposites with a uniform particle distribution, Fig. 13. A creative study has been done on graphene and magnetic Fe_2O_3/graphene nanocomposites (MGNCs) with the aim to enhance the capacitance.[133] A small external magnetic field (0.072 T) has been introduced around the electrochemical cell and the electrochemical results demonstrated that the capacitance of graphene could be enhanced by 67.1 and 26.8% at a sweeping rate of 2 and 10 mV s^{-1}. Even larger enhancement of 154.6 and 98.2% was observed in MGNCs at the same sweeping rate of 2 and 10 mV s^{-1}. The CV curves of both materials in regular condition and magnetic field are displayed in Fig. 14. The

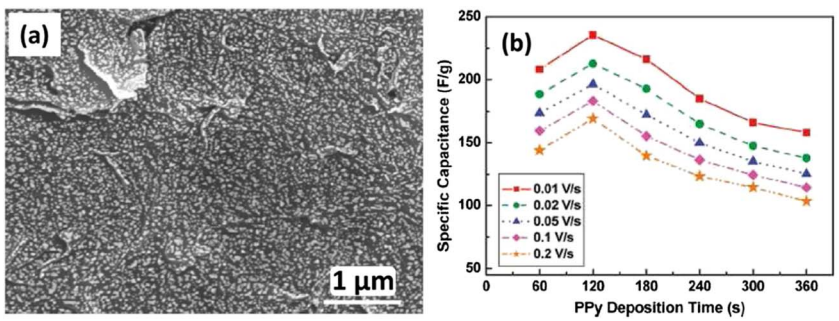

Fig. 15 (a) SEM images PPy/graphene after a 120 s electrodeposition, the white particles are PPy, (b) specific capacitance of all PPy/graphene electrodes by electrodeposition time, as determined by CV with different scan rates.[142] Reproduced from ref. 142 with permission.

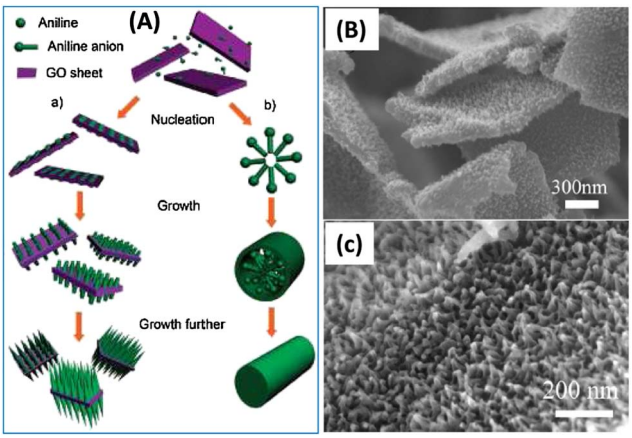

Fig. 16 (A) Schematic illustration of nucleation and growth mechanism of PANI-NW: (a) heterogeneous nucleation on GO nanosheets; (b) homogeneous nucleation in bulk solution. (B & C) SEM images of PANI/GO samples obtained at 24 h reaction interval.[33] Reproduced from ref. 33 with permission.

significant capacitance enhancement is attributed to the improved energy state of the electrons in a magnetic field. Besides, the magnetic field increased the electron transportation efficiency at the electrolyte/electrode interfacial area (double layer area) during electrochemical process and thus improved the capacitance performance.

4.1.4 Conductive polymer/graphene based supercapacitors. Conductive polymers possess many advantages that make them suitable for supercapacitors such as cost effective, environmental benign and high conductivity in a doped state and adjustable redox activity through chemical modifications. Conductive polymers offer capacitive behaviors though the redox process. When oxidation happens, electrolyte ions are transferred to the polymer backbone. The ions are released from the backbone into the electrolyte during reduction.[141] In this section, the most studied conductive polymers (PPy, PANI and PEDOT) in the applications of GNC electrodes will be discussed.

A unique nanoarchitecture has been established involving PPy and graphene nanosheets by an *in situ* polymerization. The specific capacitance value of the nanocomposites has been determined to be 267 F g^{-1} at a scan rate of 100 mV s^{-1}, which is much higher than that of pure PPy (137 F g^{-1}).[143] Using a pulsed electropolymerization technique, flexible and uniform PPy/graphene composite films were successfully fabricated, Fig. 15(a). Deposition time studies indicated an optimized deposition time of 120 s, where the highest specific capacitances of 237 F g^{-1} could be obtained, Fig. 15(b). This flexible nanocomposite film exhibited much higher energy density of 32.9 W h kg^{-1} than that of pure graphene (8.75 W h kg^{-1}) at a scan rate of 0.01 V s^{-1}.[142]

More work has been done on the PANI/graphene nanocomposite as supercapacitor electrodes. For example, flexible PANI film/graphene composite paper was fabricated *via* an *in situ* anodic electropolymerization process,[144] which was similar to the fabrication of PPy/graphene flexible composite film.[142] This composite electrode showed a favorable tensile strength of 12.6 MPa and a stable larger electrochemical capacitance of 233 F g^{-1} than that of pure graphene paper electrode (147 F g^{-1}).[144] Feng *et al.* introduced an electrodeposition method to synthesize PANI/graphene composite films by using GO and aniline monomer as the starting materials.[145] This composite film showed a high specific capacitance of 640 F g^{-1} with a retention life of 90% after 1000 charge–discharge cycles.

To ensure a good interfacial interaction between PANI nanowires and graphene/GO sheets, *in situ* polymerization of PANI nanostructures on GO surface is a feasible approach. PANI nanowire (PANI-NW) arrays were grown vertically on GO substrate *via* a soft chemical polymerization method.[33] The nucleation and growth mechanism of PANI-NW were schematically illustrated in Fig. 16(A). After 24 h reaction, aligned PANI-NW arrays are observed on the GO sheet, Fig. 16(B & C). The hierarchical nanocomposites possessed high electrochemical capacitance of 555 F g^{-1} and better stability than each individual component, showing a synergistic effect of PANI and GO. Similar soft chemical approach was used to prepare PANI nanofibers (PANI-NFs)/graphene nanocomposites and a specific capacitance of 480 F g^{-1} was obtained.[34] In a recent study,

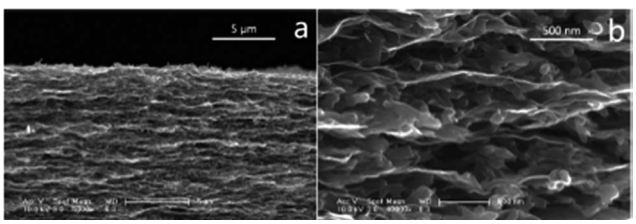

Fig. 18 (a & b) Cross-section SEM images of PANI/graphene nanocomposites.[146] Reproduced from ref. 146 with permission.

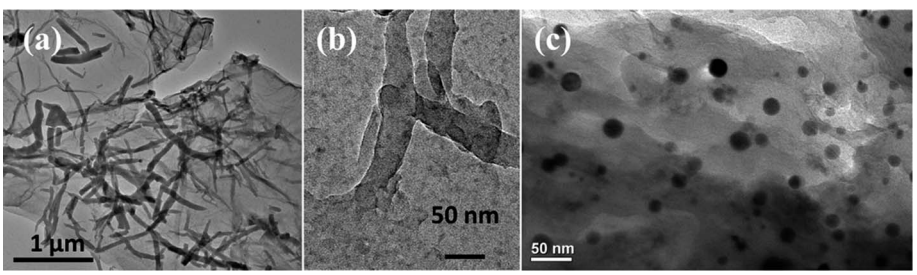

Fig. 17 (a) TEM microstructures of PANI-NF/GO nanocomposites, (b) interfacial interaction between PANI-NFs and GO sheet, and (c) SEM image of PANI-NP/GO nanocomposites.[35] Reproduced from ref. 35 with permission.

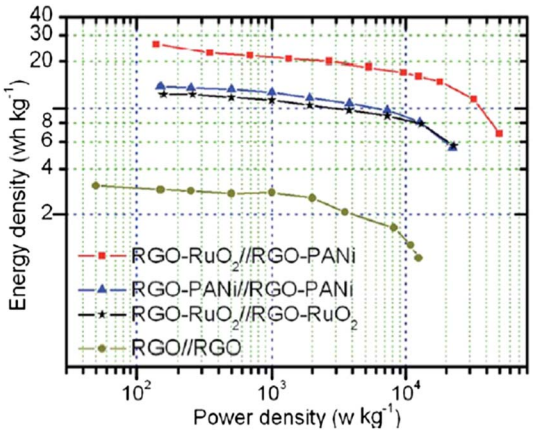

Fig. 19 Ragone plots of symmetric and asymmetric supercapacitors based on RGO, RGO/RuO_2 and RGO/PANI.[23] Reproduced from ref. 23 with permission.

PANI-NFs/GO nanocomposites with excellent interfacial interactions and elongated fiber structure were synthesized *via* a facile interfacial polymerization method, Fig. 17(a & b).[35] This polymerization method efficiently exfoliated the expanded layer structure of GO into individual sheets and thus significantly enhanced the specific surface area. The reduced diameter of PANI-NFs in PANI-NF/GO than that of pure PANI-NFs could shorten the diffusion distance and enhance the electro-active sites. The PANI-NFs/GO hybrid materials showed orders of magnitude enhancement in capacitance and energy density than that of individual GO and PANI-NF components. PANI NPs/GO was synthesized using a surface initiated polymerization method, Fig. 17(c). At the same weight loading of PANI in the composites, PANI NFs have shown higher energy density and long term stability than that of PANI NPs at higher power density.[35] Soft chemical polymerization was used to fabricate PEDOT/graphene nanocomposites as well and the specific capacitance of about 374 F g^{-1} was obtained.[39]

From a direct mixing and filtration of PANI-NFs and graphene, composite films were prepared from filtration.[146] The composite film has a layered structure, and PANI-NFs are sandwiched between graphene layers, Fig. 18(a & b). This conductive flexible composite film showed electrochemical capacitance of 210 F g^{-1} at a discharge rate of 0.3 A g^{-1}, which is significantly lower than the chemically grown PANI-NFs/GO composites due to the absence of effective interfacial interactions between both components.

Different from the conventional symmetric two electrode supercapacitor, an asymmetric supercapacitor was fabricated using RGO sheets modified with ruthenium oxide (RGO/RuO_2) or polyaniline (RGO/PANI) as the anode and cathode, respectively.[23] The capacitor exhibited a significantly improved capacitive performance in comparison with that of the symmetric supercapacitors fabricated with RGO/RuO_2 or RGO/PANI as the electrodes, Fig. 19. The improvement was attributed to the broadened potential window in an aqueous electrolyte, leading to an energy density of 26.3 W h kg^{-1}, about two-times higher than that of the symmetrical supercapacitors based on RGO/RuO_2 (12.4 W h kg^{-1}) and RGO/PANI (13.9 W h kg^{-1}) electrodes. In addition, a power density of 49.8 kW kg^{-1} was obtained at an energy density of 6.8 W h kg^{-1}.[23]

4.2 Solar cells

Solar cells have been developed for years and the primary material for today's solar cells is usually made out of high purity silicon. The high manufacturing cost of high purity silicon restricts its wide applications in market. Because of the high cost, researchers have been looking for affordable alternatives. Then, indium tin oxide (ITO) became more prevalent in electronic devices such as touch screen of smart phones. However, indium is still quite expensive. Recently, studies on graphene based solar cells are attracting ever increasing interest due to its unique features such as flexibility, weight lightness, higher mechanical strength and optical transparency.

Wang *et al.* demonstrated the concept of using transparent, conductive and ultrathin graphene films as window electrodes in dye-sensitized solar cells (DSSC) even in a nonoptimized state.[66] These graphene films are fabricated from exfoliated GO, followed by thermal reduction. The obtained films exhibited a high conductivity of 550 S cm^{-1} and a transparency of more than 70% over 1000–3000 nm. Furthermore, they showed high

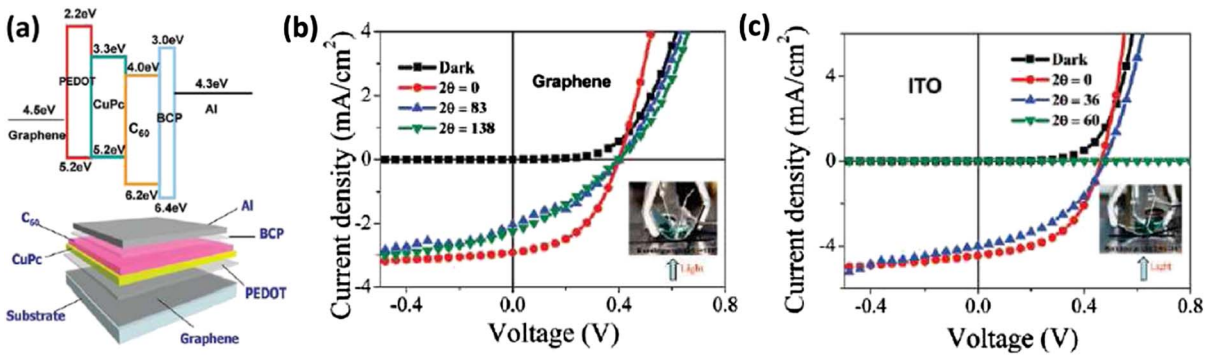

Fig. 20 (a) Schematic representation of the energy level alignment (top) and construction of the heterojunction organic solar cell fabricated with graphene as anodic electrode: CVD graphene/PEDOT/CuPc/C60/BCP/Al. (b) Current density *vs.* voltage characteristics of CVD graphene (b) or ITO (c) photovoltaic cells under 100 mW cm^{-2} AM1.5G spectral illumination for different bending angles. Insets show the experimental setup employed in the experiments.[12] Reproduced from ref. 12 with permission.

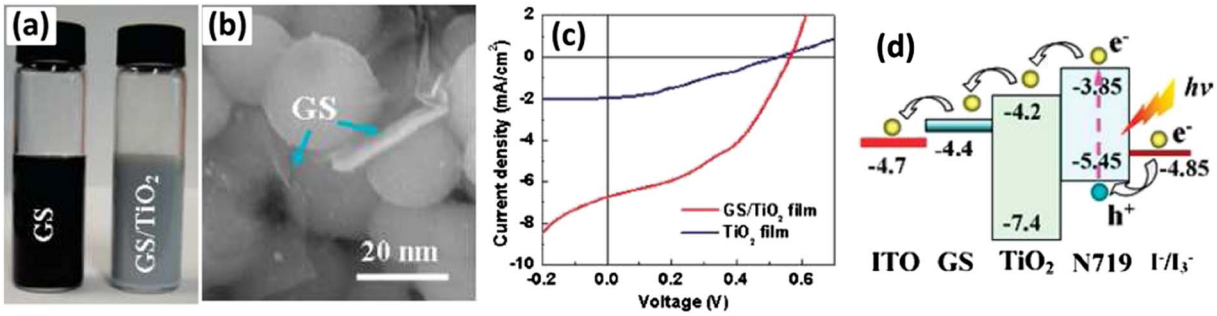

Fig. 21 (a) Photographs of an ethanol dispersion with RGO of sample 2 (left, 0.03 mg mL^{-1}) and TiO_2/graphene (GS) colloid suspension (right), (b) SEM images of the composite films deposited from the suspension with 0.03 mg mL^{-1} GS concentration, (c) current density–voltage (*J–V*) characteristics of DSSCs based on TiO_2/GS and TiO_2 nanoparticle films under 1 sun illumination. (d) Schematic energy-level diagram for the TiO_2/graphene DSSC.[153] Reproduced from ref. 153 with permission.

chemical and thermal stabilities. However, the relatively low overall power conversion efficiency of 0.26% needs to be improved for practical applications. Kalita *et al.* reported a controlled pyrolysis method to prepare graphene from botanical derivative camphor.[147] The graphene showed very good transparency in a wide range of wavelengths (0.3–2.0 μm). An organic solar cell was fabricated on a transparent graphene electrode with a transparency of 81% at 550 nm and a conductivity of 357 S cm^{-1} and higher conversion efficiency of 0.68% was obtained.[147]

A CVD method has been developed to fabricate continuous, highly flexible, and transparent graphene films that can be used in organic photovoltaic cells.[12] Graphene films as transparent electrodes were evaluated in organic solar cell heterojunctions (TCE/PEDOT:poly styrenesulfonate (PSS)/copper phthalocyanine/fullerene/bathocuproine/aluminum). Fig. 20(a) shows the typical construction of heterojunctions. Solar cells with CVD graphene and ITO electrodes were fabricated on flexible polyethylene terephthalate (PET) substrates and were confirmed to offer comparable performance, with power conversion efficiencies of 1.18 and 1.27%, respectively. Besides, CVD graphene solar cells demonstrated outstanding capability to operate under bending conditions up to 138°, whereas the ITO-based devices displayed cracks and irreversible failure under bending of 60°, Fig. 20(b & c). The excellent performance of the CVD graphene is attributed to its continuous nature, minimal surface roughness (~0.9 nm) and low sheet resistance down to 230 Ω sq^{-1} (at 72% transparency).[12] When functionalized graphene was applied as a catalytic counter electrode in dye-sensitized solar cell (DSSC), the cell efficiency was only 10% lower than platinum-based cells.[148] The material's catalytic activity increased with increasing number of the oxygen-containing functional groups. Therefore, a functionalized graphene sheet can also serve as a catalytic, flexible, electrically conductive counter electrode material in DSSC. Due to the non-conductive nature of GO, it can serve as efficient hole transport layer in polymer solar cells.[149] The incorporation of GO between the photoactive poly(3-hexylthiophene) (P3HT):phenyl-C61-butyric acid methyl ester (PCBM) layer and the transparent and conducting ITO led to a decrease in the recombination of electrons and holes and the leakage currents. This dramatic increase in the organic photovoltaics (OPV) efficiencies reached values that were comparable to the devices fabricated with the widely used PEDOT:PSS as the hole transport layer.[149]

Besides the pure graphene and functionalized graphene, graphene based hybrid materials have been widely studied to enhance the power conversion efficiency in solar cells. Recently, a CNTs/graphene hybrid has been fabricated as transparent conductors in polymer solar cell applications.[150] The hybrid delivered a resistivity of 240 Ω cm^{-1} at 86% transmittance. The composite was compatible with flexible substrates and did not require a sophisticated transfer process. And a power conversion efficiency of 0.85% was demonstrated in a polymer solar cell. The ZnO nanorods/RGO nanocomposites have been fabricated using electrochemical deposition method for hybrid solar cells with a layered structure of quartz/RGO/ZnO nanorods/P3HT/PEDOT:PSS/Au.[151] However, much lower conversion efficiency of ~0.31% was observed. As mentioned before, the CVD graphene transparent film exhibited comparable power conversion efficiency with ITO electrodes in organic photovoltaic (OPV) devices. While the challenges of CVD graphene came from the surface wetting between the hole-transporting layer and the graphene electrodes. Doping graphene with $AuCl_3$ can alter the graphene surface wetting properties such that a uniform coating of the hole-transporting layer can be achieved.[152] Furthermore, the doping both improves the conductivity and shifts the work function of the graphene electrode, resulting in an improved overall power conversion efficiency performance of 1.63% in the OPV devices.

Graphene sheets were incorporated in TiO_2 nanoparticle films *via* a molecular grafting method, Fig. 21(a & b), and deposited on conductive glass through electrophoretic deposition for DSSCs.[153] The graphene significantly improved the conductivity of the TiO_2 nanoparticle film by more than 2 orders of magnitude. And the power conversion efficiency for DSSC based on TiO_2/graphene composite films (1.68%) was more than 5 times higher than that based on TiO_2 alone (0.32%), Fig. 21(c). The schematic energy-level diagram for the TiO_2/graphene DSSC was shown in Fig. 21(d). It can be seen that the offset (~0.2 eV) between the conduction band minimum of TiO_2 and the work function of graphene is sufficient for charge separation. Meanwhile, the graphene will not block the injected electrons flowing down to the transparent electrode because its work function is higher than that of the ITO electrode.

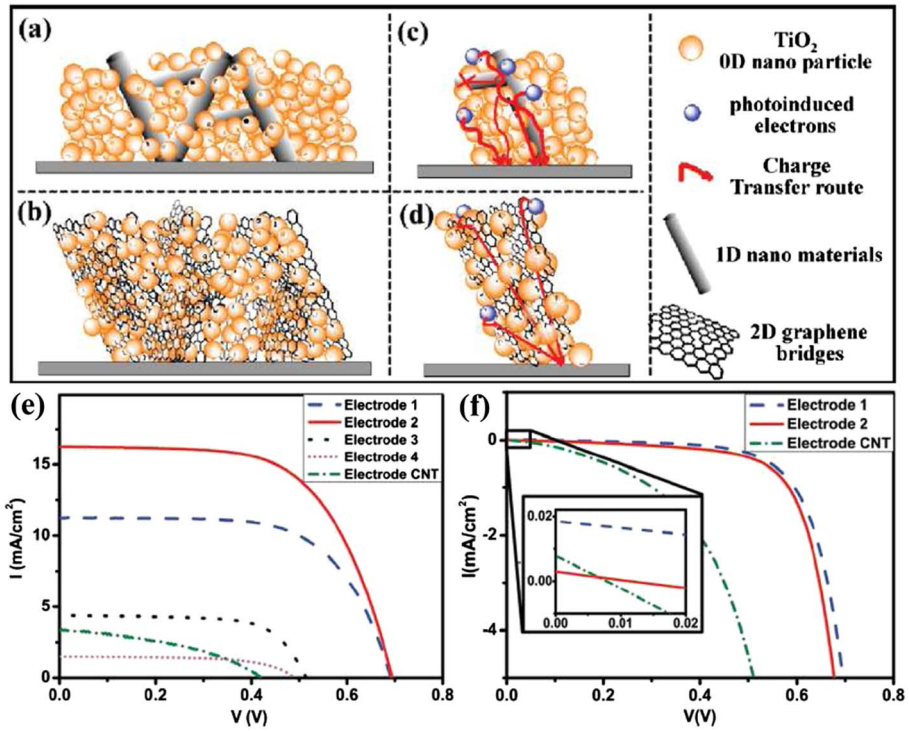

Fig. 22 Differences between (a and c) 1D and (b and d) 2D nanomaterial composite electrodes, (e) photocurrent–voltage characteristics of different electrodes. The sensitizer was N_3 (ruthenium dye). The cell active area was 0.20 cm^2, and the light intensity was 100 mW cm^{-2}, (f) back-current of different electrodes (the inset of the figure is the enlarge plot of back-current). Electrode 1: P25 (anatase TiO_2), electrode 2–4: P25/graphene nanocomposites with increasing graphene content.[154] Reproduced from ref. 154 with permission.

Therefore, the implanted graphene sheets serve as the electron acceptor and transporter for effective charge separation and rapid transport of the photogenerated electrons.[153]

A similar work has been reported *via* introducing graphene as 2D bridges into the nanocrystalline TiO_2 electrodes of DSSCs, which brought a faster electron transport and a lower recombination, together with a higher light scattering, Fig. 22(a–d).[154] On the basis of these advantages, the total conversion efficiency reached 6.97%, which was increased by 39%, comparing with the nanocrystalline TiO_2 photoanodes. Moreover, it was also much better than the TiO_2/CNT composite electrode. In graphene composite electrodes, the TiO_2 particles can anchor in the graphene better, and the photoinduced electrons can be captured and transferred by the graphene; however, with the CNT composites, there were less intermolecular forces and connections between TiO_2 and the CNT; therefore, the transfer barrier was larger and the recombination was much easier to happen, Fig. 22(e & f).[154]

4.3 Thermoelectric power devices

The high *ZT*, low cost, and rapid advances in the synthesis of nanoscale graphene derivatives make carbon-based materials a viable choice for thermoelectric applications. Right now, most of the current studies are focusing on the theoretical

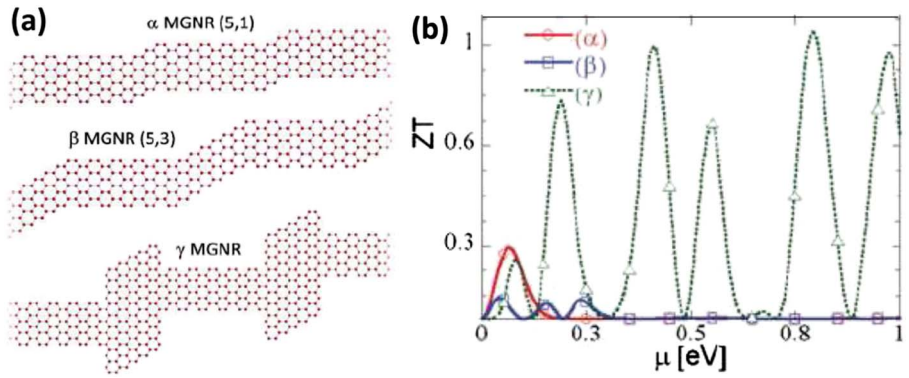

Fig. 23 (a) MGNR alternating armchair and zigzag elementary cells with the same width (α and β) and with different widths (γ), (b) *ZT* as a function of chemical potential μ.[157] Reproduced from ref. 157 with permission.

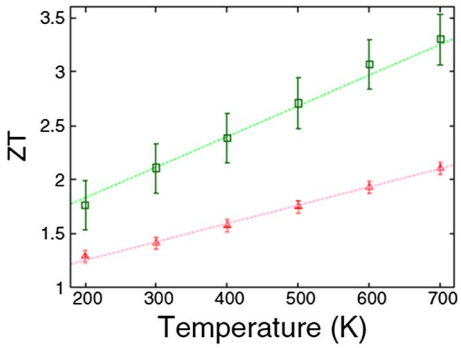

Fig. 24 Temperature dependence of *ZT* values for disordered AGANRs: $m = 5$, $\gamma = 0.45$ (triangles), and $m = 10$, $\gamma = 0.30$ (squares).[159] Reproduced from ref. 159 with permission.

investigations. For example, Ouyang *et al.*[155] found that the thermal conductivity of graphene nanoribbon can be reduced significantly (~30% of pure C^{12} graphene nanoribbon) by isotopic superlattice modulation, which depended on the superlattice period length and the isotopic mass. Sevinçli *et al.*[156] investigated electron and phonon transport through edge-disordered zigzag graphene nanoribbons (ZGNRs) using nonequilibrium Green functions. The edge disorder of graphene dramatically reduced phonon thermal transport while being only weakly detrimental to electronic conduction. The calculated thermoelectric *ZT* values of 0.39 (10 zigzag chains) and 4 (20 zigzag chains) at room temperature qualify ZGNRs as a very promising material for thermoelectric applications. Using the same simulation techniques, resonance tunneling of electrons was detected in graphene nanoribbons consisting of alternate zigzag and armchair sections, which resulted in a higher thermoelectric *ZT* at room temperature, Fig. 23.[157] Zheng *et al.*[158] used nonequilibrium Green function method and molecular dynamics simulations to study the thermoelectric properties of a series of armchair and zigzag graphene nanoribbons with narrow width. It is found that these nanoribbons are rather stable when the edge atoms are passivated by hydrogen and those with armchair edges exhibit much better thermoelectric performance than their zigzag counterparts. Moreover, the corresponding *ZT* value increases with decreasing ribbon width. By optimizing the doping level, a room temperature *ZT* of 6.0 can be achieved for the narrowest armchair nanoribbon.

Ni *et al.*[159] studied the thermoelectric property of graphene strips by using density functional theory calculations combined with nonequilibrium Green's function method. It is found that *ZT* can be remarkably enhanced five times by randomly introducing hydrogen vacancies to the graphene nanoribbon derivatives-armchair graphene nanoribbons (AGANRs). For 5 nm wide ribbons under certain conditions, *ZT* can be as high as 5.8 and depends on temperature linearly, Fig. 24. Even higher *ZT* value of 26 has been predicted from disordered examples of the narrowest AGANRs. Graphene doping effect on the polycrystalline Bi_2Te_3 has shown a lower thermal conductivity and higher *ZT* value than Bi_2Te_3 single crystals.[160]

4.4 Sensors

The atomic thickness of the graphene sheet is extremely sensitive towards the change of local environment, making it an ideal channel material in field-effect transistors used as electronic sensors. Here, electrochemical sensor and biosensor applications will be discussed separately.

4.4.1 Electrochemical sensors. As have mentioned in Section 2.1, the unique electrochemical properties of graphene make it a popular material for the development of novel electrochemical sensors. The wide potential window of 2.5 V in 0.1 M phosphate buffer solution[53] allows detection of molecules that have high oxidation and reduction potentials. The abundant edges and defects of graphene endow its faster electron transfer rate than conventional materials, such as GCE.[56] Therefore, superior electrochemical detection with graphene based electrodes is expected. Besides, the extremely large theoretical specific surface area of graphene (2675 $m^2\ g^{-1}$) provides a large effective reaction area. In most of the current studies, researchers prefer to use RGO as the sensor platform due to the following reasons: (1) RGO is electrical conductive as compared to the non-conductive GO, (2) the large number of edges and defects facilitate electron transfer, and (3) the

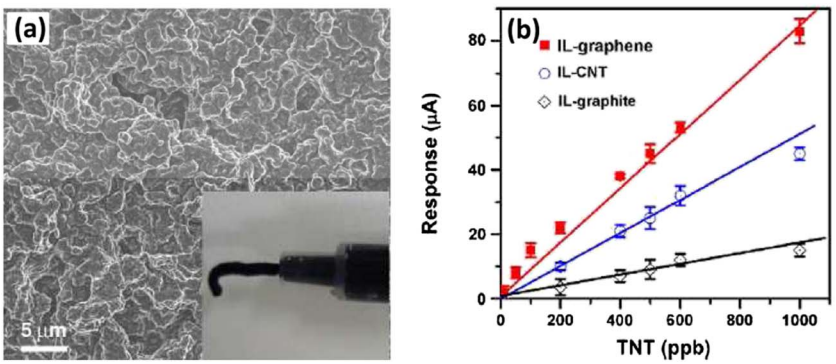

Fig. 25 (a) SEM image of IL-3D graphene composite, inset shows a photograph of IL-3D graphene gel, (b) calibration plots of IL–graphene electrodes towards TNT detection.[166] Reproduced from ref. 166 with permission.

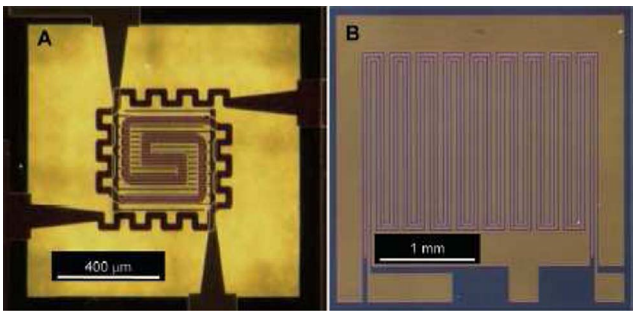

Fig. 26 Photographs of the sensor substrates used. (A) Micro hot plate (MHP) sensor showing interdigitated electrodes layered over heater leads. The electrode array is a 400 μm square with individual electrodes 10 μm wide with 10 μm gaps. The sensor is suspended on a thin silicon nitride membrane. (B) 4-point interdigitated electrode sensor. Two serpentine electrodes between the interdigitated electrodes are used for 4-point resistance measurements. The electrode array is 2.4 mm × 1.9 mm with 20 μm serpentine electrode widths, 40 μm interdigitated electrode widths, and 20 μm electrode gaps.[169] Reproduced from ref. 169 with permission.

conductivity and surface functional groups could be tuned for detection of specific chemical species.

Detection of explosive nitroaromatic compounds such as 2,4-dinitrotoluene (DNT) and trinitrotoluene (TNT) has received considerable attention during the last decade due to security reason and environmental concerns.[161,162] Electrochemical method for detecting nitroaromatic compounds showed great advantages due to its high sensitivity, fast response, low cost and feasibility for constructing portable devices.[163,164] Goh *et al.*[165] compared the response of single-, few-, and multilayer graphene nanoribbons and graphite microparticle-based electrodes toward the electrochemical reduction of TNT and found that few-layer graphene exhibited about 20% enhanced signal for TNT when compared to multilayer graphene nanoribbons. However, no significant difference was observed in the performance of graphene nanoribbons and graphite microparticles. The detecting limit of TNT in untreated seawater was established as 1 μg mL^{-1} (~1 ppm).[165] Ionic liquid (IL) modified graphene with large surface area and pronounced mesoporosity has been prepared for electrochemical TNT detection, Fig. 25(a).[166] The IL–graphene paste electrode provides higher electroactive surface area and lower charger transfer resistance compared with IL–CNT and IL–graphite paste electrodes. In TNT detection, the IL–graphene paste electrode showed low background current, high sensitivity of 1.65 μA cm^{-2} per ppb, low detection limit of 0.5 ppb and good reproducibility, which was much superior to the IL–CNT and IL–graphite past electrodes, Fig. 25(b).[166]

GNCs decorated with highly dispersive silver NPs showed a good electrocatalytic activity to nitrobenzene (NB), resulting in a sensitive detection of nitroaromatic compounds with an even lower detection limit of NB, DNT, TNT of 0.60, 0.21, 0.45 ppm, respectively.[167] Pt/graphene hybrid nanosheet was prepared through an one-step microwave-assisted heating procedure.[168] TNT was used as representative analyte to demonstrate the sensing performance of Pt/graphene nanocomposites. As a result, the Pt/graphene showed a wide linear range and low detection limit for TNT at ppb level.[168] The lowest limit of electrochemical TNT detection has been reported as 0.2 ppb using a graphene based film prepared by the electrophoretic deposition technique.[162] The excellent sensitivity performance was attributed to the effective adsorption ability and outstanding electrocatalytic activity toward the nitroaromatic explosive on the RGO film. Microscale electronic sensor devices based on chemically derived graphene has been constructed using spin coating to create single-layer graphene films on interdigitated electrode arrays, Fig. 26.[169] The device fabrication process was simple and easy to scale-up. And the results show a linear current *vs.* voltage curve for the detection of NO_2, NH_3, and DNT indicating the excellent sensitivity in all cases.

Sensors fabricated from RGO platelet film show faster response and lower noise levels than that of single walled CNT film. Robinson *et al.*[170] deposited an ultrathin continuous GO network, which was tunably reduced toward graphene by varying the exposure time to a hydrazine hydrate vapor. The sensors were capable of detecting 10 s exposures to simulants of the three main classes of chemical-warfare agents (hydrogen cyanide, chloroethylethyl sulfide and dimethylmethylphosphonate) and DNT at ppb concentrations. They demonstrated the important role of noise reduction by comparing the responses of single walled CNTs and RGO devices to 0.5 ppb DNT, a simulant for the explosive TNT. The lower noise levels in the RGO device lead to a notable increase in S/N ratio.[170] 4-nitrophenol with a detection limit of 0.02 μM at the S/N = 3 was also reported by using a GO film coated GCE.[171] GO film exhibited obvious electrocatalytic activity toward the reduction of 4-nitrophenol since it not only increased the reduction peak current but also lowered the reduction overpotential. Two possible reaction mechanisms were proposed in Fig. 27. The intermediate products of the reduction of 4-nitrophenol contained the free radical of OH, rather than OH− group. If the OH− existed, it can directly produce H_2O as reduction production in the acid conditions leading to an unbalanced chemical reaction. Therefore, OH· and O· radical generations were proposed in the electro-reduction process.[171] Other chemicals such as caffeine[172] and hydrazine[173] at low concentration level can be detected *via* graphene based electrochemical sensors. Besides, various gases (H_2, CO, NH_3, NO_2, acetone, and *etc.*)[174] and vapors (H_2O, nonanal, octanoic acid, trimethylamine, and *etc.*)[175] can be monitored using a graphene

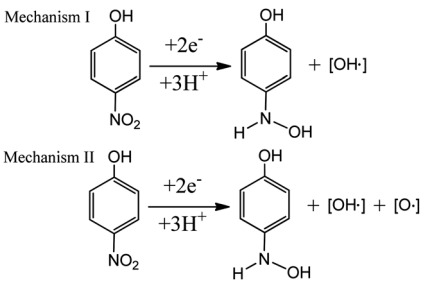

Fig. 27 The possible reduction mechanism of 4-nitrophenol at GO/GCE.[171] (mechanism II: H–N–H). Reproduced from ref. 171 with permission.

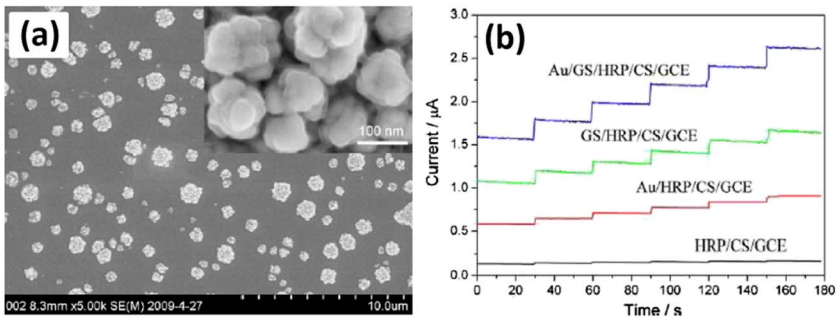

Fig. 28 (a) SEM image of Au/HRP/GS/CS modified electrode. The insert shows a cluster of Au NPs. (b) Current response to successive addition of 0.2 mM H_2O_2 of HRP/CS/GCE, Au/HRP/CS/GCE, GS/HRP/CS/GCE and Au/GS/HRP/CS/GCE in 0.1 mol L^{-1} PBS (pH = 6.5). Operating potential: −0.3 V. GS: graphene sheet.[188] Reproduced from ref. 188 with permission.

based device. More recently, a sensitive response of graphene to surface charge or ion density has been discovered in solution gated epitaxial graphene. This phenomenon points to its possible applications in ultrafast and ultralow noise biosensors or chemical sensors.[176]

4.4.2 Biosensors. Small graphene flakes can serve as advanced biosensors due to the enhanced electron transfer between the electrode and the active centers of the redox enzymes.[177] Moreover, RGO has intrinsic catalytic activity towards some small enzymatic products such as H_2O_2 and nicotinamide adenine dinucleotide (NADH), making it attractive for enzyme-based sensors. Besides, the high specific surface area of graphene provides a large effective reaction area and high capacity for enzyme loading. Moreover, decorating functional nanostructures on graphene sheets provides a superior platform to broaden the potential range of graphene for sensing species and improves the sensing activity as well.[178–181] Recently, a few review articles focusing on the potential application of graphene based materials in electrochemical and biological sensing have been published.[182–184] However, the ever increasing emphasis in GNCs and their significant roles in biosensing applications have not been realized yet. In this session, biosensing of both graphene and GNCs will be discussed.

Hydrogen peroxide (H_2O_2). The fast and reliable determination of H_2O_2 is important in many areas such as medicine, food control, environmental protection and biosensors. The study of H_2O_2 of electrochemical H_2O_2 sensors has attracted extensive attention. Brownson *et al.*[185] comparatively studied the H_2O_2 sensing performance of electrode modified by graphite, graphene, Nafion–graphite and Nafion–graphene, respectively. Interestingly, graphite exhibited a superior electrochemical response due to its enhanced percentage of edge plane sites when compared to graphene. However, when Nafion was introduced onto graphene and graphite modified electrodes, reorientation occurred in both cases, which was beneficial in graphene and detrimental in graphite.[185] Li *et al.* reported a nonenzymatic H_2O_2 sensor based on MnO_2/GO nanocomposite.[186] The MnO_2/GO based electrodes showed high electrochemical activity for the detection of H_2O_2 in alkaline medium. It displayed good performance along with low working potential, high sensitivity (38.2 μA mM^{-1} cm^{-2}), low detection limit (0.8 μM), and long-term stability (retain 90% of its original signal after 4 weeks storage), which could be attributed to the high surface area of GO that is suitable for MnO_2 nanoparticle deposition.[186] An even lower detection limit of 50 nM H_2O_2 was reported by Huang *et al.* on Au nanoparticles/amine-functionalized graphene composite film.[187] The enhanced performance was attributed to the synergistic effect of graphene–NH_2 and Au nanoparticles that facilitated the direct electron transfer between catalase and the underlying electrode. The biosensor exhibited more advantages, such as short response time (2 s), high sensitivity (13.4 μA mM^{-1}) and good reproducibility (relative standard deviation of 5.8%).[187] Zhou *et al.*[188] prepared a biocomposite H_2O_2 biosensor *via* a relatively complicated process. Specifically, graphene and horseradish peroxidase (HRP) were co-immobilized into biocompatible polymer chitosan (CS), then a GCE was modified by the biocomposite, followed by electrodeposition of Au nanoparticles on the surface to fabricate Au/graphene/HRP/CS/GCE, Fig. 28(a). The biosensor showed high sensitivity and fast response of H_2O_2, under the conditions of pH = 6.5, potential −0.3 V, Fig. 28(b). The time to reach the stable-state current was less than 3 s, and the linear range to H_2O_2 was from 5×10^{-6} to 5.13×10^{-3} M with a detection limit of 1.7×10^{-6} M (S/N = 3).[188]

Reduced nicotinamide adenine dinucleotide (NADH). NADH is an important coenzyme that involves in more than 300 dehydrogenase enzymatic reactions.[189] The electrocatalytic oxidation

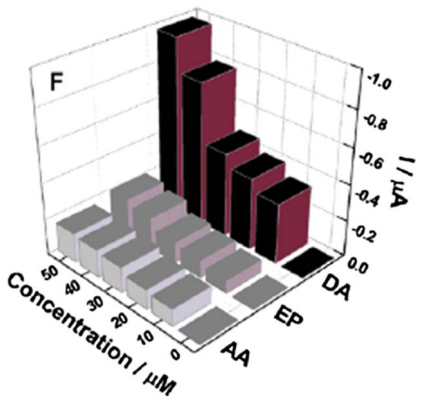

Fig. 29 Selective adsorption of DA, EP, and AA by GSCR-MIPs sensor.[193] Reproduced from ref. 193 with permission.

of NADH has been extensively investigated with the aim to dehydrogenase based biodevices. However, the high overpotential at bare GC electrode restricts its electrochemical detection due to the slow electron transfer and electrode fouling.[190] Shan *et al.*[191] reported a low potential NADH detection by designing an ionic liquid functionalized graphene (IL–graphene) biosensor. The NADH amperometric response at such a modified electrode was more stable (95.4% and 90% of the initial activity remaining after 10 and 30 min at 1 mM NADH solution) than that at bare electrode (68% and 46%). Moreover, the IL–graphene modified electrode exhibited good linearity from 0.25 to 2 mM and a high sensitivity of 37.43 mA M^{-1} cm^{-2}. This biosensor also showed rapid and highly sensitive amperometric response to ethanol with a low detection limit (5 μM).[191] Lin *et al.*[189] prepared a NADH sensor through noncovalent functionalization of graphene with water soluble electroactive methylene green. The oxidation peak of NADH at a bare GC electrode occurred at +0.55 V. However, it decreased to +0.40 and +0.14 V, respectively for electrodes of chemically modified graphene (CRG) and CRG functionalized with methylene green.

Ascorbic acid (AA), dopamine (DA) and uric acid (UA). Keeley *et al.*[192] prepared an AA sensor using graphene based electrodes by immobilizing graphene nano-sheets on pyrolysed photoresist film. This sensor was effective in the detecting range of 0.4 to 6.0 mM, with a 0.12 mM detection limit. The selectivity of the sensor was demonstrated using a commercially available vitamin C supplement.

Dopamine (DA), a simple organic chemical in the catecholamine family, is a monoamine neurotransmitter, which plays a significant role in the function of human metabolism. Since graphene is electroactive to both AA and DA, it is still a challenge to detect DA in the presence of AA. However, it is important to develop sensitive sensors for the determination of DA without the interference by AA. Recently, Kim *et al.*[194] developed a biosensor based on graphene modified GCE. The modified electrode exhibited capability in selective detection of DA in a sufficient amount of AA (1 mM). The observed linear range for the determination of DA concentration was from 4 to 100 μM. The detection limit was estimated to be 2.64 μM. Tan *et al.*[195] reported a nanomolar detection of DA in the presence of AA by using a β-cyclodextrin/graphene nanocomposite modified carbon electrode. This novel electrode showed low detection limit (5.0 nM), broad linear range (9.0×10^{-3}–12.7 μM), along with good ability to suppress the background current from large excess AA. Mao *et al.*[193] synthesized a novel composite electrode of graphene sheet/Congo red-molecular imprinted polymers (GSCR-MIPs) *via* free radical polymerization and applied as a molecular recognition element to construct DA electrochemical sensors. The selective detection of DA in a linear concentration range of 1.0×10^{-7}–8.3×10^{-4} M was obtained, which revealed a lower detection limit and wider linear response compared to some previously reported DA electrochemical MIPs sensors.[196–198] The selective detection of DA over AA and epinephrine (EP) was presented in Fig. 29.[193] Besides, the new DA electrochemical sensor exhibited excellent repeatability, which expressed a relative standard deviation of 2.50% for 30 repeated analyses of 20 μM DA.

TiO_2/graphene was also prepared *via* hydrothermal method and used to modify the GCE for selective DA detection.[179] The electrode exhibited remarkable electron transfer kinetics and electrocatalytic activity toward the oxidation of DA. The common interfering agent such as AA was significantly suppressed at this modified electrode, which resulted in good selectivity and sensitivity for electrochemical sensing of DA. Besides, Cu_2O/graphene nanocomposites were also synthesized *via* reduction of copper(II) in ethylene glycol.[199] The nanocomposite modified GCE displayed high electrocatalytic activity in giving an oxidation peak current that is proportional to the concentration of DA in the range from 0.1 to 10 μM, with a detection limit of 10 nM (S/N = 3).

Simultaneous determination of AA and DA has been reported by using Pt/ionic liquid/graphene nanocomposite modified electrode.[200] The difference between the two peak potentials of AA and DA oxidation was over 200 mV, which led to the distinguishing of AA from DA. The Pt/ionic liquid/graphene sensor in real sample analysis was also examined in human urine samples. Three independent oxidation peaks appear in urine sample containing AA and DA. A similar Pt/graphene modified GCE was created to simultaneously characterize AA, DA, and UA levels.[201] In the simultaneous detection of the three aforementioned analytes using CV, the electrochemical potential

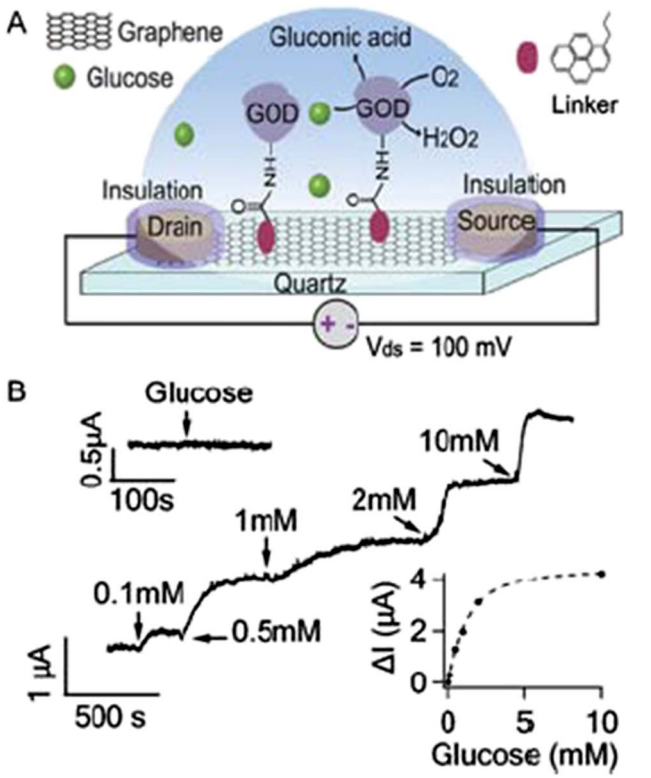

Fig. 30 (A) Schematic illustration of GOD functionalized graphene FET. (B) Current responses to the addition of glucose to various concentrations. The upper inset shows that GOD free graphene FET is not responsive to 10 mM glucose. The lower inset shows the response curve of the graphene FET to glucose fitted by an exponential function.[205] Reproduced from ref. 205 with permission.

differences among the three detected peaks were 185 (AA to DA), 144 (DA to UA), and 329 mV (AA and UA), respectively. In comparison to the CV results of bare GC and graphene-modified GC electrodes, the large electrochemical potential difference that is achieved *via* the use of the Pt/graphene nanocomposites was essential to the distinguishing of these three analytes.

The electrochemical detection of UA has been studied using poly-(diallyldimethylammonium chloride) (PDDA)-protected Au nanoparticles/graphene nanosheets (PDDA–Au/graphene) nanocomposites modified GCE.[202] PDDA–Au/graphene gave better performance for UA than Au/graphene obtained by adsorption, and the anodic peak current of UA obtained by cyclic voltammetry increased 102.1-fold in comparison to bare GCE under optimizing conditions. Differential pulse voltammetry was used to quantitatively determine UA. The linear range of UA was from 0.5 to 20 μM and the detection limit was 0.1 μM (S/N = 3) with a high sensitivity of 103.08 μA μM^{-1} cm^{-2}. Hong *et al.* prepared a similar Au/graphene nanocomposite by using 1-pyrene butyric acid functionalized graphene (PFG).[203] The linear range of UA was measured to be 2.0×10^{-6} to 6.2×10^{-5} M with a detection limit of about 2×10^{-7} M at a S/N = 3.

Glucose and glucose oxidase (GOD). Glucose is an important carbohydrate in biology, cells use it as the primary source of energy and a metabolic intermediate. Keeping the blood sugar (glucose) as close to normal as possible is very important to people who is suffering from diabetes since it helps to reduce the risk of long-term complications of diabetes. Therefore, portable devices based on advanced sensing techniques are in great demand for better monitoring and controlling of blood sugar level.

Enzymatic: Shan *et al.*[204] constructed a novel poly-vinylpyrrolidone-protected graphene/polyethylenimine-functionalized ionic liquid (PFIL)/GOD electrochemical biosensors, which achieved a direct electron transfer of GOD, maintained its bioactivity and showed potential applications for fabricating novel glucose biosensors with linear glucose response from 2 to 14 mM. Normally, the blood glucose level is maintained between about 4 and 6 mM. Therefore, the linear glucose response from 2 to 14 mM based on this novel graphene–PFIL modified electrode was enough and suitable for its practical applications in determining blood sugar concentration.[204] Huang *et al.*[205] demonstrated the use of large-sized CVD grown graphene films configured as field-effect transistors (FET) for real-time biomolecular sensing. Glucose molecules were detected by the conductance change of the graphene transistor as the molecules were oxidized by the glucose oxidase enzyme functionalized onto the graphene film. GOD was immobilized onto graphene film *via* a linker molecule (1-pyrenebutanoic acid succinimidyl ester), which on one end firmly attached to the graphene surface through π–π interaction with a pyrene group and on the other end covalently reacted with the amino group on the enzyme by an amide bond, Fig. 30(A). In a typical experiment shown in Fig. 30(B), an obvious increase of current was observed when glucose was added to the recording chamber.[205] Wang *et al.*[206] reported a facile strategy to prepare N-doped graphene by using nitrogen plasma treatment of graphene synthesized *via* a chemical method and used this material as biosensors for glucose detecting. This nitrogen doping played a critical role in regulating the electronic properties of graphene and showed fast direct electron transfer kinetics for GOD and the detecting limit of glucose was as low as 0.01 mM in the presence of UA and AA interferences. GOD/graphene/chitosan nanocomposite modified GCE[207] exhibited a wider linearity range from 0.08 to 12 mM glucose with a detection limit of 0.02 mM and much higher sensitivity (37.93 μA mM^{-1} cm^{-2}) as compared with other nanostructured supports. The excellent performance of the biosensor was attributed to large surface-to-volume ratio and high conductivity of graphene, and good biocompatibility of chitosan, which enhanced the enzyme absorption and promoted direct electron transfer between redox enzymes and the surface of electrodes. Wu *et al.*[180] prepared a bionanocomposite film consisting of GOD/Pt/graphene/chitosan for glucose sensing. With the electrocatalytic synergy of graphene and Pt nanoparticles to hydrogen peroxide, a sensitive biosensor with a detection limit of 0.6 μM glucose was achieved. The biosensor also had good reproducibility, long-term stability and negligible interfering signals from AA and UA. GOD/Au/graphene[208] was also synthesized for obtaining glucose biosensors, which exhibited a linear sensing response upto 30 mM with an excellent detection limit of 1 μM.

Nonenzymatic: besides the enzymatic glucose biosensors mentioned above, nonenzymatic biosensors were also developed. For example, Gao *et al.*[181] synthesized PtNi alloy/graphene nanocomposites *via* a facile one-step ultrasonication assisted electrochemical method and explored their applications for highly selective nonenzymatic glucose detection, Fig. 31(a–c).

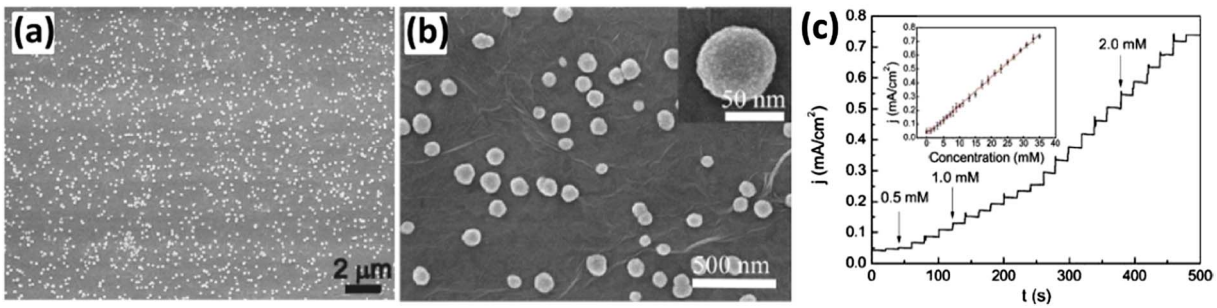

Fig. 31 (a) SEM image of PtNi/graphene nanocomposite, (b) magnified SEM images of (a) and (c) typical amperometric response of PtNi/graphene modified GCE to successive addition of 0.5, 1.0, and 2.0 mM glucose and the calibration curve (insert).[181] Reproduced from ref. 181 with permission.

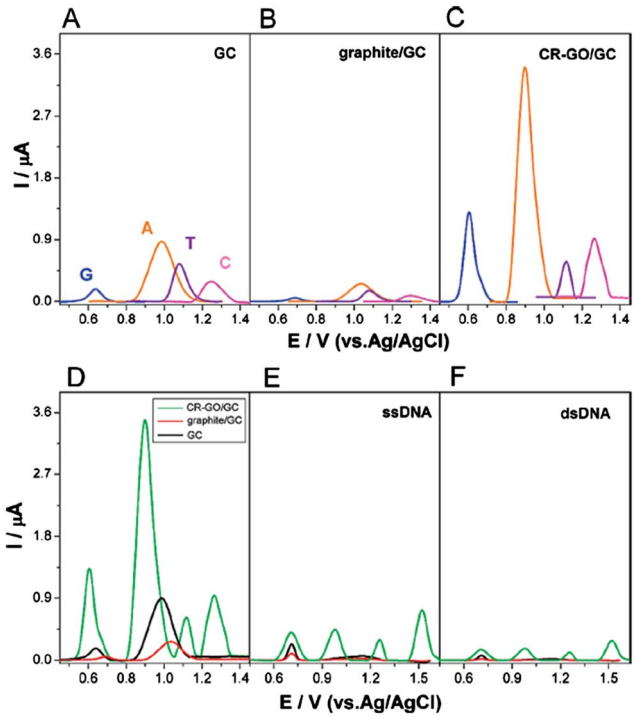

Fig. 32 (A) DPVs at the GC electrode for G (blue), A (orange), T (violet), and C (magenta), respectively. (B) DPVs at the graphite/GC electrode for G (blue), A (orange), T (violet), and C (magenta), respectively. (C) DPVs at the RGO/GC electrode for G (blue), A (orange), T (violet), and C (magenta), respectively. (D) DPVs for a mixture of G, A, T, and C at RGO/GC (green), graphite/GC (red), and GC electrodes (black). (E) DPVs for ssDNA at RGO/GC (green), graphite/GC (red), and GC electrodes (black). (F) DPVs for dsDNA at RGO/GC (green), graphite/GC (red), and GC electrodes (black). Concentrations for different species (A–F): G, A, T, C, ssDNA or dsDNA: 10 μg mL^{-1}. Electrolyte: 0.1 M pH 7.0 PBS.[53] Reproduced from ref. 53 with permission.

The current response of the sensor was linear to glucose concentration up to 35 mM with a sensitivity of 20.42 μA cm^{-2} mM^{-1} at a substantially negative potential (*i.e.*, −0.35 V). Operation under this potential eliminated the impact from the oxidation of common interfering species. This sensor with excellent sensitivity and selectivity also allowed for the reproducible detection of glucose in human urine samples. Palladium (Pd)/graphene nanocomposite also showed a very high electrochemical activity for electrocatalytic oxidation of glucose in alkaline medium.[209] The constructed biosensors were applied to the quantification of glucose with a wide linear range covering from 10 to 5 mM ($R = 0.998$) with a low detection limit of 1 μM. The experiment results also showed that the sensors exhibited good reproducibility and long term stability, as well as high selectivity with no interference from other potential competing species.

DNA, protein and cell. Sensitive, selective, rapid, and cost effective analysis of biomolecules is important in clinical diagnosis and treatment. There is enormous need for sensitive and selective detection of single nucleotide polymorphism of a DNA strand as this issue is related to many major diseases and disorders, such as Parkinson's and Alzheimer's disease. Zhou *et al.*[53] prepared a RGO modified GCE (RGO/GCE) electrode for labeling free electrochemical detection of four DNA bases (guanine (G), adenine (A), thymine (T), and cytosine (C)) in both the single-stranded DNA (ssDNA) and double-stranded DNA (dsDNA) at physiological pH without a prehydrolysis step. Differential pulse voltammetry (DPV) of G, A, T, and C was studied at GC, graphite/GC, and CRGO/GC electrodes at pH 7.0, Fig. 32(A–F).

Oxygenated defects on graphene play a significant role on biosensing.[210] Anodized epitaxial graphene, consisting of oxygen-related defects, is a superior biosensing platform for the detection of nucleic acids, UA, DA, and AA. Mixtures of nucleic acids (A, T, C, G) or biomolecules (AA, UA, DA) can be resolved as individual peaks using DPV. In fact, an anodized EG voltammetric sensor can realize the simultaneous detection of all four DNA bases in dsDNA.[210] Graphene modified electrode with an additional electrodepositing prussian blue (PB) layer can enhance the current response of the electrode in DNA

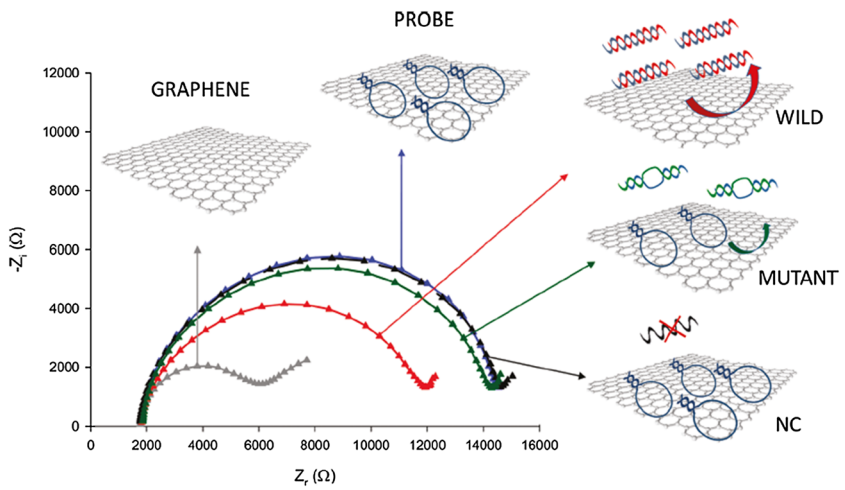

Fig. 33 Schematic of the protocol and Nyquist plots, $-Z_i$ *vs.* Z_r, of the graphene surface (gray), hpDNA (blue), complementary target (red), 1-mismatch target (green), and negative control with a noncomplementary sequence (black) (concentration of the DNA probes, 1×10^{-5} M; concentration of the DNA target, 3×10^{-8} M). All measurements were performed in 0.1 M PBS buffer solution containing 10 mM $K_3[Fe(CN)_6]/K_4[Fe(CN)_6]$.[215] Reproduced from ref. 215 with permission.

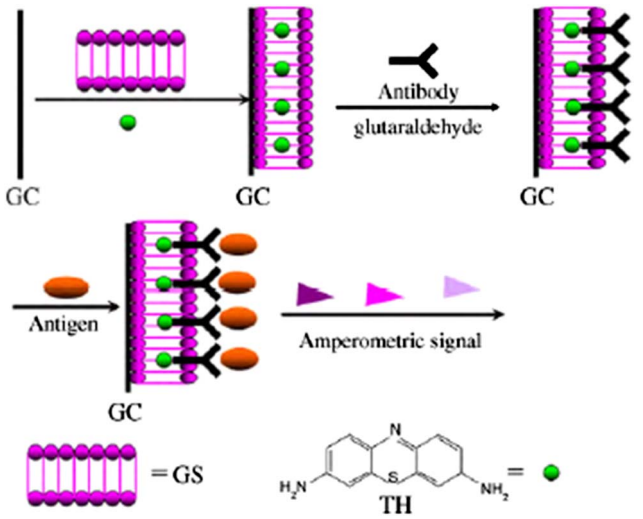

Fig. 34 Fabrication steps of the immunosensor. GC: glassy carbon.[218] Reproduced from ref. 218 with permission.

detecion.[211] Choi *et al.*[212] synthesized water soluble sulfonated RGO (SRGO) sheets and combined with DNA to form hybrids (SRGO–DNA) for the fabrication of electrical DNA sensors. The high sensing performance of SRGO–DNA sensors was demonstrated with the detection of DNA hybridization using complementary DNAs, single base mismatched DNAs, and noncomplementary DNAs, with results showing higher sensitivity and lower detection limit than those of RGO-based DNA sensors. These materials provided an effective way for electrical detection of DNA hybridization using miniature sensors without the labor-intensive labeling of the sensors and complex measurement equipments. Huang *et al.*[213] studied the sensing behavior of carboxylic acid functionalized graphene (graphene–COOH) towards adenine and guanine in DNA. On graphene–COOH modified electrodes, both adenine and guanine showed and increased oxidation peak currents with a negative shift of the oxidation peak potentials in contrast to that on the bare GCE. The modified electrode exhibited simultaneous detection of adenine and guanine with the peak separation as 0.334 V. The detection limit for individual determination of guanine and adenine was 5.0×10^{-8} and 2.5×10^{-8} M (S/N = 3), respectively. Recently, graphene-based single-bacterium resolution biodevices and DNA transistors have been developed and the sensitivity and specificity can be tuned through surface modification, polarity and morphology control.[214] Besides the CV and DPV techniques that have been widely used as general tools for the electrochemical biosensing, impedimetric sensing technique has been developed recently for rapid detection of single nucleotide polymorphism, which is correlated to the development of Alzheimer's disease.[215] Fig. 33 shows the Nyquist plots obtained in a whole impedimetric experiment and a general scheme of the graphene-based sensing platform.

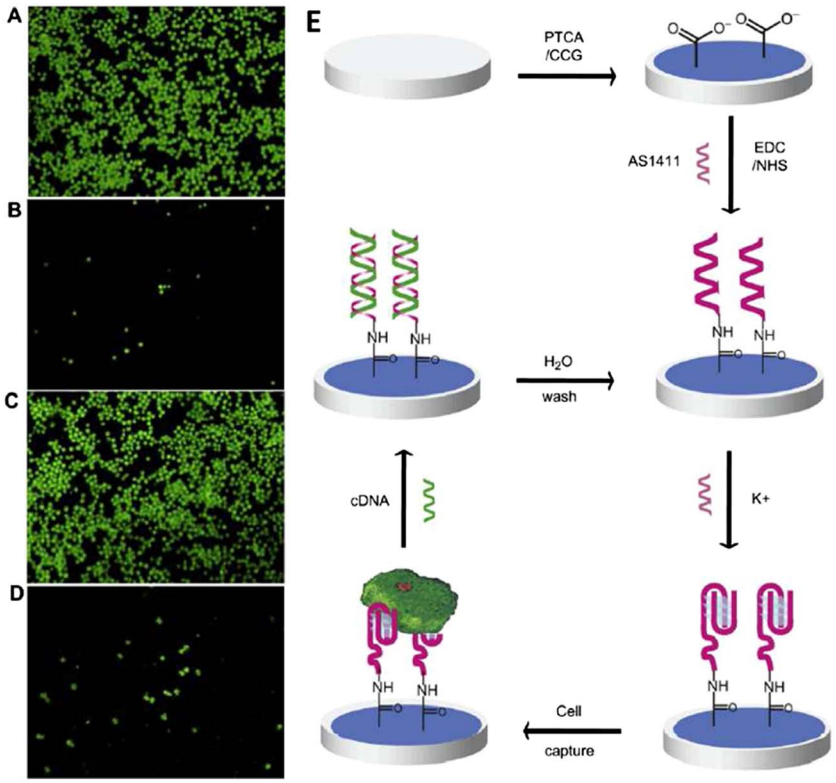

Fig. 35 Fluorescence images of (A) the perylene tetracarboxylic acid/graphene/aptamer surface treated with HeLa cells; (B) on-demand release of the cells after treatment with 5 mM cDNA; (C) after regeneration of the surface, then treated with HeLa cells; (D) on-demand release again. (E) Schematic representation of the reusable aptamer/graphene-based aptasensor. The sensor is constructed based on graphene-modified electrode and the first clinical trials II used aptamer, AS1411. AS1411 and its complementary DNA are used as a nanoscale anchorage substrate to capture/release cells.[220] Reproduced from ref. 220 with permission.

Nanocomposites also get involved in biosensing with enhanced performance. Bo *et al.*[216] prepared PANI-NW/graphene composite modified GCE for DNA detection. The resulting PANI-NW/graphene exhibited good DPV current response for the complementary DNA sequences. The biosensor exhibited a fast amperometric response, high sensitivity and good storage stability for monitoring DNA. The current response of the sensor increased linearly with the concentration of target from 2.12×10^{-6} to 2.12×10^{-12} M with an extremely low detection limit of 3.25×10^{-13} M.[216] Au nanoparticles were electrodeposited on the graphene/GCE with the aim to amplify the electrochemical signals.[217] The electrochemical responses of guanine (G), adenine (A), thymine (T) and cytosine (C) were investigated at Au/graphene/GCE, which showed more favorable electron transfer kinetics than at graphene/GCE, demonstrating the significantly synergistic electrocatalytic effect of graphene and Au nanoparticles. Synthetic sequence-specific DNA oligonucleotides were successfully detected and the established immobilization-free biosensors had the ability to discriminate single- or double-base mismatched DNA.

Wei *et al.*[218] constructed an immunosensor by immobilizing anti-alpha fetoprotein (anti-AFP) on graphene sheet and thionine modified GCE. The sensor fabrications were schematically illustrated in Fig. 34. Tests relating to the detection of AFP demonstrated that the sensors exhibited high sensitivity, wide linear range (0.05–2.00 ng mL^{-1}), low detection limit (5.77 pg mL^{-1}) and good long-term stability. TiO_2/graphene[219] nanocomposite modified GCE has been applied for electrochemical sensing of adenine and guanine. Significantly improved electrocatalytic activity and voltammetric response of TiO_2/graphene was observed comparing with that at the graphene. The TiO_2/graphene based electrochemical sensors exhibited wide linear range of 0.5–200 μM with detection limit of 0.10 and 0.15 μM for adenine and guanine detection, respectively. The excellent performance of this electrochemical sensor was attributed to the high adsorptivity and conductivity of the TiO_2/graphene nanocomposite, which provided an efficient microenvironment for the electrochemical reaction of these purine bases.

For cell detection, a label-free cancer cell electrochemical detection based on the first clinical trial II used aptamer AS1411 and functionalized graphene has been developed.[220] The schematic illustration of the reusable aptamer/graphene-based aptasensor is shown in Fig. 35. By taking advantages of AS1411 high binding affinity and specificity to the overexpressed nucleolin on the cancer cell surface, the developed electrochemical aptasensor can distinguish cancer cells and normal ones and detect as low as one thousand cells. With DNA hybridization technique, this DNA sensor can be regenerated and reusable for cancer cell detection.[220]

4.5 Environmental remediation

Water pollution has been a critical issue for over a decade due to the over exploring of natural resources and uncontrolled release of toxic pollutants (heavy metal ions, organic dyes, herbicides, pesticides and *etc.*). The unique surface chemistry and large specific surface area of graphene make it an attractive material for water purification, especially with a surface coating of functional nanostructures. Here, graphene and GNCs based adsorbents for heavy metal removal and photocatalysts for organic dye degradation are discussed separately.

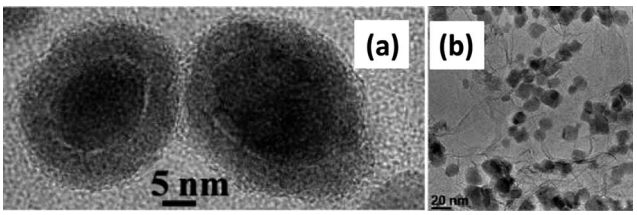

Fig. 36 (a) TEM image of Fe@Fe_2O_3/graphene nanocomposites showing the core@shell structure with a shell thickness about 5 nm,[19] (b) TEM image of Fe_3O_4/graphene nanocomposites.[18] Reproduced from ref. 18 with permission.

4.5.1 Heavy metal removal. Rapid industrialization has led to an increased discharged wastewater containing heavy metals (Cr, Cd, Hg, Pb, As, Co and Cu), which have detrimental effects on the environment and human health. Graphene and GO, with a large dimension in XY plane reaching several micrometers and extremely thin thickness (nanometer) in *Z*-axis, have large specific surface area and show promising applications as efficient adsorbents for heavy metal removal from polluted water.

Few-layered GO nanosheets were synthesized and used as sorbents for the removal of Cd(II) and Co(II) ions from aqueous solutions.[221] The abundant oxygen-containing functional groups on the surfaces of GO nanosheets played an important role on Cd(II) and Co(II) sorption. The maximum sorption capacities of Cd(II) and Co(II) on graphene oxide nanosheets at pH = 6.0 ± 0.1 and $T = 303$ K reached up to 106.3 and 68.2 mg g^{-1}, respectively. Yang *et al.* reported a huge Cu(II) absorption capacity of GO *via* an aggregation process.[222] The Cu(II) caused GO sheets to be folded and also to form large aggregates, which were most likely triggered by the coordination between GO and Cu(II). GO has a huge adsorption capacity for Cu(II), which was around 10 times of active carbon. For Hg(II) adsorption, GO was covalently modified with thiol groups by diazonium chemistry, and the modified GO adsorbs 6-fold higher concentration of aqueous Hg(II) than the unmodified GO.[223]

Arsenic is known for its toxicity and carcinogenicity to human beings. Arsenic can exit in both inorganic and organic forms. In general, inorganic arsenic compounds are more toxic than organic arsenic compounds, and arsenite [As(III)] is considerably more mobile and toxic than arsenate [As(V)].[224] Arsenate (*i.e.*, $HAsO4^{2-}$) is the primary anion in the aerobic surface water and arsenite (*i.e.*, H_3AsO_3 or H_2AsO^{3-}) is the primary species in the ground water. Functionalized graphene sheets (hydrogen induced exfoliation of GO followed by functionalization) were used as adsorbents for simultaneous removal of inorganic species of arsenic (both trivalent and pentavalent) with high concentrations.[225] The maximum adsorption capacities, using Langmuir isotherm, for arsenate and arsenite were found to be nearly 142 and 139 mg g^{-1}, respectively. GNCs decorated with metal oxide or metal hydroxides were also synthesized for fast arsenic adsorption. Recently, Fe@Fe_2O_3/graphene nanocomposite has been synthesized from a facile thermal decomposition method,

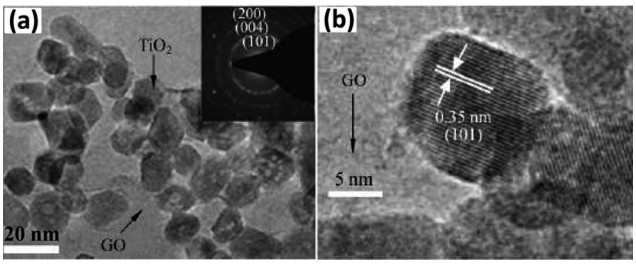

Fig. 37 (a) Low magnification, and (b) high magnification TEM images of TiO_2 nanocrystals grown on GO sheets.[237] Reproduced from ref. 237 with permission.

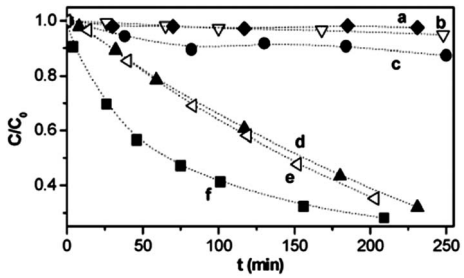

Fig. 39 Degradation of RhB (a) over Au/RGO in the dark, and (b) without catalyst, over (c) RGO, (d) P25, (e) Au/P25 and (f) Au/RGO under visible light irradiation.[239] Reproduced from ref. 239 with permission.

Fig. 36(a).[19] The nanocomposite showed a significantly higher adsorption capacity (11.34 mg g^{-1}) than the other adsorption values reported on the conventional iron oxide based adsorbents (~1 mg g^{-1}). Besides, the nanocomposites exhibited a strong magnetization and can be magnetically separated from the liquid mixture by a permanent magnet after adsorption. Fe_3O_4/graphene nanocomposites, Fig. 36(b), exhibited a high binding capacity for both As(III) and As(V) and showed near complete (over 99.9%) arsenic removal within 1 ppb.[18] $Fe(OH)_3$/GO composites were synthesized and evaluated as adsorbents for arsenate removal.[226] 95% arsenate can be adsorbed by the composite from water (concentration of arsenate is 51.14 ppm) with an adsorption capacity of 23.78 mg g^{-1}. This material demonstrated its effective arsenate removal in a wide range of pH from 4 to 9. For Cr(VI) adsorption, a core@double–shell (crystalline Fe as the core, Fe_2O_3 as the inner shell and amorphous Si–S–O compound as the outer shell) structure has been decorated on graphene sheet for fast Cr(VI) adsorption.[17] The nanocomposite has shown an extremely fast Cr(VI) removal from polluted water (within 5 min) with a high removal efficiency (1.03 mg g^{-1}).

4.5.2 Organic dye adsorption/degradation

Adsorption. Fe_3O_4/graphene nanocomposites were used as efficient adsorbents for organic dye removal, which were synthesized from solvothermal[227] and *in situ* coprecipitation[228] processes. The solvothermal synthesized Fe_3O_4/graphene exhibited excellent removal efficiency for Rhodamine B (RhB, >91%) and malachite green (>94%) and could be rapidly separated from aqueous solution by an external magnetic field. The real industrial waste water and lake water tests revealed its efficiency for removing dye pollutants.[227] The adsorption performance of coprecipitated Fe_3O_4/graphene was tested using an organic dye fuchsine as the adsorbate. And a very high maximum adsorption capacity of 89.4 mg g^{-1} was achieved.[228]

Photodegradation. Photodegradation process of organic pollutants has attracted increasing attention during the past decades. Among various strategies, TiO_2-based materials have been the most promising candidates for photocatalytic decontamination.[229] Particularly, the composites of TiO_2 and carbon were currently being considered as potential photocatalysts in the purification of air and water.[230–233]

TiO_2 (P25)/graphene composite can be prepared from physical mixing[234] or hydrothermal reaction.[76,234,235] In the visible light photocatalytic degradation of methylene blue (MB), about 70% MB was degraded by using P25/graphene composite after 5 h irradiation. In contrast, only 10% MB was degraded for pure P25.[234] TiO_2 sheets/graphene composites with large fraction of exposed anatase TiO_2 (001) facets were fabricated *via* molecular grafting method.[236] In comparison with commercial P25 and TiO_2 nanosheets, the composite exhibited significant improvement in photocatalytic degradation of the azo dye Rhodamine B (RhB) under visible light irradiation. The enhancement of photocatalytic activity and stability was attributed to the effective charge anti-recombination of graphene and the high catalytic activity of (001) facets. Graphene composites decorated

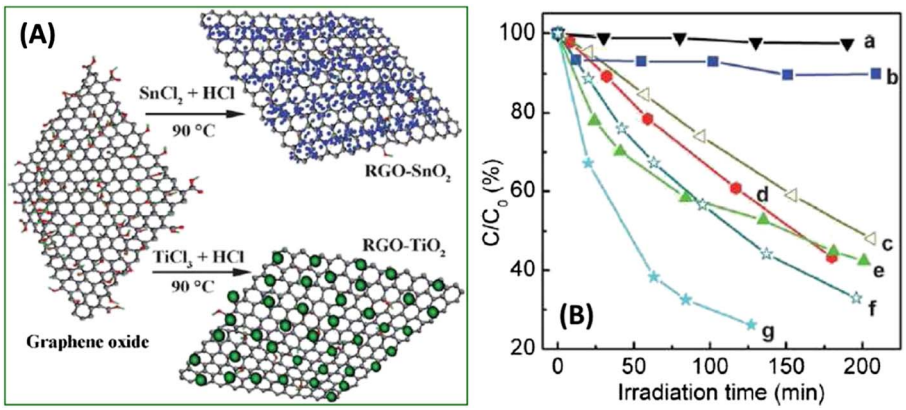

Fig. 38 (A) A scheme showing the preparation of samples SnO_2/RGO and TiO_2/RGO. (B) Degradation of RhB (a) without catalyst, with (b) RGO, (c) TiO_2/RGO, (d) P25, (e) SnO_2/RGO, (f) TiO_2/RGO-400, and (g) SnO_2/RGO-400.[238] Reproduced from ref. 238 with permission.

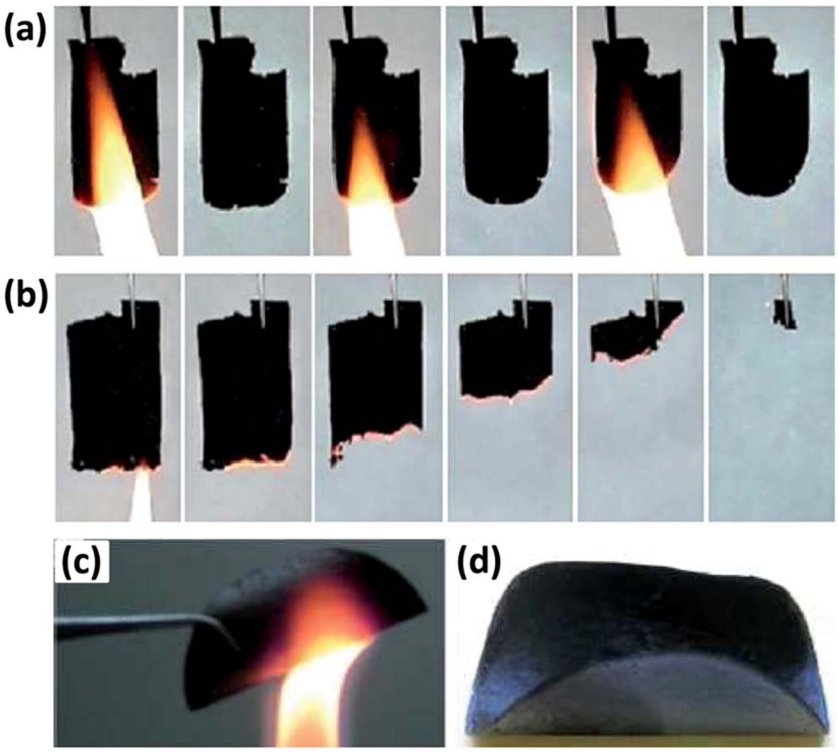

Fig. 40 (a) Snapshots showing flame treatments on RGO film with intervals of 3 to 4 s. The film was first exposed to a natural gas flame for a few seconds. The burned part turned red hot but didn't propagate, and was quenched after the flame was removed. No combustion occurred even after multiple flame treatments, clearly showing the high thermal stability of RGO. (b) Snapshots showing flame treatment on a RGO contaminated with KOH salts (1 wt%). The flame immediately triggered the self-propagating combustion in the film, which suggests that potassium salts can significantly reduce the thermal stability of RGO. Time intervals between the frames are 0.32 s, 1.82 s, 2.5 s, 2.5 s and 2.5 s, from left to right.[250,253] (c) Photographs of the MMT–RGO hybrid films (with initial thickness of 0.05 mm) exposed to open flame. (d) Digital image showing the MMT–RGO hybrid film after flame treatment.[251] Reproduced from ref. 251 with permission.

with highly crystalline anatase TiO_2 (Fig. 37) also demonstrated superior photocatalytic activity in degradation of RhB over other TiO_2 materials, showing an impressive 3-fold photocatalytic enhancement over P25.[237]

RGO was modified with SnO_2 and TiO_2 *via* a direct redox reaction between the GO and the reactive cations Sn^{2+} and Ti^{3+}, respectively, forming SnO_2/RGO and TiO_2/RGO composites, Fig. 38(A).[238] The photocatalytic activity of both composite samples was evaluated using the degradation of RhB under visible light irradiation. RhB was observed to be very stable under visible light irradiation without the presence of a photocatalyst, Fig. 38(B). It was slightly degraded in the presence of RGO. However, in the presence of catalysts SnO_2/RGO and TiO_2/RGO, the degradation was remarkably enhanced with rate constants of about 6.2×10^{-3} min^{-1} for SnO_2/RGO and 3.6×10^{-3} min^{-1} for TiO_2/RGO, significantly higher than that of RGO (3.9×10^{-4} min^{-1}). In addition, photocatalyst SnO_2/RGO performed better than and TiO_2/RGO and commercial product P25.[238]

Besides the widely studied TiO_2 nanostructures, other metals and metal oxides were also integrated on graphene surface to form high performance nanocomposites for organic dye degradation. Au/graphene nanocomposites have been prepared[239,240] and have shown even greater RhB degradation performance as compared to TiO_2, Fig. 39, due to the following features: (1) high adsorption ability toward organic dyes, (2) strong π–π interaction with dye chromophores, (3) efficient photosensitized electron injection, and (4) slow electron recombination.[239] Recently, ZnO/graphene (ZGC) was synthesized *via* a chemical deposition route and the corresponding RhB degradation performance under UV and visible light was investigated.[241] Enhanced photocatalytic activity was obtained for the ZGC due to the interaction between the graphene sheets and the ZnO nanoparticles. When compared with ZnO, ZGC exhibited efficient photosensitized electron injection and slow electron recombination. The application of ZGC has been extended to remove RhB dye molecules from water by using ZGC as filtration membranes, where the ZGC exhibited a higher efficiency than graphene and ZnO.[241]

4.6 Flame retardant polymer nanocomposites

Polymers are inherently flammable due to its organic nature. Reducing the flammability of polymers is essentially important in the fields of electronics, construction materials, vehicles and *etc.* Nanoclays seem to be a good option because heat release rate (HRR) and mass loss rate (MLR) can be tremendously reduced compared to neat polymers.[242–245] However, the main disadvantage of clay/polymer nanocomposites is that they do not extinguish and burn slowly until most of the fuel has been burnt. As a result, these materials by themselves are unable to meet the requirements of the ignition resistance tests

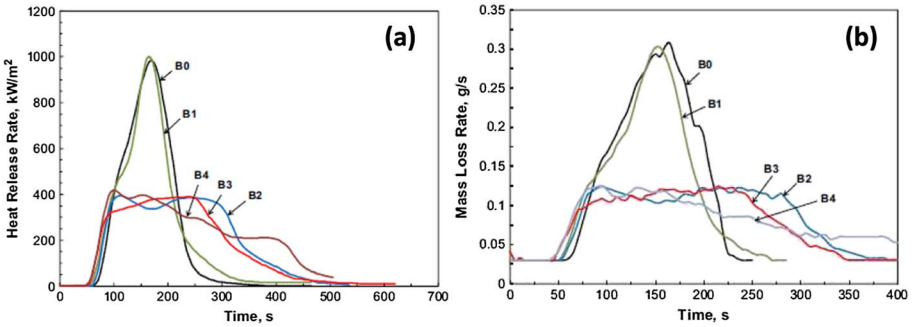

Fig. 41 Flammability properties of B0 and B1 to B4 evaluated with a cone calorimeter at an incident heat flux of 50 kW m^{-2}: (a) HRR and (b) MLR. B0: neat polyamide 6, B1: polyamide 6/POSS (85/15), B2: polyamide 6/organoclay (85/15), B3: polyamide 6/POSS/organoclay (70/15/15), and B4: polyamide 6/GO (85/15) nanocomposite.[257] Reproduced from ref. 257 with permission.

(*e.g.* vertical burning UL94 test). Besides, carbon based materials, such as carbon nanotubes[246–248] and fullerene,[249] were investigated to reduce the flammability of polymeric materials by inhibiting this vigorous bubbling process in the course of degradation during combustion. In recent years, GO and graphene as effective flame retardant fillers in polymers have been studied and the current progress in this area has been summarized and discussed.

Although high purity graphene is quite stable against combustion even in a natural gas flame, its thermal stability is significantly reduced when contaminated with potassium salt by-products left from GO synthesis, Fig. 40(a & b). In particular, the contaminated GO became highly flammable. A gentle touch with a hot soldering iron can trigger violent, catastrophic, total combustion of such GO films, which posed a serious fire hazard.[250] Recently, Zhang *et al.* reported a simple and efficient method to fabricate flexible multifunctional free-standing montmorillonite–RGO (MMT–RGO) hybrid films *via* vacuum filtration.[251] Aqueous colloidal dispersion of RGO, stabilized by MMT nanoplatelets with variable contents of RGO, has been obtained by direct reduction of GO in the presence of exfoliated MMT nanoplatelets. The MMT–RGO hybrid films show excellent flexibility, electrical conductivity and fire-retardant properties, Fig. 40(c & d).[251] Besides, surface modification on GO sheets with organics such as 2-amino-4,6-didodecylamino-1,3,5-triazine (ADDT) has been demonstrated as an effective approach to enhance the flame retardancy of GO.[252] The reduced MLR along with enhanced residue formation indicated a significant improvement in thermal stability for GO/ADDT compared to GO. Moreover, good solubility of GO/ADDT in organic solvents suggested the potential of GO/ADDT as a flame retardant nano-additive for polymeric systems.

GO with different oxidation states were examined as fire retardants of epoxy resin. It has been revealed that excessive oxidation was detrimental to the fire retardant effect of GO because it generated a weak GO with reduced intumescent ability.[254] Guo *et al.* prepared graphene, GO, and organic phosphate functionalized GO (FGO) from expandable graphite and incorporated into epoxy resin *via in situ* polymerization to prepare epoxy based composites.[102] The thermal behavior indicated the graphene/epoxy composites show the highest onset temperature and maximum weight loss temperature compared with those added with GO and FGO. The flame retardant properties investigated by micro combustion calorimeter illustrate that both graphene/epoxy and FGO/epoxy composites perform better than GO/epoxy composites in flame retardant properties with a maximum reduction of 23.7% in peak HRR when containing 5 wt% FGO and a maximum reduction of 43.9% at 5 wt% loading of graphene.[102] Liao *et al.* grafted 9,10-dihydro-9-oxa-10-phosphaphenanthrene-10-oxide (DOPO) onto GO sheets (DOPO–RGO) and integrated as filler in epoxy matrix.[255] The flame retardancy and thermal stability of DOPO–RGO/epoxy nanocomposites containing various weight fractions of DOPO–RGO were investigated by the limiting oxygen index (LOI) test and thermogravimetric analysis (TGA) in nitrogen. Significant increases in the char yield and LOI were achieved with the addition of 10 wt% DOPO–RGO in epoxy, giving improvements of 81 and 30%, respectively. DOPO–RGO/epoxy nanocomposites with phosphorus and graphene layer structures were found to contribute to excellent flame retardancy compared to that of neat epoxy. Therefore, the synergistic effect of DOPO–RGO is quite useful, and this material can be utilized as a potential flame retardant. Most recently, Wang *et al.* introduced Ni–Fe layered double hydroxide/graphene hybrids into epoxy to reduce fire hazard in epoxy composites.[256] With the incorporation of 2.0 wt% of Ni–Fe LDH/graphene, the onset thermal degradation temperature of the epoxy composites was significantly increased by 25 °C compared to that of pure epoxy. Also, the addition of Ni–Fe LDH/graphene hybrids imparted excellent flame retardant properties, evidenced by the dramatically reduced peak HRR and total heat release values obtained from micro combustion calorimeter and cone calorimeter.

Dasari *et al.* comparatively studied the roles of GO, clay and polyhedral oligomeric silsesquioxane (POSS) during the combustion of polyamide 6.[257] The HRR and MLR of composites with different composition were shown in Fig. 41. No improvements were observed with additional incorporation of POSS in the organoclay/polyamide 6 nanocomposite. The voluminous expansion of GO during combustion of GO/polyamide 6 composite combined with the physical barrier mechanism contributed to the significant reductions of HRR (~60%

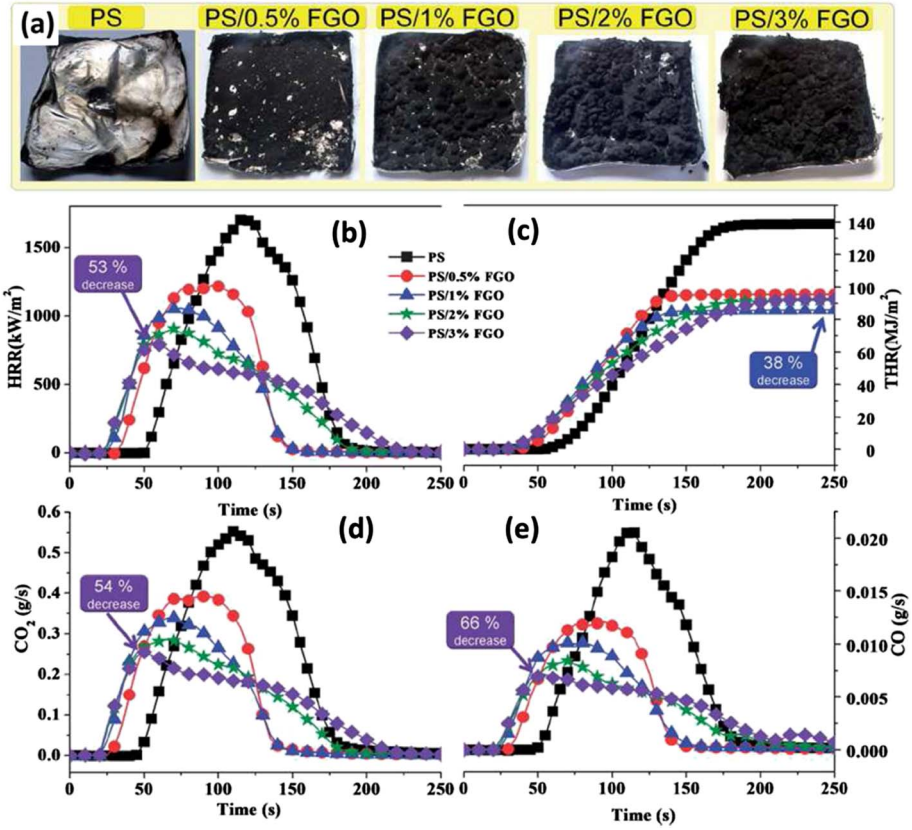

Fig. 42 (a) Digital photographs of char, and Cone calorimeter test results of (b) HRR curves, (c) THR curves, (d) CO_2 yield; and (e) CO yield.[264] Reproduced from ref. 264 with permission.

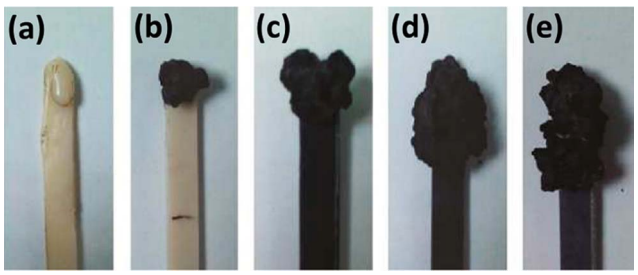

Fig. 43 Photos of char residues of samples after combustion: (a) PBS, (b) PBS-1 (PBS/IFR/GNS = 80/20/0), (c) PBS-2 (PBS/IFR/GNS = 80/19.5/0.5), (d) PBS-3 (PBS/IFR/GNS = 80/19/1), and (e) PBS-4 (PBS/IFR/GNS = 80/18/2).[265] Reproduced from ref. 265 with permission.

compared to neat polyamide 6) and MLR, and delayed the burning even slightly better than the organoclay nanocomposites.

Graphene has been demonstrated as effective flame retardant filler in PVA as well. Graphene/PVA nanocomposites prepared from solution blending method showed excellent flame retardant behavior with a significant reduction in peak HRR (49% reduction with 3 wt% graphene) and a much longer time to ignition.[258] The coexistence of melamine polyphosphate (MPP) and graphene in PVA lead to an even more significantly reduced flammability for the nanocomposites. PVA composites filled with 10 wt% MPP and 1 wt% graphene (PVA/G1/MPP10) achieved the LOI value of 29.6 and UL-94 V0 grade. Compared to pure PVA, the peak HRR of PVA/G1/MPP10 was reduced by about 60%.[259]

Cao *et al.* grafted polypropylene on GO sheets (PP-*g*-GO) to improve the compatibility of immiscible PP/polyphenylene oxide (PP/PPO, 90/10) blends.[260] With 0.5 wt% of PP-*g*-GO into immiscible PP/PPO blends, the dispersion of the minor phase (PPO) was remarkably improved without visible agglomerates. Moreover, PP-*g*-GO acted as effective fillers for enhancing the flame retardancy of PP/PPO blends. GO and graphene has been also demonstrated effective flame retardant fillers in poly(piperazine spirocyclic pentaerythritol bisphosphonate) (PPSPB),[261] polycarbonate (PC), acrylonitrile butadiene styrene (ABS), high-impact PS,[262] and polyurethane acrylate (PUA).[263]

A novel strategy based on functionalized GO was developed to overcome the challenge of graphene in its burn out limits.[264] GO was functionalized with char-catalyzing agents and reactive compounds and incorporated into PS. When FGO/PS composites were degraded or burned, FGO catalyzed the char formation from polystyrene (Char A). Char A protected FGO from burning out and then FGO acted as a graphitic char (Char B). Because of the combination of Char A, Char B, the physical barrier effects of FGO, and the strong interfacial interactions of FGO and polymers, the fire safety properties of the FGO–polystyrene composites were improved, including increased char formation

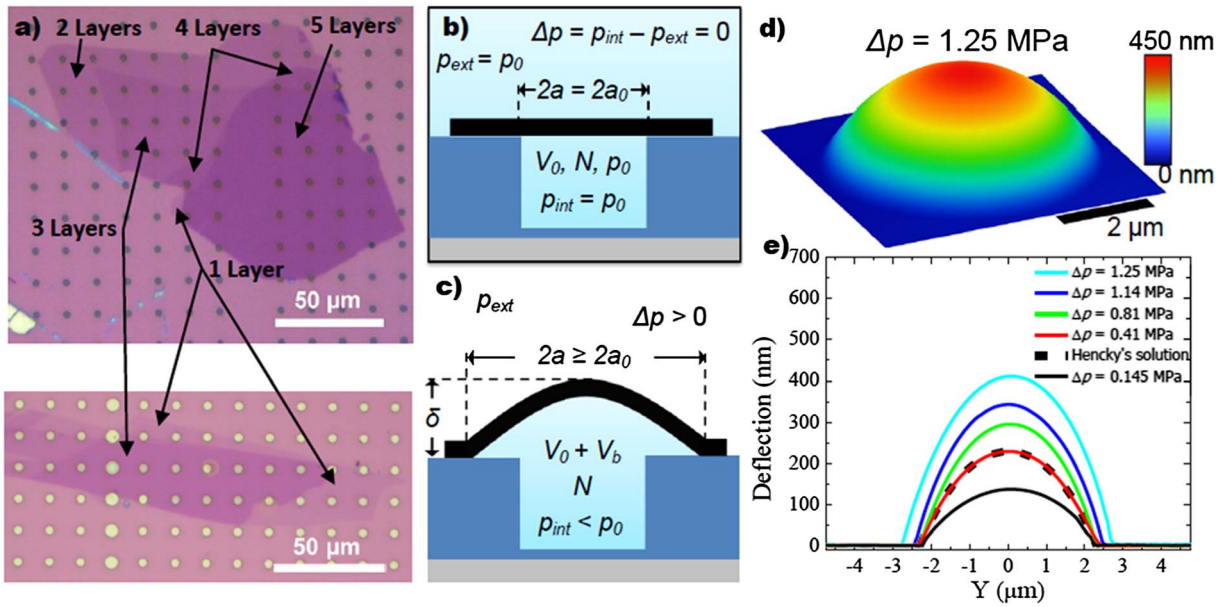

Fig. 44 Pressurizing graphene membranes (a) two optical images showing graphene flakes with regions of 2–5 suspended layers (top) and 1 and 3 suspended layers (bottom). The arrays of microcavities in the SiO_2 substrate can also be seen. (b) Schematic illustration of a graphene-sealed microcavity before it is placed in the pressure chamber. The pressure inside the microcavity p_{int} is equal to the external pressure p_{ext}, so the membrane is flat. After 4–6 days inside the pressure chamber, p_{int} increases to p_0. (c) When the microcavity is removed from the pressure chamber, the pressure difference across the membrane causes it to bulge upward and eventually delaminate from the substrate, causing the radius a to increase. (d) Three dimensional rendering of an AFM image showing the deformed shape of a monolayer graphene membrane with $\Delta p = p_{int} - p_{ext} = 1.25$ MPa. (e) Deflection *versus* position as Δp is increased from 0.145 MPa (black) to 1.25 MPa (cyan). The dashed black line is the shape obtained from Hencky's solution for $\Delta p = 0.41$ MPa. The deflection is measured by an AFM along a line that passes through the centre of the membrane.[269] Reproduced from ref. 269 with permission.

(7 times), Fig. 42(a), decreased peak CO release rate (66% decrease), decreased peak CO_2 release rate (54% decrease), decreased peak HRR (53% decrease), decreased thermal degradation rate (30% decrease), and decreased total heat release (THR) (38% decrease), Fig. 42(b–e).[264]

Flame retardant poly(butylene succinate) (IFRPBS) composites with enhanced fire resistance were prepared using graphene as synergist.[265,266] The LOI values increased from 23.0 for pure PBS to 31.0 for IFRPBS with 20 wt% IFR loading.[265] The addition of graphene further improved the LOI values of the composites and exhibited excellent antidripping properties, Fig. 43. The UL-94 V0 materials were obtained with a formulation of 18 wt% IFR and 2 wt% graphene. Melt flow index (MFI) measurement indicated that the presence of graphene significantly enhanced the melt viscosity and restrained the melt dripping.[265]

4.7 Graphene membrane

Membranes are widely existed as an essential component in a variety of physical, chemical, and biological systems, used in everything from cellular compartmentalization to mechanical pressure sensing. Graphene, a single layer of graphite, is the thinnest membrane (one atom in thickness) that still acquires highly electrical conductivity and excellent chemical inertness. Recently, researchers started theoretical and experimental investigation in graphene membrane, including adhesion of graphene membrane to a substrate, gas and liquid separation behaviors in porous graphene membranes, and DNA translocation through graphene pores.

Van der walls force plays a significant role in mechanical properties when the mechanical structures enters nanoscale

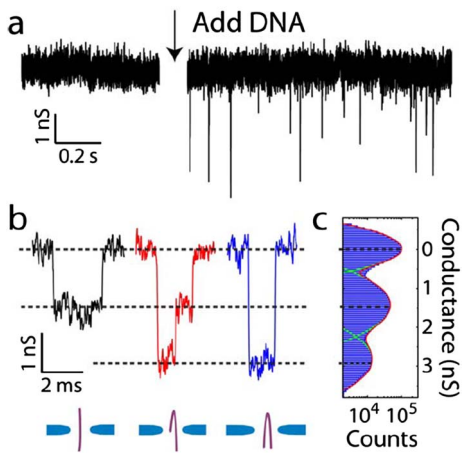

Fig. 45 DNA translocation through a graphene monolayer. (a) Translocation of 48 kbp double-stranded λ-DNA across a 22 nm nanopore within a graphene monolayer, showing the baseline conductance (left) and blockade events upon addition of DNA (right). (b) Examples of translocation events of nonfolded (black), partially folded (red) and fully folded (blue) DNA molecules recorded at 200 mV. (c) Conductance histogram of 1222 translocation events, including 1 ms of open-pore conductance before and after the event. Note that counts in this histogram correspond to a single current measurement, not to a single event.[277] Reproduced from ref. 277 with permission.

region.[267,268] This force clamps graphene samples to substrates, and also holds together the individual graphene sheets in multilayer samples. Koenig *et al.*[269] used a pressurized blister test to directly measure the adhesion energy of graphene sheets with a silicon oxide substrate (Fig. 44) and found that an adhesion energy of 0.45 ± 0.02 J m^{-2} for monolayer graphene and 0.31 ± 0.03 J m^{-2} for samples containing 2–5 graphene sheets. These values are larger than the adhesion energies measured in typical micromechanical structures and are comparable to solid/liquid adhesion energies. Lu *et al.*[270] developed an atomic simulation model to describe single layers of graphene adhered to a substrate, which showed excellent agreement with theory and identified the influence of van der Walls adhesion energy on membrane decohesion from and/or sliding along a substrate.

Single layer graphene has been demonstrated to be impermeable to standard gases including helium.[267] With this advantage, single layer graphene has been developed into a trans-electrode membrane utilizing the atomic scale opposing liquid–solid interfaces together with graphene's well known in-plane conductivity.[271] Although the membranes were only one to two atomic layers thick, it is found that they were remarkable ionic insulators with a very small stable conductance that depended on the ion species in solution. Electrical measurements on graphene membranes in which a single nanopore has been drilled showed that the membrane's effective insulating thickness was less than one nanometer. This small effective thickness made graphene an ideal substrate for very high-resolution, high throughput nanopore-based single molecule detectors.[271] Even though graphene is not permeable, porous graphene with intentionally introduced pore structure could be a good candidate for separation applications. Until now, most of the literature reports were based on theoretical simulation while experimental work was rarely reported. For example, Blankenburg *et al.*[272] developed a graphene porous network through self-assembling of hexaiodo-substituted macrocycle cyclohexa-*m*-phenylene using first principle calculations. The resulting porous network exhibited an extremely high selectivity in favor of H_2 and He among other atmospheric gases, such as Ne, O_2, N_2, CO, CO_2, NH_3, and Ar. He separation from He/Ne/CH_4 was also performed using porous graphene membrane.[273] Jiang *et al.*[274] investigated the permeability and selectivity of graphene sheets with designed sub-nanometer pores using first principles density functional theory calculations. High selectivity on the order of 10^8 for H_2/CH_4 with a high H_2 permeance for a nitrogen-functionalized pore and has been revealed. Meanwhile, they found extremely high selectivity on the order of 10^{23} for H_2/CH_4 for an all-hydrogen passivated pore whose small width (at 2.5 Å) presents a formidable barrier (1.6 eV) for CH_4 but easily surmountable for H_2 (0.22 eV). Nanopore size and shape of porous graphene membrane have been studied in H_2/N_2 separation.[275] Small pore only allowed hydrogen molecules to permeate due to the size restriction. When the pore size was big enough to allow nitrogen molecules to permeate without any restriction, more permeation of nitrogen than that of hydrogen molecules was observed. When the pore size further increased, the flow of hydrogen molecules exhibited linear dependence on the pore area, while no obvious correlation between nitrogen molecules and the pore area. Liquid separation (benzene, water and acetonitrile) by a graphene membrane was also realized *via* extensive molecular dynamics simulations.[276]

Recently, an experimental approach demonstrated that it is possible to realize and use ultrathin nanopores fabricated in graphene monolayers for single-molecule DNA translocation.[277] The pores were obtained by placing a graphene flake over a microsize hole in a silicon nitride membrane and drilling a nanosize hole in the graphene using an electron beam. As individual DNA molecules translocated through the pore, characteristic temporary conductance changes were observed in the ionic current through the nanopore, setting the stage for future genomic screening, Fig. 45.

5. Conclusions and perspectives

This review summarizes not only the recent progress of graphene applications in research areas including electrochemical energy storage, thermal energy and solar energy conversion, electrochemical and biological sensing, polluted water treatment, but also the newly developed research areas such as flame retardant graphene composites, graphene single layer membrane for chemical and biomolecule separation. Obviously, the superior material performance in versatile applications are taking advantage of the outstanding physiochemical properties of graphene that include excellent electrical conductivity, large specific surface area, high mechanical strength, low manufacturing cost and *etc.* In current research, both graphene and graphene composites are designed to overcome the limitations and achieve revolutionary performances with regard to specific applications. To realize multi-functionalities in a single material as required by certain applications, graphene nanocomposites decorated with functional groups or nanostructures are well accepted as the major strategy. However, the major challenge of the hybrid composite synthesis comes from the different functional groups that exist at the edge area and basal planes of graphene. When the graphene surface is exposed for nanostructure growth, a selective reaction between specific surface groups and nanomaterial precursors would occur and result in a non-uniform distribution. A convenient technique to engineer the graphene surface for chemically homogeneous functions is in great demand. The other challenge is the interfacial interaction that bridges the functionalities of individual components together. Until now, successful combination of graphene and other nanomaterials with tremendously improved physiochemical properties have been reported from the significant amount of recent literatures. However, only few work has mentioned how the nanostructures are bonded to the graphene surface and effective characterization techniques are still in demand. The relationship between the interfacial bonding mode and final nanocomposite performance needs to be elucidated.

To further explore the potential of graphene in improving solar cell energy conversion efficiency, large scale, continuous,

highly transparent, conductive and atomic level thickness graphene film fabrication is the key technique where significant research efforts need get involved to develop cost-effective and highly efficient graphite layer exfoliation technique in the future. Development in organic synthesis of graphene together with the well developed chemical vapor deposition technique provides a possible approach to manufacture the above mentioned graphene film, while their strict operation conditions and high manufacturing cost make them difficult to realize scale-up production. The demonstrated sensitivity of graphene and GNCs electrodes in detecting explosive chemicals at ppb level as well as the bio-molecules at a similar sensing level provides a platform for other sensing applications in the future including bacterial culturing, virus monitoring, disease control and *etc.* However, sensitivity and selectivity are equally important for reliable sensing devices. In real sample, interference between co-existing molecules often occurs to disturb the real sensing signal. Tremendous fundamental research need gets involved in this area to design novel graphene nanocomposites at molecular level and achieve specified sensing capability to targeting molecules. Cost effective and environmental benign synthetic methods will be the two major considerations in developing efficient adsorbents and photocatalysts for water purification. There is also a trend that multifunctionalities will be integrated into one material, which is able to adsorb heavy metal ions, degrade organic dyes and even kill the bacterial at the same time from a single step process. Even though the mechanical reinforcement of graphene in polymer nanocomposites has not been detailed in this review, the incorporation of graphene into polymer is an efficient approach to broaden the function and enhance the performance of polymer. However, efficient methods for single layer dispersion of graphene in these hybrids are very limited because graphene is very easily aggregated due to their π–π interaction. Effective interfacial engineering techniques (chemical modification, plasmon treatment and *etc.*) and processing techniques are still desired for manufacturing high performance polymer nanocomposites. Gas, liquid and even biomolecule separation based on single-layer/multi-layers graphene membrane is an ideal model right now and the related researches are mostly at the simulation stage. Experimentalists need involve their efforts to design a separation device that is equipped with atomic thickness graphene membrane and verify the interesting phenomena that have been proposed by the theoretical scientists. This article reviews the applications of graphene and GNCs in a multidisciplinary environment. However, there are still many unexplored aspects yet to be investigated in the future.

Acknowledgements

The authors appreciate the support from Research Enhancement Grant (REG) of Lamar University. Partial financial supports from NSF-Nanomanufacturing (CMMI-13-14486), Nanoscale Interdisciplinary Research Team and Materials Processing and Manufacturing (CMMI 10-30755) and Chemical and Biological Separations (CBET 11-37441) are acknowledged. Dr Shao acknowledges the financial supports from NSFC (21177032) and Program for New Century Excellent Talents in University (NCET-11-0805). The Welch Foundation (V-0004) is also acknowledged.

References

1 K. S. Novoselov, D. Jiang, F. Schedin, T. J. Booth, V. V. Khotkevich, S. V. Morozov and A. K. Geim, *Proc. Natl. Acad. Sci. U. S. A.*, 2005, **102**, 10451–10453.
2 Y. Zhang, Y.-W. Tan, H. L. Stormer and P. Kim, *Nature*, 2005, **438**, 201–204.
3 D. A. Abanin, S. V. Morozov, L. A. Ponomarenko, R. V. Gorbachev, A. S. Mayorov, M. I. Katsnelson, K. Watanabe, T. Taniguchi, K. S. Novoselov, L. S. Levitov and A. K. Geim, *Science*, 2011, **332**, 328–330.
4 J. H. Seol, I. Jo, A. L. Moore, L. Lindsay, Z. H. Aitken, M. T. Pettes, X. Li, Z. Yao, R. Huang, D. Broido, N. Mingo, R. S. Ruoff and L. Shi, *Science*, 2010, **328**, 213–216.
5 A. K. Geim and K. S. Novoselov, *Nat. Mater.*, 2007, **6**, 183–191.
6 C. N. R. Rao, K. Biswas, K. S. Subrahmanyam and A. Govindaraj, *J. Mater. Chem.*, 2009, **19**, 2457–2469.
7 K. S. Novoselov, A. K. Geim, S. V. Morozov, D. Jiang, Y. Zhang, S. V. Dubonos, I. V. Grigorieva and A. A. Firsov, *Science*, 2004, **306**, 666–669.
8 J. C. Meyer, A. K. Geim, M. I. Katsnelson, K. S. Novoselov, T. J. Booth and S. Roth, *Nature*, 2007, **446**, 60–63.
9 I. K. Moon, J. Lee, R. S. Ruoff and H. Lee, *Nat. Commun.*, 2010, **1**, 73.
10 S. Stankovich, D. A. Dikin, R. D. Piner, K. A. Kohlhaas, A. Kleinhammes, Y. Jia, Y. Wu, S. T. Nguyen and R. S. Ruoff, *Carbon*, 2007, **45**, 1558–1565.
11 X. Yang, X. Dou, A. Rouhanipour, L. Zhi, H. J. Räder and K. Müllen, *J. Am. Chem. Soc.*, 2008, **130**, 4216–4217.
12 L. Gomez De Arco, Y. Zhang, C. W. Schlenker, K. Ryu, M. E. Thompson and C. Zhou, *ACS Nano*, 2010, **4**, 2865–2873.
13 G. Goncalves, P. A. A. P. Marques, A. Barros-Timmons, I. Bdkin, M. K. Singh, N. Emami and J. Gracio, *J. Mater. Chem.*, 2010, **20**, 9927–9934.
14 X. Zhao, Q. Zhang, D. Chen and P. Lu, *Macromolecules*, 2010, **43**, 2357–2363.
15 M. A. Rafiee, J. Rafiee, Z. Wang, H. Song, Z.-Z. Yu and N. Koratkar, *ACS Nano*, 2009, **3**, 3884–3890.
16 Z. Xu and C. Gao, *Macromolecules*, 2010, **43**, 6716–6723.
17 J. Zhu, S. Wei, H. Gu, S. B. Rapole, Q. Wang, Z. Luo, N. Haldolaarachchige, D. P. Young and Z. Guo, *Environ. Sci. Technol.*, 2012, **46**, 977–985.
18 V. Chandra, J. Park, Y. Chun, J. W. Lee, I.-C. Hwang and K. S. Kim, *ACS Nano*, 2010, **4**, 3979–3986.
19 J. Zhu, R. Sadu, S. Wei, D. H. Chen, N. Haldolaarachchige, Z. Luo, J. A. Gomes, D. P. Young and Z. Guo, *ECS J. Solid State Sci. Technol.*, 2012, **1**, M1–M5.
20 V. Chandra and K. S. Kim, *Chem. Commun.*, 2011, **47**, 3942–3944.

21 Y. Liang, H. Wang, H. Sanchez Casalongue, Z. Chen and H. Dai, *Nano Res.*, 2010, **3**, 701–705.
22 Z.-S. Wu, D.-W. Wang, W. Ren, J. Zhao, G. Zhou, F. Li and H.-M. Cheng, *Adv. Funct. Mater.*, 2010, **20**, 3595–3602.
23 J. Zhang, J. Jiang, H. Li and X. S. Zhao, *Energy Environ. Sci.*, 2011, **4**, 4009–4015.
24 H. Huang and X. Wang, *Nanoscale*, 2011, **3**, 3185–3191.
25 R. B. Rakhi, W. Chen, D. Cha and H. N. Alshareef, *J. Mater. Chem.*, 2011, **21**, 16197–16204.
26 G. Yu, L. Hu, M. Vosgueritchian, H. Wang, X. Xie, J. R. McDonough, X. Cui, Y. Cui and Z. Bao, *Nano Lett.*, 2011, **11**, 2905–2911.
27 H. Kim, D.-H. Seo, S.-W. Kim, J. Kim and K. Kang, *Carbon*, 2011, **49**, 326–332.
28 Z.-S. Wu, W. Ren, L. Wen, L. Gao, J. Zhao, Z. Chen, G. Zhou, F. Li and H.-M. Cheng, *ACS Nano*, 2010, **4**, 3187–3194.
29 X. Xia, J. Tu, Y. Mai, R. Chen, X. Wang, C. Gu and X. Zhao, *Chem.–Eur. J.*, 2011, **17**, 10898–10905.
30 Y. Bu, S. Wang, H. Jin, W. Zhang, J. Lin and J. Wang, *J. Electrochem. Soc.*, 2012, **159**, A990–A995.
31 S. D. Perera, A. D. Liyanage, N. Nijem, J. P. Ferraris, Y. J. Chabal and K. J. Balkus Jr, *J. Power Sources*, 2012, **230**, 130–137.
32 H.-W. Wang, Z.-A. Hu, Y.-Q. Chang, Y.-L. Chen, H.-Y. Wu, Z.-Y. Zhang and Y.-Y. Yang, *J. Mater. Chem.*, 2011, **21**, 10504–10511.
33 J. Xu, K. Wang, S.-Z. Zu, B.-H. Han and Z. Wei, *ACS Nano*, 2010, **4**, 5019–5026.
34 K. Zhang, L. L. Zhang, X. S. Zhao and J. Wu, *Chem. Mater.*, 2010, **22**, 1392–1401.
35 J. Zhu, M. Chen, H. Qu, X. Zhang, H. Wei, Z. Luo, H. A. Colorado, S. Wei and Z. Guo, *Polymer*, 2012, **53**, 5953–5964.
36 S. Biswas and L. T. Drzal, *Chem. Mater.*, 2010, **22**, 5667–5671.
37 D. Zhang, X. Zhang, Y. Chen, P. Yu, C. Wang and Y. Ma, *J. Power Sources*, 2011, **196**, 5990–5996.
38 L. L. Zhang, S. Zhao, X. N. Tian and X. S. Zhao, *Langmuir*, 2010, **26**, 17624–17628.
39 F. Alvi, M. K. Ram, P. A. Basnayaka, E. Stefanakos, Y. Goswami and A. Kumar, *Electrochim. Acta*, 2011, **56**, 9406–9412.
40 D. K. James and J. M. Tour, *Macromol. Chem. Phys.*, 2012, **213**, 1033–1050.
41 M. J. Allen, V. C. Tung and R. B. Kaner, *Chem. Rev.*, 2009, **110**, 132–145.
42 Y. Zhu, S. Murali, W. Cai, X. Li, J. W. Suk, J. R. Potts and R. S. Ruoff, *Adv. Mater.*, 2010, **22**, 3906–3924.
43 M. J. McAllister, J.-L. Li, D. H. Adamson, H. C. Schniepp, A. A. Abdala, J. Liu, M. Herrera-Alonso, D. L. Milius, R. Car, R. K. Prud'homme and I. A. Aksay, *Chem. Mater.*, 2007, **19**, 4396–4404.
44 H. C. Schniepp, J.-L. Li, M. J. McAllister, H. Sai, M. Herrera-Alonso, D. H. Adamson, R. K. Prud'homme, R. Car, D. A. Saville and I. A. Aksay, *J. Phys. Chem. B*, 2006, **110**, 8535–8539.
45 R. S. Sundaram, C. Gómez-Navarro, K. Balasubramanian, M. Burghard and K. Kern, *Adv. Mater.*, 2008, **20**, 3050–3053.
46 M. Zhou, Y. Wang, Y. Zhai, J. Zhai, W. Ren, F. Wang and S. Dong, *Chem.–Eur. J.*, 2009, **15**, 6116–6120.
47 H. He, J. Klinowski, M. Forster and A. Lerf, *Chem. Phys. Lett.*, 1998, **287**, 53–56.
48 M. S. Dresselhaus, A. Jorio, M. Hofmann, G. Dresselhaus and R. Saito, *Nano Lett.*, 2010, **10**, 751–758.
49 X. Li, G. Zhang, X. Bai, X. Sun, X. Wang, E. Wang and H. Dai, *Nat. Nanotechnol.*, 2008, **3**, 538–542.
50 M. Lotya, Y. Hernandez, P. J. King, R. J. Smith, V. Nicolosi, L. S. Karlsson, F. M. Blighe, S. De, Z. Wang, I. T. McGovern, G. S. Duesberg and J. N. Coleman, *J. Am. Chem. Soc.*, 2009, **131**, 3611–3620.
51 A. C. Ferrari, *Solid State Commun.*, 2007, **143**, 47–57.
52 J. Lu, J.-x. Yang, J. Wang, A. Lim, S. Wang and K. P. Loh, *ACS Nano*, 2009, **3**, 2367–2375.
53 M. Zhou, Y. Zhai and S. Dong, *Anal. Chem.*, 2009, **81**, 5603–5613.
54 N. G. Shang, P. Papakonstantinou, M. McMullan, M. Chu, A. Stamboulis, A. Potenza, S. S. Dhesi and H. Marchetto, *Adv. Funct. Mater.*, 2008, **18**, 3506–3514.
55 D. A. C. Brownson and C. E. Banks, *Analyst*, 2010, **135**, 2768–2778.
56 L. Tang, Y. Wang, Y. Li, H. Feng, J. Lu and J. Li, *Adv. Funct. Mater.*, 2009, **19**, 2782–2789.
57 P. Recher and B. Trauzettel, *Physics*, 2011, **4**, 25.
58 E. H. Hwang and S. Das Sarma, *Phys. Rev. B: Condens. Matter Mater. Phys.*, 2007, **75**, 205418.
59 M. Jablan, H. Buljan and M. Soljaccaronicacute, *Phys. Rev. B: Condens. Matter Mater. Phys.*, 2009, **80**, 245435.
60 M. I. Katsnelson, K. S. Novoselov and A. K. Geim, *Nat. Phys.*, 2006, **2**, 620–625.
61 J. Zhu, S. Wei, N. Haldolaarachchige, J. He, D. P. Young and Z. Guo, *Nanoscale*, 2012, **4**, 152–156.
62 L. Yang, J. Deslippe, C.-H. Park, M. L. Cohen and S. G. Louie, *Phys. Rev. Lett.*, 2009, **103**, 186802.
63 R. R. Nair, P. Blake, A. N. Grigorenko, K. S. Novoselov, T. J. Booth, T. Stauber, N. M. R. Peres and A. K. Geim, *Science*, 2008, **320**, 1308.
64 G. Eda, G. Fanchini and M. Chhowalla, *Nat. Nanotechnol.*, 2008, **3**, 270–274.
65 X. Li, Y. Zhu, W. Cai, M. Borysiak, B. Han, D. Chen, R. D. Piner, L. Colombo and R. S. Ruoff, *Nano Lett.*, 2009, **9**, 4359–4363.
66 X. Wang, L. Zhi and K. Mullen, *Nano Lett.*, 2007, **8**, 323–327.
67 H. A. Becerril, J. Mao, Z. Liu, R. M. Stoltenberg, Z. Bao and Y. Chen, *ACS Nano*, 2008, **2**, 463–470.
68 K. P. Loh, Q. Bao, G. Eda and M. Chhowalla, *Nat. Chem.*, 2010, **2**, 1015–1024.
69 X. Sun, Z. Liu, K. Welsher, J. Robinson, A. Goodwin, S. Zaric and H. Dai, *Nano Res.*, 2008, **1**, 203–212.
70 Z. Luo, P. Vora, E. J. Mele, A. T. C. Johnson and J. M. Kikkawa, *Appl. Phys. Lett.*, 2009, **94**, 111909.
71 J. Zang and X. Li, *J. Mater. Chem.*, 2011, **21**, 10965–10969.

72 A. K. Mishra and S. Ramaprabhu, *J. Phys. Chem. C*, 2011, **115**, 14006–14013.
73 M. D. Archer, *Sol. Energy*, 1978, **20**, 167–169.
74 H.-D. Scharf, J. Fleischhauer, H. Leismann, I. Ressler, W.-g. Schleker and R. Weitz, *Angew. Chem., Int. Ed.*, 1979, **18**, 652–662.
75 J. P. Heremans, C. M. Thrush, D. T. Morelli and M.-C. Wu, *Phys. Rev. Lett.*, 2002, **88**, 216801.
76 H. Zhang, X. Lv, Y. Li, Y. Wang and J. Li, *ACS Nano*, 2009, **4**, 380–386.
77 F. Rahman, K. H. Langford, M. D. Scrimshaw and J. N. Lester, *Sci. Total Environ.*, 2001, **275**, 1–17.
78 S. H. Chiu and W. K. Wang, *J. Appl. Polym. Sci.*, 1998, **67**, 989–995.
79 X. Chen, J. Yu, S. Guo, S. Lu, Z. Luo and M. He, *J. Mater. Sci.*, 2009, **44**, 1324–1332.
80 K. Wu, L. Song, Z. Wang and Y. Hu, *J. Polym. Res.*, 2009, **16**, 283–294.
81 J.-K. Yang, H.-J. Park, H.-D. Lee and S.-M. Lee, *Colloids Surf., A*, 2009, **337**, 154–158.
82 X. Zhang, Q. He, H. Gu, H. A. Colorado, S. Wei and Z. Guo, *ACS Appl. Mater. Interfaces*, 2012, **5**, 898–910.
83 H. Horacek and R. Grabner, *Polym. Degrad. Stab.*, 1996, **54**, 205–215.
84 T. Kashiwagi, F. Du, K. I. Winey, K. M. Groth, J. R. Shields, S. P. Bellayer, H. Kim and J. F. Douglas, *Polymer*, 2005, **46**, 471–481.
85 T. Kashiwagi, E. Grulke, J. Hilding, K. Groth, R. Harris, K. Butler, J. Shields, S. Kharchenko and J. Douglas, *Polymer*, 2004, **45**, 4227–4239.
86 T. Kashiwagi, E. Grulke, J. Hilding, R. Harris, W. Awad and J. Douglas, *Macromol. Rapid Commun.*, 2002, **23**, 761–765.
87 P. Song, L. Xu, Z. Guo, Y. Zhang and Z. Fang, *J. Mater. Chem.*, 2008, **18**, 5083–5091.
88 P. a. Song, L. Xu, Z. Guo, Y. Zhang and Z. Fang, *J. Mater. Chem.*, 2008, **18**, 5083–5091.
89 H. Lu, Y. Hu, J. Xiao, Z. Wang, Z. Chen and W. Fan, *J. Mater. Sci.*, 2006, **41**, 363–367.
90 Y. Tang, Y. Hu, B. Li, L. Liu, Z. Wang, Z. Chen and W. Fan, *J. Polym. Sci., Part A: Polym. Chem.*, 2004, **42**, 6163–6173.
91 Y. Tang, Y. Hu, S. Wang, Z. Gui, Z. Chen and W. Fan, *Polym. Int.*, 2003, **52**, 1396–1400.
92 Q. Wang and D. O'Hare, *Chem. Rev.*, 2012, **112**, 4124–4155.
93 Q. Wang, X. Zhang, C. J. Wang, J. Zhu, Z. Guo and D. O'Hare, *J. Mater. Chem.*, 2012, **22**, 19113–19121.
94 Q. Wang, X. Zhang, J. Zhu, Z. Guo and D. O'Hare, *Chem. Commun.*, 2012, **48**, 7450–7452.
95 Q. He, H. Lu, L. Song, Y. Hu and L. Chen, *J. Fire Sci.*, 2009, **27**, 303–321.
96 P. Zhang, L. Song, H. Lu, Y. Hu, W. Xing, J. Ni and J. Wang, *Polym. Degrad. Stab.*, 2009, **94**, 201–207.
97 S.-Y. Lu and I. Hamerton, *Prog. Polym. Sci.*, 2002, **27**, 1661–1712.
98 H. Yang, C. Q. Yang and Q. He, *Polym. Degrad. Stab.*, 2009, **94**, 1023–1031.
99 S. Nie, Y. Hu, L. Song, Q. He, D. Yang and H. Chen, *Polym. Adv. Technol.*, 2008, **19**, 1077–1083.
100 W. Zhang, X. Li, X. Guo and R. Yang, *Polym. Degrad. Stab.*, 2010, **95**, 2541–2546.
101 X. Wang, L. Song, H. Yang, W. Xing, H. Lu and Y. Hu, *J. Mater. Chem.*, 2012, **22**, 3426–3431.
102 Y. Guo, C. Bao, L. Song, B. Yuan and Y. Hu, *Ind. Eng. Chem. Res.*, 2011, **50**, 7772–7783.
103 L. O. Index, Standard Test Method for Measuring Minimum Oxygen Concentration to Support Candle-Like Combustion of Plastics, *ASTM D 2863*, 2008, 2863.
104 Standard Test Method for Measuring the Comparative Burning Characteristics of Solid Plastics in a Vertical Position, UL-94, *ASTM D*, ASTM International, 2010, vol. 3801.
105 V. Babrauskas and R. D. Peacock, *Fire Saf. J.*, 1992, **18**, 255–272.
106 C. Q. Yang, Q. He, R. E. Lyon and Y. Hu, *Polym. Degrad. Stab.*, 2010, **95**, 108–115.
107 Standard Test Method for Heat and Visible Smoke Release Rates for Materials and Products Using an Oxygen Consumption Calorimeter, *ASTM E1354-13*, 2013.
108 M. C. Calorimetry, Standard Test Method for Determining Flammability Characteristics of Plastics and Other Solid Materials Using Microscale Combustion Calorimetry, *ASTM International*, 2011, vol. 7309.
109 S. Pei and H.-M. Cheng, *Carbon*, 2012, **50**, 3210–3228.
110 M. D. Stoller, S. Park, Y. Zhu, J. An and R. S. Ruoff, *Nano Lett.*, 2008, **8**, 3498–3502.
111 M. D. Stoller, C. W. Magnuson, Y. Zhu, S. Murali, J. W. Suk, R. Piner and R. S. Ruoff, *Energy Environ. Sci.*, 2011, **4**, 4685–4689.
112 H. Gwon, H.-S. Kim, K. U. Lee, D.-H. Seo, Y. C. Park, Y.-S. Lee, B. T. Ahn and K. Kang, *Energy Environ. Sci.*, 2011, **4**, 1277–1283.
113 J. Xia, F. Chen, J. Li and N. Tao, *Nat. Nanotechnol.*, 2009, **4**, 505–509.
114 C. Liu, Z. Yu, D. Neff, A. Zhamu and B. Z. Jang, *Nano Lett.*, 2010, **10**, 4863–4868.
115 Y. Wang, Z. Shi, Y. Huang, Y. Ma, C. Wang, M. Chen and Y. Chen, *J. Phys. Chem. C*, 2009, **113**, 13103–13107.
116 D. A. C. Brownson and C. E. Banks, *Chem. Commun.*, 2012, **48**, 1425–1427.
117 B. G. Choi, J. Hong, W. H. Hong, P. T. Hammond and H. Park, *ACS Nano*, 2011, **5**, 7205–7213.
118 X. Li, T. Zhao, K. Wang, Y. Yang, J. Wei, F. Kang, D. Wu and H. Zhu, *Langmuir*, 2011, **27**, 12164–12171.
119 L. Zhang and G. Shi, *J. Phys. Chem. C*, 2011, **115**, 17206–17212.
120 D. Yu and L. Dai, *J. Phys. Chem. Lett.*, 2009, **1**, 467–470.
121 X. Lu, H. Dou, B. Gao, C. Yuan, S. Yang, L. Hao, L. Shen and X. Zhang, *Electrochim. Acta*, 2011, **56**, 5115–5121.
122 S.-Y. Yang, K.-H. Chang, H.-W. Tien, Y.-F. Lee, S.-M. Li, Y.-S. Wang, J.-Y. Wang, C.-C. M. Ma and C.-C. Hu, *J. Mater. Chem.*, 2011, **21**, 2374–2380.
123 Z. Fan, J. Yan, L. Zhi, Q. Zhang, T. Wei, J. Feng, M. Zhang, W. Qian and F. Wei, *Adv. Mater.*, 2010, **22**, 3723–3728.

124 J. Lin, C. Zhang, Z. Yan, Y. Zhu, Z. Peng, R. H. Hauge, D. Natelson and J. M. Tour, *Nano Lett.*, 2013, **13**, 72–78.
125 D. Wei, S. J. Wakeham, T. W. Ng, M. J. Thwaites, H. Brown and P. Beecher, *Electrochem. Commun.*, 2009, **11**, 2285–2287.
126 V. D. Patake, C. D. Lokhande and O. S. Joo, *Appl. Surf. Sci.*, 2009, **255**, 4192–4196.
127 Q. Qu, S. Yang and X. Feng, *Adv. Mater.*, 2011, **23**, 5574–5580.
128 B. Li, H. Cao, J. Shao, M. Qu and J. H. Warner, *J. Mater. Chem.*, 2011, **21**, 5069–5075.
129 Z.-S. Wu, W. Ren, D.-W. Wang, F. Li, B. Liu and H.-M. Cheng, *ACS Nano*, 2010, **4**, 5835–5842.
130 Z. Li, J. Wang, X. Liu, S. Liu, J. Ou and S. Yang, *J. Mater. Chem.*, 2011, **21**, 3397–3403.
131 S. Chen, J. Zhu, X. Wu, Q. Han and X. Wang, *ACS Nano*, 2010, **4**, 2822–2830.
132 G. Yu, L. Hu, N. Liu, H. Wang, M. Vosgueritchian, Y. Yang, Y. Cui and Z. Bao, *Nano Lett.*, 2011, **11**, 4438–4442.
133 J. Zhu, M. Chen, H. Qu, Z. Luo, S. Wu, H. A. Colorado, S. Wei and Z. Guo, *Energy Environ. Sci.*, 2013, **6**, 194–204.
134 S. Chen, J. Zhu and X. Wang, *J. Phys. Chem. C*, 2010, **114**, 11829–11834.
135 J. Yan, T. Wei, W. Qiao, B. Shao, Q. Zhao, L. Zhang and Z. Fan, *Electrochim. Acta*, 2010, **55**, 6973–6978.
136 B. Zhao, J. Song, P. Liu, W. Xu, T. Fang, Z. Jiao, H. Zhang and Y. Jiang, *J. Mater. Chem.*, 2011, **21**, 18792–18798.
137 W. Shi, J. Zhu, D. H. Sim, Y. Y. Tay, Z. Lu, X. Zhang, Y. Sharma, M. Srinivasan, H. Zhang, H. H. Hng and Q. Yan, *J. Mater. Chem.*, 2011, **21**, 3422–3427.
138 S. D. Perera, A. D. Liyanage, N. Nijem, J. P. Ferraris, Y. J. Chabal and K. J. Balkus Jr, *J. Power Sources*, 2013, **230**, 130–137.
139 F. Li, J. Song, H. Yang, S. Gan, Q. Zhang, D. Han, A. Ivaska and L. Niu, *Nanotechnology*, 2009, **20**, 455602.
140 D. Wang, R. Kou, D. Choi, Z. Yang, Z. Nie, J. Li, L. V. Saraf, D. Hu, J. Zhang, G. L. Graff, J. Liu, M. A. Pope and I. A. Aksay, *ACS Nano*, 2010, **4**, 1587–1595.
141 G. Wang, L. Zhang and J. Zhang, *Chem. Soc. Rev.*, 2012, **41**, 797–828.
142 A. Davies, P. Audette, B. Farrow, F. Hassan, Z. Chen, J.-Y. Choi and A. Yu, *J. Phys. Chem. C*, 2011, **115**, 17612–17620.
143 S. Bose, N. H. Kim, T. Kuila, K.-t. Lau and J. H. Lee, *Nanotechnology*, 2011, **22**, 295202.
144 D.-W. Wang, F. Li, J. Zhao, W. Ren, Z.-G. Chen, J. Tan, Z.-S. Wu, I. Gentle, G. Q. Lu and H.-M. Cheng, *ACS Nano*, 2009, **3**, 1745–1752.
145 X.-M. Feng, R.-M. Li, Y.-W. Ma, R.-F. Chen, N.-E. Shi, Q.-L. Fan and W. Huang, *Adv. Funct. Mater.*, 2011, **21**, 2989–2996.
146 Q. Wu, Y. Xu, Z. Yao, A. Liu and G. Shi, *ACS Nano*, 2010, **4**, 1963–1970.
147 G. Kalita, M. Matsushima, H. Uchida, K. Wakita and M. Umeno, *J. Mater. Chem.*, 2010, **20**, 9713–9717.
148 J. D. Roy-Mayhew, D. J. Bozym, C. Punckt and I. A. Aksay, *ACS Nano*, 2010, **4**, 6203–6211.
149 S.-S. Li, K.-H. Tu, C.-C. Lin, C.-W. Chen and M. Chhowalla, *ACS Nano*, 2010, **4**, 3169–3174.
150 V. C. Tung, L.-M. Chen, M. J. Allen, J. K. Wassei, K. Nelson, R. B. Kaner and Y. Yang, *Nano Lett.*, 2009, **9**, 1949–1955.
151 Z. Yin, S. Wu, X. Zhou, X. Huang, Q. Zhang, F. Boey and H. Zhang, *Small*, 2010, **6**, 307–312.
152 H. Park, J. A. Rowehl, K. K. Kim, V. Bulovic and J. Kong, *Nanotechnology*, 2010, **21**, 505204.
153 Y.-B. Tang, C.-S. Lee, J. Xu, Z.-T. Liu, Z.-H. Chen, Z. He, Y.-L. Cao, G. Yuan, H. Song, L. Chen, L. Luo, H.-M. Cheng, W.-J. Zhang, I. Bello and S.-T. Lee, *ACS Nano*, 2010, **4**, 3482–3488.
154 N. Yang, J. Zhai, D. Wang, Y. Chen and L. Jiang, *ACS Nano*, 2010, **4**, 887–894.
155 T. Ouyang, Y. P. Chen, K. K. Yang and J. X. Zhong, *EPL*, 2009, **88**, 28002.
156 H. Sevinçli and G. Cuniberti, *Phys. Rev. B: Condens. Matter Mater. Phys.*, 2010, **81**, 113401.
157 K. Yang, Y. Chen, R. D'Agosta, Y. Xie, J. Zhong and A. Rubio, *Phys. Rev. B: Condens. Matter Mater. Phys.*, 2012, **86**, 045425.
158 H. Zheng, H. J. Liu, X. J. Tan, H. Y. Lv, L. Pan, J. Shi and X. F. Tang, *Appl. Phys. Lett.*, 2012, **100**, 093104.
159 X. Ni, G. Liang, J.-S. Wang and B. Li, *Appl. Phys. Lett.*, 2009, **95**, 192114.
160 A. H. Li, M. Shahbazi, S. H. Zhou, G. X. Wang, C. Zhang, P. Jood, G. Peleckis, Y. Du, Z. X. Cheng, X. L. Wang and Y. K. Kuo, *Thin Solid Films*, 2010, **518**, e57–e60.
161 J. Wang, S. B. Hocevar and B. Ogorevc, *Electrochem. Commun.*, 2004, **6**, 176–179.
162 L. Tang, H. Feng, J. Cheng and J. Li, *Chem. Commun.*, 2010, **46**, 5882–5884.
163 G. Shi, Y. Qu, Y. Zhai, Y. Liu, Z. Sun, J. Yang and L. Jin, *Electrochem. Commun.*, 2007, **9**, 1719–1724.
164 H.-X. Zhang, A.-M. Cao, J.-S. Hu, L.-J. Wan and S.-T. Lee, *Anal. Chem.*, 2006, **78**, 1967–1971.
165 M. Goh and M. Pumera, *Anal. Bioanal. Chem.*, 2011, **399**, 127–131.
166 C. X. Guo, Z. S. Lu, Y. Lei and C. M. Li, *Electrochem. Commun.*, 2010, **12**, 1237–1240.
167 X. Lu, H. Qi, X. Zhang, Z. Xue, J. Jin, X. Zhou and X. Liu, *Chem. Commun.*, 2011, **47**, 12494–12496.
168 S. Guo, D. Wen, Y. Zhai, S. Dong and E. Wang, *ACS Nano*, 2010, **4**, 3959–3968.
169 J. D. Fowler, M. J. Allen, V. C. Tung, Y. Yang, R. B. Kaner and B. H. Weiller, *ACS Nano*, 2009, **3**, 301–306.
170 J. T. Robinson, F. K. Perkins, E. S. Snow, Z. Wei and P. E. Sheehan, *Nano Lett.*, 2008, **8**, 3137–3140.
171 J. Li, D. Kuang, Y. Feng, F. Zhang, Z. Xu and M. Liu, *J. Hazard. Mater.*, 2012, **201–202**, 250–259.
172 J.-Y. Sun, K.-J. Huang, S.-Y. Wei, Z.-W. Wu and F.-P. Ren, *Colloids Surf., B*, 2011, **84**, 421–426.
173 C. Wang, L. Zhang, Z. Guo, J. Xu, H. Wang, K. Zhai and X. Zhuo, *Microchim. Acta*, 2010, **169**, 1–6.
174 K. R. Ratinac, W. Yang, S. P. Ringer and F. Braet, *Environ. Sci. Technol.*, 2010, **44**, 1167–1176.

175 Y. Dan, Y. Lu, N. J. Kybert, Z. Luo and A. T. C. Johnson, *Nano Lett.*, 2009, **9**, 1472–1475.
176 P. K. Ang, W. Chen, A. T. S. Wee and K. P. Loh, *J. Am. Chem. Soc.*, 2008, **130**, 14392–14393.
177 X. Zuo, S. He, D. Li, C. Peng, Q. Huang, S. Song and C. Fan, *Langmuir*, 2009, **26**, 1936–1939.
178 D. Du, J. Liu, X. Zhang, X. Cui and Y. Lin, *J. Mater. Chem.*, 2011, **21**, 8032–8037.
179 Y. Fan, H.-T. Lu, J.-H. Liu, C.-P. Yang, Q.-S. Jing, Y.-X. Zhang, X.-K. Yang and K.-J. Huang, *Colloids Surf., B*, 2011, **83**, 78–82.
180 H. Wu, J. Wang, X. Kang, C. Wang, D. Wang, J. Liu, I. A. Aksay and Y. Lin, *Talanta*, 2009, **80**, 403–406.
181 H. Gao, F. Xiao, C. B. Ching and H. Duan, *ACS Appl. Mater. Interfaces*, 2011, **3**, 3049–3057.
182 Y. Liu, X. Dong and P. Chen, *Chem. Soc. Rev.*, 2012, **41**, 2283–2307.
183 W. Yang, K. R. Ratinac, S. P. Ringer, P. Thordarson, J. J. Gooding and F. Braet, *Angew. Chem., Int. Ed.*, 2010, **49**, 2114–2138.
184 T. Kuila, S. Bose, P. Khanra, A. K. Mishra, N. H. Kim and J. H. Lee, *Biosens. Bioelectron.*, 2011, **26**, 4637–4648.
185 D. A. C. Brownson and C. E. Banks, *Analyst*, 2011, **136**, 2084–2089.
186 L. Li, Z. Du, S. Liu, Q. Hao, Y. Wang, Q. Li and T. Wang, *Talanta*, 2010, **82**, 1637–1641.
187 K.-J. Huang, D.-J. Niu, X. Liu, Z.-W. Wu, Y. Fan, Y.-F. Chang and Y.-Y. Wu, *Electrochim. Acta*, 2011, **56**, 2947–2953.
188 K. Zhou, Y. Zhu, X. Yang, J. Luo, C. Li and S. Luan, *Electrochim. Acta*, 2010, **55**, 3055–3060.
189 W.-J. Lin, C.-S. Liao, J.-H. Jhang and Y.-C. Tsai, *Electrochem. Commun.*, 2009, **11**, 2153–2156.
190 K. M. Shaju, G. V. Subba Rao and B. V. R. Chowdari, *Electrochem. Commun.*, 2002, **4**, 633–638.
191 C. Shan, H. Yang, D. Han, Q. Zhang, A. Ivaska and L. Niu, *Biosens. Bioelectron.*, 2010, **25**, 1504–1508.
192 G. P. Keeley, A. O'Neill, N. McEvoy, N. Peltekis, J. N. Coleman and G. S. Duesberg, *J. Mater. Chem.*, 2010, **20**, 7864–7869.
193 Y. Mao, Y. Bao, S. Gan, F. Li and L. Niu, *Biosens. Bioelectron.*, 2011, **28**, 291–297.
194 Y.-R. Kim, S. Bong, Y.-J. Kang, Y. Yang, R. K. Mahajan, J. S. Kim and H. Kim, *Biosens. Bioelectron.*, 2010, **25**, 2366–2369.
195 L. Tan, K.-G. Zhou, Y.-H. Zhang, H.-X. Wang, X.-D. Wang, Y.-F. Guo and H.-L. Zhang, *Electrochem. Commun.*, 2010, **12**, 557–560.
196 D. Lakshmi, A. Bossi, M. J. Whitcombe, I. Chianella, S. A. Fowler, S. Subrahmanyam, E. V. Piletska and S. A. Piletsky, *Anal. Chem.*, 2009, **81**, 3576–3584.
197 N. Gao, Z. Xu, F. Wang and S. Dong, *Electroanalysis*, 2007, **19**, 1655–1660.
198 J. Li, J. Zhao and X. Wei, *Sens. Actuators, B*, 2009, **140**, 663–669.
199 F. Zhang, Y. Li, Y.-e. Gu, Z. Wang and C. Wang, *Microchim. Acta*, 2011, **173**, 103–109.
200 F. Li, J. Chai, H. Yang, D. Han and L. Niu, *Talanta*, 2010, **81**, 1063–1068.
201 C.-L. Sun, H.-H. Lee, J.-M. Yang and C.-C. Wu, *Biosens. Bioelectron.*, 2011, **26**, 3450–3455.
202 Y. Xue, H. Zhao, Z. Wu, X. Li, Y. He and Z. Yuan, *Biosens. Bioelectron.*, 2011, **29**, 102–108.
203 W. Hong, H. Bai, Y. Xu, Z. Yao, Z. Gu and G. Shi, *J. Phys. Chem. C*, 2010, **114**, 1822–1826.
204 C. Shan, H. Yang, J. Song, D. Han, A. Ivaska and L. Niu, *Anal. Chem.*, 2009, **81**, 2378–2382.
205 Y. Huang, X. Dong, Y. Shi, C. M. Li, L.-J. Li and P. Chen, *Nanoscale*, 2010, **2**, 1485–1488.
206 Y. Wang, Y. Shao, D. W. Matson, J. Li and Y. Lin, *ACS Nano*, 2010, **4**, 1790–1798.
207 X. Kang, J. Wang, H. Wu, I. A. Aksay, J. Liu and Y. Lin, *Biosens. Bioelectron.*, 2009, **25**, 901–905.
208 T. T. Baby, S. S. J. Aravind, T. Arockiadoss, R. B. Rakhi and S. Ramaprabhu, *Sens. Actuators, B*, 2010, **145**, 71–77.
209 L.-M. Lu, H.-B. Li, F. Qu, X.-B. Zhang, G.-L. Shen and R.-Q. Yu, *Biosens. Bioelectron.*, 2011, **26**, 3500–3504.
210 C. X. Lim, H. Y. Hoh, P. K. Ang and K. P. Loh, *Anal. Chem.*, 2010, **82**, 7387–7393.
211 Y. Bo, W. Wang, J. Qi and S. Huang, *Analyst*, 2011, **136**, 1946–1951.
212 B. G. Choi, H. Park, M. H. Yang, Y. M. Jung, S. Y. Lee, W. H. Hong and T. J. Park, *Nanoscale*, 2010, **2**, 2692–2697.
213 K.-J. Huang, D.-J. Niu, J.-Y. Sun, C.-H. Han, Z.-W. Wu, Y.-L. Li and X.-Q. Xiong, *Colloids Surf., B*, 2011, **82**, 543–549.
214 N. Mohanty and V. Berry, *Nano Lett.*, 2008, **8**, 4469–4476.
215 A. Bonanni and M. Pumera, *ACS Nano*, 2011, **5**, 2356–2361.
216 Y. Bo, H. Yang, Y. Hu, T. Yao and S. Huang, *Electrochim. Acta*, 2011, **56**, 2676–2681.
217 M. Du, T. Yang and K. Jiao, *J. Mater. Chem.*, 2010, **20**, 9253–9260.
218 Q. Wei, K. Mao, D. Wu, Y. Dai, J. Yang, B. Du, M. Yang and H. Li, *Sens. Actuators, B*, 2010, **149**, 314–318.
219 Y. Fan, K.-J. Huang, D.-J. Niu, C.-P. Yang and Q.-S. Jing, *Electrochim. Acta*, 2011, **56**, 4685–4690.
220 L. Feng, Y. Chen, J. Ren and X. Qu, *Biomaterials*, 2011, **32**, 2930–2937.
221 G. Zhao, J. Li, X. Ren, C. Chen and X. Wang, *Environ. Sci. Technol.*, 2011, **45**, 10454–10462.
222 S.-T. Yang, Y. Chang, H. Wang, G. Liu, S. Chen, Y. Wang, Y. Liu and A. Cao, *J. Colloid Interface Sci.*, 2010, **351**, 122–127.
223 W. Gao, M. Majumder, L. B. Alemany, T. N. Narayanan, M. A. Ibarra, B. K. Pradhan and P. M. Ajayan, *ACS Appl. Mater. Interfaces*, 2011, **3**, 1821–1826.
224 J. L. Schnoor, *Environmental Modeling: Fate and Transport of Pollutants in Water, Air, and Soil*, John Wiley & Sons, New York, 1996.
225 A. K. Mishra and S. Ramaprabhu, *Desalination*, 2011, **282**, 39–45.
226 K. Zhang, V. Dwivedi, C. Chi and J. Wu, *J. Hazard. Mater.*, 2010, **182**, 162–168.
227 H. Sun, L. Cao and L. Lu, *Nano Res.*, 2011, **4**, 550–562.
228 C. Wang, C. Feng, Y. Gao, X. Ma, Q. Wu and Z. Wang, *Chem. Eng. J.*, 2011, **173**, 92–97.

229 K. Rajeshwar, M. E. Osugi, W. Chanmanee, C. R. Chenthamarakshan, M. V. B. Zanoni, P. Kajitvichyanukul and R. Krishnan-Ayer, *J. Photochem. Photobiol., C*, 2008, **9**, 171–192.
230 K. Woan, G. Pyrgiotakis and W. Sigmund, *Adv. Mater.*, 2009, **21**, 2233–2239.
231 X. Su, Q. Wu, X. Zhan, J. Wu, S. Wei and Z. Guo, *J. Mater. Sci.*, 2012, **47**, 2519–2534.
232 R. Asapu, V. M. Palla, B. Wang, Z. Guo, R. Sadu and D. H. Chen, *J. Photochem. Photobiol., A*, 2011, **225**, 81–87.
233 W. Suying, M. Pallavi, W. Qiang, C. Daniel, A. Ramesh, M. Yuanbing, H. Neel, P. Y. David and G. Zhanhu, *J. Electrochem. Soc.*, 2011, **158**, K205–K212.
234 Y. Zhang and C. Pan, *J. Mater. Sci.*, 2011, **46**, 2622–2626.
235 F. Wang and K. Zhang, *J. Mol. Catal. A: Chem.*, 2011, **345**, 101–107.
236 L. Sun, Z. Zhao, Y. Zhou and L. Liu, *Nanoscale*, 2012, **4**, 613–620.
237 Y. Liang, H. Wang, H. Sanchez Casalongue, Z. Chen and H. Dai, *Nano Res.*, 2010, **3**, 701–705.
238 J. Zhang, Z. Xiong and X. S. Zhao, *J. Mater. Chem.*, 2011, **21**, 3634–3640.
239 Z. Xiong, L. L. Zhang, J. Ma and X. S. Zhao, *Chem. Commun.*, 2010, **46**, 6099–6101.
240 L. Guardia, S. Villar-Rodil, J. I. Paredes, R. Rozada, A. Martínez-Alonso and J. M. D. Tascón, *Carbon*, 2012, **50**, 1014–1024.
241 B. Li and H. Cao, *J. Mater. Chem.*, 2011, **21**, 3346–3349.
242 S. Duquesne, C. Jama, M. Le Bras, R. Delobel, P. Recourt and J. M. Gloaguen, *Compos. Sci. Technol.*, 2003, **63**, 1141–1148.
243 Y. Shi, T. Kashiwagi, R. N. Walters, J. W. Gilman, R. E. Lyon and D. Y. Sogah, *Polymer*, 2009, **50**, 3478–3487.
244 Y. Hu, S. Wang, Z. Ling, Y. Zhuang, Z. Chen and W. Fan, *Macromol. Mater. Eng.*, 2003, **288**, 272–276.
245 A. Dasari, Z.-Z. Yu, Y.-W. Mai and S. Liu, *Nanotechnology*, 2007, **18**, 445602.
246 B. H. Cipiriano, T. Kashiwagi, S. R. Raghavan, Y. Yang, E. A. Grulke, K. Yamamoto, J. R. Shields and J. F. Douglas, *Polymer*, 2007, **48**, 6086–6096.
247 S. Peeterbroeck, F. Laoutid, J. M. Taulemesse, F. Monteverde, J. M. Lopez-Cuesta, J. B. Nagy, M. Alexandre and P. Dubois, *Adv. Funct. Mater.*, 2007, **17**, 2787–2791.
248 T. Kashiwagi, F. Du, J. F. Douglas, K. I. Winey, R. H. Harris and J. R. Shields, *Nat. Mater.*, 2005, **4**, 928–933.
249 P. a. Song, H. Liu, Y. Shen, B. Du, Z. Fang and Y. Wu, *J. Mater. Chem.*, 2009, **19**, 1305–1313.
250 F. Kim, J. Luo, R. Cruz-Silva, L. J. Cote, K. Sohn and J. Huang, *Adv. Funct. Mater.*, 2010, **20**, 2867–2873.
251 C. Zhang, W. W. Tjiu, W. Fan, Z. Yang, S. Huang and T. Liu, *J. Mater. Chem.*, 2011, **21**, 18011–18017.
252 X.-Z. Tang, W. Li, Z.-Z. Yu, M. A. Rafiee, J. Rafiee, F. Yavari and N. Koratkar, *Carbon*, 2011, **49**, 1258–1265.
253 Y. Shi and L.-J. Li, *J. Mater. Chem.*, 2011, **21**, 3277–3279.
254 Y. Lee, S. Kim, H.-i. Lee, H. Jeong, A. Raghu, K. Reddy and B. Kim, *Macromol. Res.*, 2011, **19**, 66–71.
255 S.-H. Liao, P.-L. Liu, M.-C. Hsiao, C.-C. Teng, C.-A. Wang, M.-D. Ger and C.-L. Chiang, *Ind. Eng. Chem. Res.*, 2012, **51**, 4573–4581.
256 X. Wang, S. Zhou, W. Xing, B. Yu, X. Feng, L. Song and Y. Hu, *J. Mater. Chem. A*, 2013, **1**, 4383–4390.
257 A. Dasari, Z.-Z. Yu, Y.-W. Mai, G. Cai and H. Song, *Polymer*, 2009, **50**, 1577–1587.
258 G. Huang, J. Gao, X. Wang, H. Liang and C. Ge, *Mater. Lett.*, 2012, **66**, 187–189.
259 G. Huang, H. Liang, Y. Wang, X. Wang, J. Gao and Z. Fei, *Mater. Chem. Phys.*, 2012, **132**, 520–528.
260 Y. Cao, J. Feng and P. Wu, *J. Mater. Chem.*, 2012, **22**, 14997–15005.
261 G. Huang, S. Chen, S. Tang and J. Gao, *Mater. Chem. Phys.*, 2012, **135**, 938–947.
262 A. L. Higginbotham, J. R. Lomeda, A. B. Morgan and J. M. Tour, *ACS Appl. Mater. Interfaces*, 2009, **1**, 2256–2261.
263 B. Yu, X. Wang, W. Xing, H. Yang, L. Song and Y. Hu, *Ind. Eng. Chem. Res.*, 2012, **51**, 14629–14636.
264 C. Bao, Y. Guo, B. Yuan, Y. Hu and L. Song, *J. Mater. Chem.*, 2012, **22**, 23057–23063.
265 X. Wang, L. Song, H. Yang, H. Lu and Y. Hu, *Ind. Eng. Chem. Res.*, 2011, **50**, 5376–5383.
266 X. Wang, Y. Hu, L. Song, H. Yang, B. Yu, B. Kandola and D. Deli, *Thermochim. Acta*, 2012, **543**, 156–164.
267 J. S. Bunch, S. S. Verbridge, J. S. Alden, A. M. van der Zande, J. M. Parpia, H. G. Craighead and P. L. McEuen, *Nano Lett.*, 2008, **8**, 2458–2462.
268 C. Lee, X. Wei, J. W. Kysar and J. Hone, *Science*, 2008, **321**, 385–388.
269 S. P. Koenig, N. G. Boddeti, M. L. Dunn and J. S. Bunch, *Nat. Nanotechnol.*, 2011, **6**, 543–546.
270 Z. Lu and M. L. Dunn, *J. Appl. Phys.*, 2010, **107**, 044301.
271 S. Garaj, W. Hubbard, A. Reina, J. Kong, D. Branton and J. A. Golovchenko, *Nature*, 2010, **467**, 190–193.
272 S. Blankenburg, M. Bieri, R. Fasel, K. Müllen, C. A. Pignedoli and D. Passerone, *Small*, 2010, **6**, 2266–2271.
273 J. Schrier, *J. Phys. Chem. Lett.*, 2010, **1**, 2284–2287.
274 D.-e. Jiang, V. R. Cooper and S. Dai, *Nano Lett.*, 2009, **9**, 4019–4024.
275 H. Du, J. Li, J. Zhang, G. Su, X. Li and Y. Zhao, *J. Phys. Chem. C*, 2011, **115**, 23261–23266.
276 E. E. Fileti, G. M. Dalpian and R. Rivelino, *J. Appl. Phys.*, 2010, **108**, 113527.
277 C. A. Merchant, K. Healy, M. Wanunu, V. Ray, N. Peterman, J. Bartel, M. D. Fischbein, K. Venta, Z. Luo, A. T. C. Johnson and M. Drndić, *Nano Lett.*, 2010, **10**, 2915–2921.

